Mechanical signatures of the current-blockade instability in suspended carbon nanotubes

Gianluca Micchi

To cite this version:

Gianluca Micchi. Mechanical signatures of the current-blockade instability in suspended carbon nanotubes. Other [cond-mat.other]. Université de Bordeaux, 2016. English. NNT : 2016BORD0337 . tel-01480268

HAL Id: tel-01480268
https://theses.hal.science/tel-01480268

Submitted on 1 Mar 2017

THÈSE

PRÉSENTÉE À

L'UNIVERSITÉ DE BORDEAUX

ÉCOLE DOCTORALE DES SCIENCES PHYSIQUES ET DE L'INGÉNIEUR

par **Gianluca Micchi**

POUR OBTENIR LE GRADE DE

DOCTEUR

SPÉCIALITÉ : LASERS, MATIÈRE ET NANOSCIENCES

Mechanical Signatures of the Current-Blockade Instability in Suspended Carbon Nanotubes

---

Date de soutenance : 12 decembre 2016
Devant la commission d'examen compose de :

Shahal ILANI	Prof, Weizmann Institute of Science	rapporteur
Andrew ARMOUR	Prof, Nottingham University	rapporteur
Robert WHITNEY	CR, Université de Grenoble Alpes & CNRS	examinateur
Jérôme CAYSSOL	Prof, Université de Bordeaux	examinateur
Fabio PISTOLESI	DR, Université de Bordeaux	directeur
Rémi AVRILLER	CR, Université de Bordeaux	co-directeur

– 2016 –

Caractéristiques mécaniques de l'instabilité provoquée par le blocage du courant dans les nanotubes de carbone suspendus

Résumé

Le couplage fort entre le transport électronique dans une boîte quantique à un seul niveau et un oscillateur nano-mécanique couplé capacitivement peut conduire à une transition vers un état mécaniquement bistable et bloqué en courant. Son observation est à portée de main dans les expériences de pointe ménées sur les nanotubes de carbone. Nous étudions donc la réponse mécanique du système et plus précisément la fonction spectrale de déplacement, la réponse linéaire à un solicitation externe et le comportement pendant le retour à l'équilibre. Nous montrons qu'il existe une relation étroite entre les grandeurs électriques (telles le courant électrique et la fonction spectrale des fluctuations du courant) et mécaniques. Nous constatons qu'en augmentant le couplage électromécanique, les deux fonctions spectrales présentent un pic qui s'élargit et se déplace vers les basses fréquences alors que le temps de déphasage de l'oscillateur se raccourcit. Ces effets sont maximaux à la transition où les non-linéarités dominent la dynamique et sont robustes vis-à-vis de l'effet des fluctuations extérieures et de la dissipation. Ces caractéristiques fortes ouvrent la voie à la détection de la transition vers l'état de blocage du courant dans des dispositifs actuellement étudiés par plusieurs groupes.

Mots-clés : systèmes nano-électromécaniques, transport électronique cohérent, nanotubes de carbone, analyse spectrale, non-linéarités, fluctuations, transitions de phase.

Thèse preparée au LOMA, Université de Bordeaux, 351 cours de la libération bâtiment A4N, 33405 Talence CEDEX, FRANCE.

Mechanical Signatures of the Current-Blockade Instability in Suspended Carbon Nanotubes

Abstract

The strong coupling between electronic transport in a single-level quantum dot and a capacitively coupled nano-mechanical oscillator may lead to a transition towards a mechanically-bistable and blocked-current state. Its observation is at reach in carbon-nanotube state-of-art experiments. Therefore, we investigate the mechanical response of the system, namely the displacement spectral function, the linear response to a driving, and the ring-down behavior, and the electric response, namely the electric current and current spectral function. We show that a close relation between electric and mechanical quantities exists. We find that, by increasing the electromechanical coupling, the peak in both spectral functions broadens and shifts at low frequencies while the oscillator dephasing time shortens. These effects are maximum at the transition where nonlinearities dominate the dynamics, and are robust towards the effect of external fluctuations and dissipation. These strong signatures open the way to detect the blockade transition in devices currently studied by several groups.

Keywords: nanoelectromechanical systems, coherent electronic transport, carbon nanotubes, spectral analysis, nonlinearities, fluctuations, phase transition.

Thesis prepared in LOMA, University of Bordeaux, 351 cours de la libération building A4N, 33405 Talence CEDEX, FRANCE.

Preface

> Do not take life too seriously –
> you will never get out of it alive.
>
> Elbert “Carneades” Hubbard

Welcome ladies and gentleman to the wonderful story of nanoelectromechanical systems! It is a story of a great talent that’s trying to blossom and of mysteries to solve. It is a story of a thousand people that cooperate not knowing each other. It is a story of crocodiles and tightropes. It is the story of three long years of my life.

This story wouldn’t be possible without my Anechka, my family, my supervisors, and my friends. Thank you.

Contents

Preface **vii**

1 Everything about NEMS* **1**

1.1 Introduction to NEMS . . . 2

1.1.1 Single-electron transistors . . . 2

1.1.2 Quantum or classical treatment? . . . 3

1.1.3 The electron back-action . . . 4

1.2 Carbon nanotubes . . . 6

1.2.1 History of carbon nanotubes . . . 6

1.2.2 Properties of carbon nanotubes . . . 7

1.3 Suspending a nanotube . . . 9

1.3.1 First realizations . . . 9

1.3.2 Sensing experiments . . . 11

1.3.3 Decoherence in a carbon nanotube . . . 13

1.3.4 A novel fabrication technique . . . 15

2 The model **19**

2.1 The electromechanical coupling . . . 19

2.2 Hamiltonian of the system . . . 21

2.3 Electron dynamics . . . 24

2.3.1 Dynamics of the electron operators . . . 24

2.3.2 Derivation of important physical quantities: number of electrons, its auto-correlator, and electric current . . . 25

2.4 The equation of motion for the oscillator . . . 27

2.4.1 Derivation of the Langevin Equation 28

2.5 Fluctuations and Fokker-Planck picture 30

2.5.1 The probability density function in the energy space 31

2.5.2 An analysis of the probability density function 32

2.5.3 A fluctuation-dissipation relation 33

3 The results, or: What we did 35

3.1 The mechanical softening of the system 35

3.1.1 The force and the equilibrium positions 36

3.1.2 The mechanical resonance frequency 37

3.1.3 The potential of the system 38

3.1.4 Sweeping around the symmetric gating 38

3.1.5 The effects of a finite temperature 41

3.2 The electric current 44

3.2.1 Analytic calculations of the electric current through the system . . 45

3.3 The effect of nonlinearities 47

3.3.1 An analytical approach 47

3.3.2 A numerical approach 48

3.4 The autocorrelation functions 49

3.4.1 Analytic calculations of $S_{xx}(\omega)$ 50

3.4.2 Analytic calculation of $S_{II}(\omega)$ 56

3.5 The ring-down behavior 59

3.5.1 Analytical calculation of the ring-down displacement 60

3.5.2 Numerical calculation of the ring-down displacement 62

3.6 The influence of asymmetry 63

3.6.1 The displacement spectrum 63

3.6.2 Relation between current and displacement spectra 65

3.7 Effect of thermal fluctuations on mechanical noise 67

3.8 The effects of a dissipative coupling 68

4 Conclusions and future perspectives 71

4.1 Conclusions 71

4.2 Future perspectives 72

Chapter 1

Everything you always wanted to know about carbon-nanotube based nano electromechanical systems* (*but were afraid to ask)

The detection and actuation of mechanical systems at the nano-scale represents a challenge with important future perspectives, both for understanding fundamental physics and for technological applications [1, 2, 3, 4, 5, 6, 7, 8, 9].

One possible path for winning this challenge revolves around the interaction of the mechanical system with an electric current; this electromechanical interaction allows for the detection of displacements of extremely small objects (nanometric size) like carbon nanotubes [10].

Nano ElectroMechanical Systems (NEMS) can be used, for example, to reproduce in a controllable way all effects due to electron-phonon coupling, like superconductivity [11]. NEMS also have several practical applications, for example as sensors or as an evolution of the Micro ElectroMechanical Systems (MEMS) that have already had so much of an influence in our life (suffice it to mention the accelerometers nowadays present in all smartphones, tablets, etc.).

An obvious way to increase the sensitivity of the detection and actuation of the mechanical motion, and consequently produce higher quality devices, is to increase the electromechanical coupling. However, a strong coupling can also lead to more complex behaviors [12, 13].

The thesis I defend is that the strong coupling regime in NEMS is an intriguing phenomenon with a host of interesting properties that deserve theoretical and experimental investigation [14, 15]. In particular, we focus on an oscillating quantum dot, realized for example with a suspended carbon nanotube; for such a system the arisal of a current blockade associated to a mechanical bistability and a decrease in the quality factor of the mechanical oscillator has already been predicted [16, 17, 18]. In this regime, the oscillator becomes strongly nonlinear and this, combined with the voltage- and temperature-induced fluctuations of the nanotube, leads to a very large phase noise that dominates the mechanics of the oscillator. This is particularly noticeable in the spectrum of the auto-correlation function of the movement of the oscillator and leads to a difference between the ring-down time and the width of the resonance in the spectrum, unexplicable taking into account only the energy dissipation.

The analytical and numerical calculation of these quantities constitutes the main novel result of this work. For simplicity, we first consider a system at zero temperature, vanishing bias voltage, and at the electron-hole symmetry point; then we show that the results we obtain are robust under small variations of these parameters and give explicit analytical expressions describing the effect of these small variations. Most importantly, we estimate the phenomena we predict to be observable in current state-of-the-art devices.

However discouraging these results might seem for the realization of sensors, they are nevertheless important, because they give us a clearer understanding of the fundamental interaction between a single mechanical mode and a single electron.

These results have been published in two papers [14, 15].

1.1 A general introduction to nano electromechanical systems

A typical NEMS is composed by an oscillating mechanical part and a transducer that converts the mechanical displacement into an electric signal. For example, the oscillating element can be a metallic island, a nanotube, a nanobeam, or a molecule. The transduction can be done by a current flowing through the oscillating mechanical part in presence of a magnetic field or by the variation of the electric field generated on a nearby sensor.

The typically tiny size of the oscillating element implies a quantization on the number of electrons it contains. The addition of a single electron requires a large amount of energy and brings an additional force to the oscillating element due to the capacitive coupling to the gate. The oscillator starts to move, varying the capacitance as it does so. In turn, this changes the potential of the island, inducing thus the electron to leave. This complex electromechanical interaction, that will be explained in more detail in the next chapter, is at the heart of all the properties of NEMS.

One of the first examples of NEMS to be experimentally realized is a mechanical oscillator coupled to a single-electron transistor (SET) [19].

1.1.1 Single-electron transistors

A single-electron transistor, or SET, is a device consisting of a metallic island of nanometric size connected to a drain, a source, and a gate electrode. The island is connected to the electrodes through capacitances; tunneling is possible to and from the drain and source electrode, but not the gate. See Figure 1.1, panel (a).

Typically, SETs operate at very low temperatures: In this regime, the charging energy needed to add a single electron to the very small metallic island is not available to the system and the number of electrons inside the island is quantized. This is known as the *Coulomb blockade regime* due to the high resistance to the passage of electric current.

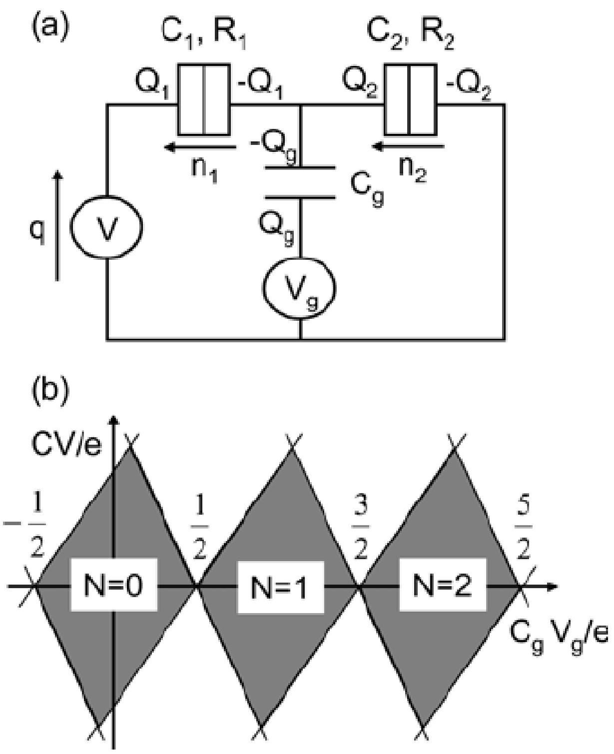

Figure 1.1: Panel (a): A single-electron transistor, or SET. Panel (b): Coulomb diamonds. Taken from [20].

The exact number of electrons in the island is controlled by the gate voltage. When it is chosen to be near a semi-integer $N + 1/2$, a single-electron current is actually allowed to tunnel in and out of the island through the source and drain capacitances. This happens for any value of N, leading to a periodic behavior of the conductance of the system: When color-plotted against the gate voltage and the bias voltage, it shows a peculiar pattern known as *Coulomb diamonds* because of its shape, resembling the diamonds suit in cards. Coulomb diamonds are depicted in Figure 1.1, panel (b).

Typically one electron tunnels from the source to the island, spends some time in the island, and then tunnels from the island to the drain, although this is not the only possibility. If the temperature T is low enough, electrons manage to keep their coherence, leading to quantum effects in the electric current passing through. Otherwise, the electronic transport is known as *incoherent* or *sequential*. The coherence condition says $k_B T \ll \hbar\Gamma$, where Γ is the typical width of the discrete levels inside the SET due to the tunneling coupling with the source and drain leads.

The coherence of the electronic transport could cause *cotunneling*: It is the effect of two electronic transition happening coherently, such as a double jump of an electron directly from the left to the right lead through an intermediate virtual state. Cotunneling processes happen when the intermediate state of the transition is energetically prohibited in the standard sequential tunneling regime (for example, in the intermediate state there could be two electrons in the central island). These higher-order effects are discarded in what is known as the *orthodox* theory of Coulomb blockade [21].

Because of their extreme sensitivity to charge variations, SETs are used to detect a nanometric motion of the central metallic island with respect to the gate electrode. The transduction from charge sensitivity to mechanical sensitivity is possible thanks to the capacitive coupling between the island and the gate, as explained in section 2.1.

1.1.2 Quantum or classical treatment?

An important theoretical question that arises, especially when treating nanoscopic objects, is “Should I use quantum mechanics?” Of course, quantum mechanics and classical mechanics offer a different view of the world (and a different set of equations as well). While quantum mechanics is always valid, it is not required to accurately describe the system at a sufficiently high temperature; classical mechanics is sufficient. When that is the case, a classical theory is often the first step to take, since it is often simpler.

Concerning the system at hand, it has been shown that it is possible to use classical mechanics to treat the motion of the oscillating mechanical system not only when the temperature is high enough ($T \gg \omega_0$, ω_0 being the phonon energy), but also at very low temperatures, provided a large bias voltage is applied across the system ($V \gg \omega_0$) [22, 13]. The voltage-induced fluctuations of the charge coupled to the oscillator can be interpreted as temperature-induced fluctuations of an external bath or, in other words, the bias voltage introduces an effective temperature to the system.

Ref. [13], for example, using a functional integral approach, shows this to be true in the Born-Oppenheimer limit, that is, when the typical timescale of the electronic degrees of freedom Γ^{-1} is much shorter than the period of the mechanical oscillation ω_m^{-1} (limit that we will consider as well). Quadratic terms in the quantum fluctuations around the classical trajectory give a Gaussian noise, while terms of higher orders bring corrections to the gaussianicity; however, when the typical timescale of the correlation of the noise is very short compared to the total time of an oscillation (fast electrons), one can integrate over a period of the oscillation and, via the central limit theorem, say that the noise is Gaussian. Thus the system can be treated semiclassically with an added source of Gaussian noise (of quantum origin) due to the interaction with the electrons. This means that, while the dynamics of the electrons is governed by quantum annihilation and creation operators and solved using the (quantum-mechanical) Schrödinger equation, the position of the oscillator x and its momentum p are considered as classical variables and, therefore, computed using a classical stochastic equation (Langevin, in our case).

In our thesis, we consider a nano electromechanical system in the semiclassical regime with fast electrons.

1.1.3 The electron back-action

The importance of the electron back-action on the mechanical degrees of freedom in NEMS was recognized very early [21, 23, 24, 25, 26, 27]. At first, the behavior of the system under weak coupling was studied [21]: The probability distribution of the system was shown to be close to a Gaussian with a width determined by the bias voltage through the system (in accordance with the aforementioned result for which the bias voltage acts as an effective temperature to the mechanical oscillator), while the current was shown to be slightly hampered by the coupling (an effect which evolves into the current blockade at high values of the electromechanical coupling).

The first experimental evidence was that the conductance of the system subject to an AC driving decreases at the resonance frequencies of the nanotube. This was initially found in classical mechanical oscillators coupled to a SET in the orthodox incoherent Coulomb-blockade regime.

As already mentioned, in this regime the presence of current blockade associated to a mechanical bistability has been predicted [16]. The transition to the bistable state is controlled by the intensity of the electro-mechanical coupling $\epsilon_P \equiv F_0^2/k$, where k is the spring constant of the oscillator and F_0 is the force acting on the oscillator when one electron is added to the metallic island of the SET; the transition has been predicted when both the temperature T and the bias voltage V are smaller than ϵ_P (we work throughout the manuscript with electric charge e, Boltzmann constant k_B, and reduced Planck constant $\hbar$ set to 1). This makes this effect not easy to observe, since in general

Franck-Condon blockade

It is useful to specify the difference between the current blockade that is the center of our investigation and the similar effect known as *Franck-Condon blockade*: The latter implies the presence of side-bands in the Coulomb diamonds; the side-bands are due to the interaction of electrons with high-frequency phonons and they are only visible in the regime where the phonon energy ω_0 is much larger than the energies that determine the width of the edges in the Coulomb blockade, that is, temperature and width of the electronic level. To be specific, this condition reads $\omega_0 \gg T \gg \Gamma$; incidentally, this also means that the electron tunneling in such a system needs to be weak.

The Franck-Condon regime requires a fully quantum treatment of the mechanical oscillator, that is not needed for the current blockade we study.

This effect has already been observed [34, 35, 36, 37].

the value of ϵ_P is very small. Therefore, to approach the regime of the current blockade, one can either reduce the temperature or increase the coupling. Typically, both are used.

A reduction in the temperature brings the SET to operate in the coherent regime of transport. In this regime, an additional condition has to be satisfied for the bistable state to appear: ϵ_P greater than Γ, the typical width of the electron level.

Increasing the coupling is more difficult: It has been proposed, for instance, to take advantage of the Euler buckling instability [28, 29], that is, to use a nanobeam or nanotube as a SET and to put them under longitudinal compression. This actually reduces the spring constant k of the oscillator, leading to an increase in the electromechanical coupling $\varepsilon_P = F_0^2/k$ by a factor of 100, approximately. However, up to now this technique has not been used, to the best of our knowledge.

This situation changed dramatically in the last years due to the enormous progress that has been achieved in the detection and manipulation of carbon-nanotube mechanical oscillators. For the first time, experiments were able to observe effects due to the strong electromechanical coupling [30, 18], even if the transition to the current blockade has not been reached yet. However, new fabrication techniques [31] allow for the realization of devices with much shorter distance d between the CNT and the gate. For example, in Ref. [32], the authors show a CNT 880 nm long with a 2 nm diameter, resonating at frequency $\omega_0/2\pi = 78$ MHz, and suspended at $d = 125$ nm above the gate. For this device, experimental measurements of the mode softening are consistent with a coupling $\varepsilon_P \approx 300$ mK. More recently, the same group presented results of a device with $d = 60$ nm [33] for which we estimate ε_P in the Kelvin range. These figures indicate that observation of the transition should be possible by measuring the device at standard cryogenic temperatures of the order of 100 mK.

Therefore, we devote our manuscript to the analysis of the transition to the current blockade and to the physical quantities that one should analyze to observe it. During the preparation of this thesis, two papers have been peer-reviewed and published [14, 15].

The introductory chapter continues with a short history of carbon nanotubes and of their main characteristics, then an analysis of the experimental advances we mentioned above.

1.2 Carbon nanotubes

A carbon nanotube (CNT) is a long stretch of carbon atoms arranged in a two-dimensional hexagonal pattern which has been rolled to create a tiny pipe of sort – actually, a nanotube! It is strictly connected to one of the miracle materials of the twenty-first century: graphene. They both hold promises of revolutionizing the technological industry thanks to their remarkable mechanical and electrical properties and to the abundance of carbon in Nature, pretty much like silicon did in the past century. However, the great potential that these materials hold must be thoroughly analyzed to find a proper way of putting it to use. Applications for carbon nanotubes have been proposed in several fields: electronics, quantum information, biophysics, chemistry, modeling of quantum systems... In particular, suspended carbon nanotubes have an impressive series of applications for mass [3, 38], force [7], magnetic [39] and biological [40] sensors.

1.2.1 History of carbon nanotubes

Carbon nanotubes were discovered at the beginning of the '90s, a period in which the research for fullerenes – carbon-based molecules with 3-electron bonds (*sp2*) on each atom of carbon instead of four-electron bonds (*sp3*) – was very intense. The interest mainly sparked from the fourth, missing link: In certain configurations, the remaining electrons can move almost freely above the structure of carbon atoms giving remarkable electronic properties to the material. (All the "free" electrons actually participate in a so-called π state.)

The first experimental evidence of carbon nanotubes was in 1991, in the work by Iijima[41]. His *needle-like helical microtubules of graphitic carbon* were created by electric arc-discharge method: Two carbon rods are placed in front of each other in a container filled with a small quantity of inert gas; when a sufficiently high voltage is established between the two rods an electric arc is set; some carbon evaporates from one of the rods and creates some tubular structures on the other rod. Iijima immediately recognized that carbon nanotubes can be considered as graphite sheets rolled on themselves: Several coaxial tubes, whose number is not fixed, are created one inside the other, and their distance is similar to the distance of different sheets in graphite. This intuition helped in the theoretical prediction of electrical properties of carbon nanotubes [42, 43, 44].

In 1993 there was with the first experimental realization of single-walled carbon nanotubes (SWCNT), that is, systems that are composed of just one rolled graphene sheet [45, 46].

However, the arc-discharge method used up to that moment method implies very high temperatures ($\approx 3000\,^{\circ}\mathrm{C}$) and generates lots of unwanted structures along the nanotubes. The result is that the nanotubes are all tangled and lots of work is needed to separate and purify them. For these reasons, people tried to find new methods for synthesizing the carbon nanotubes. The first attempt was laser ablation [47], but the real breakthrough came with the technique of chemical vapor deposition [48], which allows for the synthesis of large quantities of high-quality single-walled carbon nanotubes. This has quickly become the method of choice, still being the most used as of 2016.

1.2.2 Electronic and mechanical properties of carbon nanotubes

Single-wall carbon nanotubes provide a simpler theoretical picture, therefore we focus on them. Even though their synthesis is performed with a different technique, one can think of them as a long strip of graphene that is rolled on its short side to form a tube (shaded in Figure 1.2 panel a, and the printed pattern facing outward).

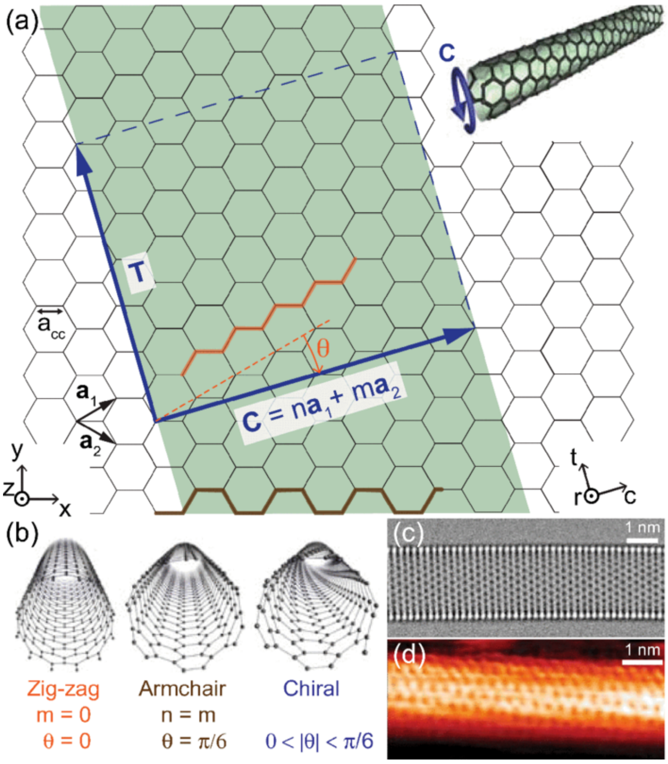

Figure 1.2: Atomic structure of carbon nanotubes. (a) A SWCNT is equivalent to a rolled-up graphene strip. In this example, $(n, m) = (6, 2)$ and $\theta = 13.9°$. (b) Chiral indices here: zigzag $(12, 0)$, armchair $(6, 6)$, chiral $(6, 4)$. (c) Zigzag CNT imaged by transmission electron microscopy. (d) Chiral CNT imaged by scanning tunneling microscopy. Taken from [49].

There is a discrete - yet infinite - number of ways to roll the nanotube while preserving the continuity of the structure: They are numbered by the *chiral vector* $\boldsymbol{C} = n\boldsymbol{a_1} + m\boldsymbol{a_2}$, where $\boldsymbol{a_1}$ and $\boldsymbol{a_2}$ are the basis vectors for the hexagonal lattice of graphene. (Usually, a chiral angle θ between the chiral vector and the direction of $\boldsymbol{a_1}$ is also defined.) The chiral vector $\boldsymbol{C}$ thus spans the nanotube circumference and connects lattice sites that are brought together by rolling up (inset in Figure 1.2 panel a). Chiral indices (n, m) completely define the nanotube structure and thus its properties: when $m = 0$ the nanotube is called *zigzag*, when $n = m$ it is called *armchair*, and *chiral* in all other situations. Zigzag and armchair nanotubes are called so because of the shape of the edge formed by a cut perpendicular to the nanotube axis (see Figure 1.2). The unit cell of the nanotube is much larger than the unit cell of graphene (dashed lines in the figure, with unit vector $\boldsymbol{T}$ indicated).

Electronic properties

The electronic properties of carbon nanotubes come from the ones of graphene. We remind that, in graphene, the Fermi surface touches the electronic bands in six points of the Brillouin zone which have a linear dispersion relation. Due to degeneracies, these six points can be divided in two classes of three, usually labeled as K and K'. This peculiar structure is called *semimetallic* because there is no gap between occupied and unoccupied states but at the same time there is no conducting electron at zero temperature; together with the linear dispersion relation of the bands at the Fermi level, it is responsible for many interesting properties of graphene, such as the very high mobility. The electronic bands to which K and K' belong are called π bands and are created by the set of the quasi-free electrons perpendicular to the graphene sheet, as we already mentioned when talking about fullerenes. The remaining three electrons per carbon nanotube hybridize in the so-called $sp2$ bonding, responsible for other bands known as σ bands that are far away in energy and don't actively participate in electronic properties (they will however be fundamental in determining the mechanical properties [50]).

The differences between the properties of graphene and those of carbon nanotubes come from the chirality of the nanotube, which determines the allowed transversal wavevectors of the electrons: if the vectors pointing to K and K' are allowed, then the nanotube is *metallic* (actually semimetallic, but metallic is the common way of addressing it); if they are not, the bands are separated by a gap and the nanotube is *semiconducting*. The analysis of the band structure of the system says that a nanotube is metallic if the difference between the chiral coefficients $n - m$ is a multiple of 3; as a consequence, no armchair ($n = m$) semiconducting nanotube exists. What we presented here is just a first approximation: finer details such as the opening of a narrow gap in some kinds of metallic nanotube can be found in the literature [49, 43, 51].

To study transport properties of carbon nanotubes we have to connect them to electric leads. This creates a boundary condition also in the longitudinal direction: The electrons are now confined to a limited space and this generates a discrete distribution of the energy levels of the system. This is known as the *quantum dot* regime; it has been experimentally realized and is the regime in which we will develop our theory. It is remarkable to notice that the quantum dot regime does not substantially depend on the chirality of the nanotube; for this reason, our model doesn't take chirality into account. We will also assume to have a strong confinement, so that the energy difference between electronic levels is very high compared to all other energy scales of the system; consequently, when the quantum dot is connected to two leads through a tunneling barrier, only one electronic level participates in the dynamics of the system.

Mechanical properties

The mechanical properties of the nanotube arise once again from the simplicity of the structure.

For example, their very high stiffness is due to the perfect symmetry of the structure, together with the absence of defect in ultra-clean nanotubes: A compression or strain of the nanotube requires the simultaneous strain of all the strong *sp*2 bonds between the carbon atoms [50]; theoretical models and experimental results confirm a Young modulus in the range of 1 TPa, 5 times larger than steel.

Another remarkable property is their extremely high aspect ratio, that is the ratio between their length and their diameter, which makes them one-dimensional systems with a very good approximation. Carbon nanotubes up to 550 mm long have been recently built [52]; considering that their diameter is typically of the order of 10 nm, it makes for an astounding aspect ratio of 50 millions to 1. By analogy, a standard bridge for cars with the same aspect ratio would join the Earth to the Moon.

One way of exploiting the mechanical properties of carbon nanotubes is to suspend them over a gate, like a rope bridge or a tightrope, clamped at both extremities. In this situation, the nanotube can be seen as a nearly perfect 1-dimensional resonator that can be excited with several different oscillation modes. Going from the slowest to the fastest, they are [53]: (1) Bending modes, in which the nanotube oscillates in the transversal plane, like a guitar string. The wavelength is given by submultiples of double the length of the nanotube L, and the typical frequency for a 1 µm-long CNT is around 100 MHz (although determined also by the tension of the nanotube). (2) Stretching modes, in which the nanotube is elongated and compressed along its longitudinal axis. Typically around 200 GHz for length of 1 µm. (3) Breathing modes, in which the nanotube expands and contracts its diameter, like the chest of a person that is breathing. They don't depend on the length of the nanotube. Typical frequencies are around 3 THz.

In our system we will work with bending modes, that are the easiest to excite and also allow us to study the system from a semiclassical point of view.

1.3 Suspending a nanotube

To take advantage of the electrical properties of carbon nanotubes, one needs to put some current into them. And to take advantage of their *mechanical* properties, the nanotubes must be free to move. It sounds all too natural, then, to work with suspended carbon nanotubes, systems made of a nanotube clamped on two metallic leads and suspended above a gate.

1.3.1 First realizations

The first realization of a suspended nano-mechanical system using carbon nanotubes was in 2000 [54]. In this case, however, the authors show the effects of an electro-mechanical coupling in ropes made of a bundle of about a hundred tubes. This peculiar structure is the result of a nanotube growth with the arc-discharge method, after a process of purification.

Instead, the first experiment on a single suspended carbon nanotube was published in 2004 [10] (see Figure 1.3). The authors show how the electric current through a driven suspended CNT changes as a function of the driving frequency at room temperature (Figure 1.4). The driving is done through a gate voltage δV_g that oscillates on a range of frequencies close to the mechanical resonance ω_m. They find two different effects: (1) A resonance around ω_m. (2) A slowly varying background, that we neglect in the following.

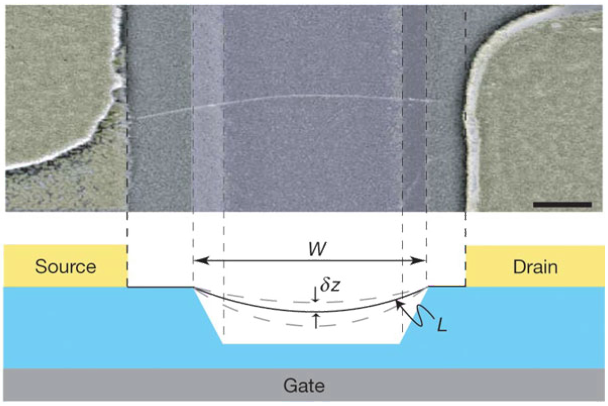

Figure 1.3: A scheme of the experimental apparatus used in [10]. The nanotube and the gate form a capacitor with capacitance C_g: electrons amass on the nanotube following $n_g = C_g V_g$, where n_g is the number of electrons and V_g is the gate potential. When the nanotube oscillates in the z direction the capacitance changes; this creates an electromechanical coupling that influences the passage of the current.

To understand the resonance around ω_m, we first need to focus on the *mixing current* technique that they use to measure the output current: An oscillating bias voltage δV_{sd} is applied across the nanotube; its frequency ω_{sd} is kept at a constant small detuning $\delta\omega$ from the driving frequency on the gate ω_g. (In this particular experiment, the detuning is fixed at 10 kHz, while the driving frequency is around 50 MHz.)

Now, the current inside the nanotube depends on the bias and gate voltage in a non-trivial way (see 2.33). In general, we can write

$$\begin{aligned} I(V_{sd}, V_g) = I(\bar{V}_{sd}, \bar{V}_g) &+ \left.\frac{\partial I}{\partial V_{sd}}\right|_{\bar{V}_{sd}} \delta V_{sd} + \left.\frac{\partial I}{\partial V_g}\right|_{\bar{V}_g} \delta V_g \\ &+ \frac{1}{2}\left.\frac{\partial^2 I}{\partial V_{sd}^2}\right|_{\bar{V}_{sd}} \delta V_{sd}^2 + \frac{1}{2}\left.\frac{\partial^2 I}{\partial V_g^2}\right|_{\bar{V}_g} \delta V_g^2 + \left.\frac{\partial^2 I}{\partial V_{sd}\partial V_g}\right|_{\bar{V}_{sd},\bar{V}_g} \delta V_{sd}\delta V_g + \dots \end{aligned} \tag{1.1}$$

Each term in Eq. (1.1) oscillates at a different frequency. In particular, the mixed term proportional to $\delta V_{sd}\delta V_g$ oscillates at the detuning frequency $\delta\omega$. Information can then be extracted from this low-frequency signal. This procedure is undertaken mainly to avoid a loss of information in the RC part of the circuit, that acts as a low-pass filter. Moreover, it allows one to keep only the interesting electromechanical part of the current, filtering out all other contributions such as displacement currents. (The name mixing technique comes from the original mechanical frequency being mixed down to 10 kHz, pretty much like in an FM radio [55].)

Now, the component at 10 kHz of the current through the system is determined by the product between the oscillating variation of conductance and the oscillating bias voltage, $I = \delta G \delta V_{sd}$. As we have just seen, the former depends on the variation of the induced charge $\delta q = C_g \delta V_g + V_g \delta C_g$, where δC_g is the variation of the gate capacitance with the motion of the nanotube and has thus the typical oscillating frequency ω_m. This leads to the final expression for the current

$$I = \frac{1}{2\sqrt{2}} \frac{dG}{dV_g} \left(\delta V_g + V_g^{DC} \frac{\delta C_g}{C_g} \right) \delta V_{sd}. \tag{1.2}$$

This is fit in Figure 1.4 with a Lorentzian function with mechanical resonance $\omega_m = 55\,\text{MHz}$, quality factor $Q = \omega_m/\Delta\omega \approx 80$ where $\Delta\omega$ is the width of the resonance, and an appropriate phase difference between the gate voltage and the force on the nanotube. One can see that there is a very good agreement with the experimental results.

After these first pioneering experiments, much work has been done on suspended carbon nanotubes. For example we remember experiments on heavily disordered single-wall carbon nanotubes [56, 57, 58], electromechanical coupling to the nanotube's breathing [59], stretching [60], and bending modes [61] and detection of motion of a suspended carbon nanotube through cantilevers [62].

One of the clearest proofs of the back-action of single-electron transport on the mechanical degrees of freedom is the observation of a weak softening of the mode as a function of the gate voltage around the degenerate point. In 2009, it became possible to observe this effect for the first time [63, 64].

This paved the way for a completely new series of effects and applications, such as very-high quality factors resonators [65, 66] and observation of phenomena related to the non-linear behavior of the mechanical oscillator [30, 18].

In the same year, working with bending modes, a system with a double quantum dot was realized [67]: The CNT is suspended over three different gates and the central gate can be used to create a potential barrier in the middle of the nanotube. This creates one quantum dot to the right of the barrier and one to its left.

Still in 2009, the same group also showed the possibility of working at very low temperatures [68]. This allowed for a big leap of two orders of magnitude in the quality factor

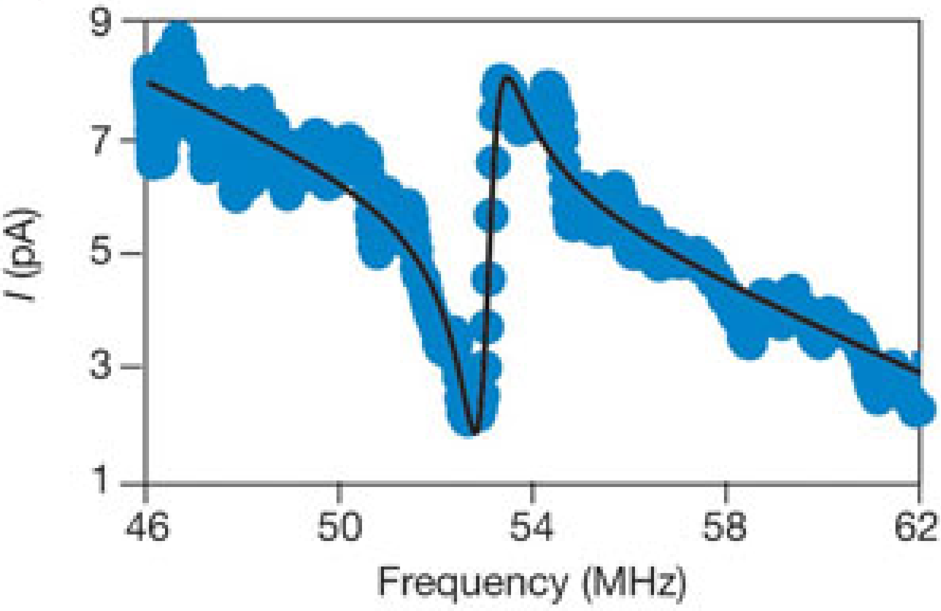

Figure 1.4: The current through the junction against the driving frequency: The current has a resonance, for which the fitted frequency gives 55 MHz. This is a clear indication of the interaction between electronic system and mechanical one and the first detection of mechanical displacement through electric measurement. Adapted from 10.

of the resonator, which is in those two papers reported to be around 10^5. A high quality factor has at least two very important consequences: (1) The system has a very narrow spectral line, which is an essential prerequisite, for example, for force sensors; it allows for a great sensitivity in the measure of the reaction of the system at different frequencies. (2) The information that is stored in the resonator is kept for a long time, with interesting applications in information theory.

In the following, we will focus essentially on the applications to sensing experiments.

1.3.2 Sensing experiments

Bachtold and co-workers published a first paper in 2008 where they present a doubly-clamped suspended carbon nanotube that can be used to measure masses down to 25×10^{-21} g at room temperature and to 1.4×10^{-21} g at 5 K, thanks to the high Q-factor and low mass of the carbon nanotube [3]. In their experiment, they bombard the carbon nanotube with chromium atoms; some of the atoms can be adsorbed by the carbon nanotube, changing thus the effective mass m_{eff} of the resonator and, ultimately, its resonance frequency ω_0. In a simple linear model of the harmonic oscillator, the relation $k = m_{\text{eff}}\omega_0^2$, where k is the spring constant, holds. Since the value of k is constant, the relation between the mass increase δm and the frequency decrease $\delta\omega_0$ reads

$$\delta m = \frac{2m_{\text{eff}}}{\omega_0}|\delta\omega_0|. \tag{1.3}$$

The resonance frequency is estimated driving the nanotube with an oscillating gate voltage and measuring the electric current as a function of the driving frequency (the same method as ref. [10]). The mass resolution m_R, i.e. the smallest mass variation that

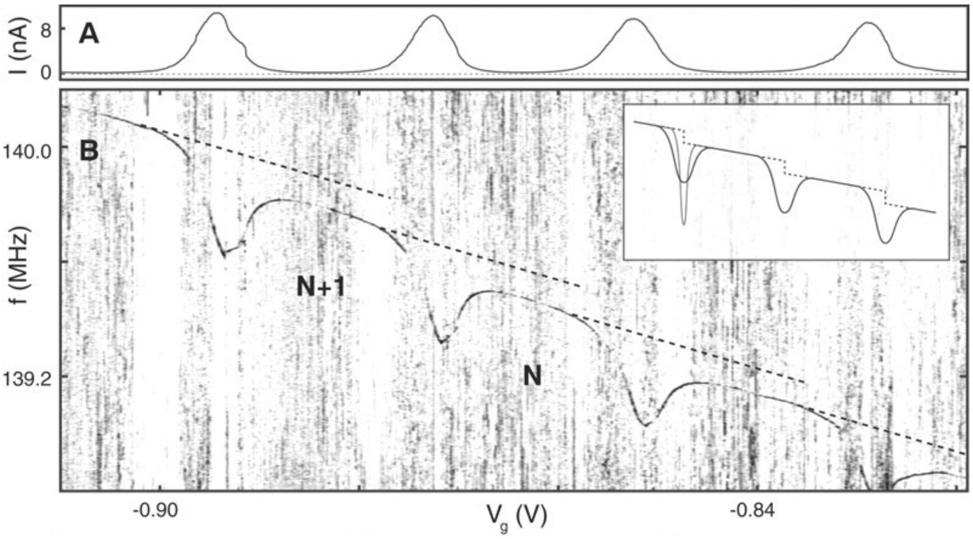

Figure 1.5: Single-electron tuning. (A) Nanotube current versus gate voltage showing single-electron tunneling at the peaks and Coulomb blockade in the valleys. This curve is taken from (B) at f = 138.8 MHz. (B) Normalized resonance signal versus driving frequency and gate voltage (Vsd = 1.5 mV). The tuned mechanical resonance shows up as the darker curve with dips at the Coulomb peaks. The offsets between the dashed lines indicate the frequency shift due to the addition of one electron to the nanotube. The resonance frequency also shows dips caused by a softening of the spring constant because of single-electron charge fluctuations. N, number of holes on the quantum dot. (Inset) The expected resonance behavior. Adapted from 64.

the system can effectively measure, is given by the width of the resonance in the frequency spectrum $\Delta\omega = \omega_0/Q$, which leads to

$$m_R = \frac{2m_{\text{eff}}}{Q}. \tag{1.4}$$

A very low mass and a very high quality factor are then useful for reducing the mass resolution, yielding thus a better sensor.

A subsequent work [38] improves on these results by using a carbon nanotube with a shorter suspended length, cleaned thoroughly with a so-called annealing process: In the annealing process, a large current is sent through the nanotube. This current induces all the atoms and molecules attached to the nanotube to leave, regenerating its properties to the original state. The annealing process works particularly well with carbon nanotubes because they can sustain very large currents without structural damage, unlike other NEMS. The improvements on the results of the previous paper are so big that the resolution has improved of three orders of magnitude: at 5 K, it jumped to 1.7×10^{-24} g, roughly the mass of a single proton!

The same group also worked on force sensitivity [7], for which a similar albeit more complicated sensing mechanism is required. The idea is to compare the frequency response of the system under a small driving with the response due to thermal fluctuations; the smallest detectable force represents the resolution of the system.

The scheme used is represented in Figure 1.6. The electric current that passes through the suspended carbon nanotube is connected to an electric circuit made of a resistance R, of two op-amps, and of a FFT analyser. The resistance converts the electric signal to a voltage signal following Ohm's law $V = IR$. This voltage signal is then sent to both op-amps that independently amplify it. The two amplified signals are then cross-correlated by the FFT analyser. The noise introduced by the op-amps is cut away from the output

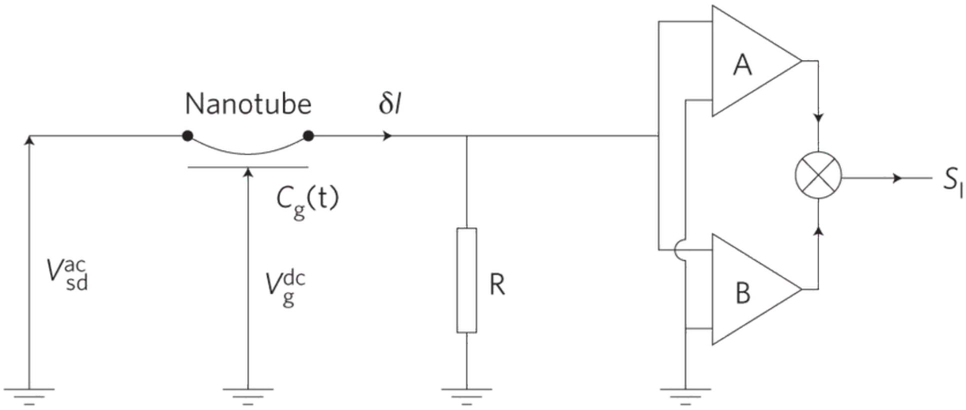

Figure 1.6: The electronic scheme of the device used for force sensing experiments. R is the resistance that transforms the current signal δI into a voltage signal δV, which is then independently amplified by two op-amps (triangles A and B to the right) and finally cross-correlated with a FFT analyser (crossed circle) to obtain S_{II}. Adapted from [7].

of the analyser because it is uncorrelated (the two op-amps work independently), leaving only the electromechanical correlation signal S_{II} as the output of the system. The spectral noise is then defined as

$$S_{II} = \frac{\langle \delta I^2(t) \rangle}{\mathrm{rbw}}, \tag{1.5}$$

where rbw is the resolution bandwidth and $\langle \delta I^2(t) \rangle$ is the mean square Fourier component of the time-averaged current cross-correlation at frequency $|\omega_{sd} - \omega_m|$ (ω_{sd} being the bias-voltage frequency and ω_m the mechanical resonance frequency, as usual).

The sensitivity can be further improved by using a very soft carbon nanotube, that is, one that stretches over a length of several micrometers: An increase in the softness corresponds to an increase in the electromechanical response, while the purely electronic one is unaffected.

The driving is put through the gate and at the frequency ω_m of the mechanical resonance. In the response of the system, it is seen as a sharp δ-like peak that sits on top of the thermal fluctuations (see Figure 1.7).

Once the frequency response is obtained, the force sensitivity is defined as the square root of

$$S_F = \frac{\text{thermal resonance height}}{\text{driven peak height}} \times F_d^2/\mathrm{rbw}, \tag{1.6}$$

where F_d is the driving force. We can see that it depends on the resolution bandwidth of the electronic circuit, which is independent on the NEMS.

The authors declare a sensitivity of $12(8) \times 10^{-21}\,\mathrm{NHz}^{1/2}$ at a temperature of $1.2\,\mathrm{K}$, that they claim to be 40 times smaller than the previous record.

1.3.3 Decoherence in a carbon nanotube

The quality factor of the mechanical oscillator is a fundamental physical quantity, since the sensing capabilities of the NEMS heavily depend on it. It is thus obvious to try to increase it as much as possible.

A few years ago a carbon nanotube with a quality factor of 5 millions, more than one

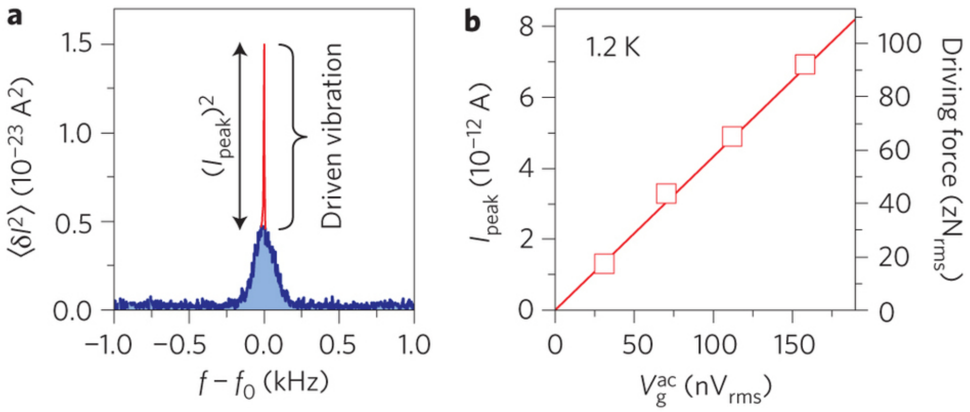

Figure 1.7: Panel (a): Current spectrum, with the driven signal (in red) on top of the thermal fluctuations' signal (blue area). The driven signal is essentially a delta peak of height $(\delta I)^2$ that starts from the top of the thermal fluctuation peak. Panel (b): The (linear) dependence between driving force, realized with an oscillating gate voltage, and electric current δI. Adapted from [7].

order of magnitude larger than the previous record, was presented [66]. However, this result was achievable only during short measurements: if the experiment time is too long, frequency fluctuations occur and determine a much larger frequency distribution of the peak, that reduces thus the quality factor. The authors associate frequency fluctuations with the electrostatic noise of the environment, suggesting that a lower temperature helps to reduce them (hence their measurement at a temperature of 44 mK).

However, a contribution to frequency fluctuations possibly comes from intrinsic nonlinearities of the system, that become paramount at strong electromechanical couplings [18, 69]. In a nonlinear system, the period of the oscillation is a function of its amplitude; thermal fluctuations of the amplitude thus lead to frequency fluctuations. To measure the effect of decoherence, the authors of Ref. [69] measure the spectral response of a driven carbon nanotube and the quadrature signal during the ring-down time and show that the two are not compatible if one takes into account only the dissipation.

The system they work with is a standard suspended carbon nanotube clamped at both extremities, of the type we have already described. They drive the nanotube through an oscillating gate voltage with driving frequency ω_d; the driving is then set off at time $t = 0$ and the oscillator is let evolve freely.

In order to measure the electric current they insert a slightly detuned probe signal and make use of the mixing technique that we explained before. It is important to remark that the probe has no effect on the movement of the carbon nanotube when the detuning is larger than the linewidth of the nanotube.

The driving is modeled by a force $F(t) = F_d \cos(\omega_d t)\theta(-t)$, where $\theta(-t)$ is the step function that is 1 for negative times and 0 for positive ones. The force $F(t)$ enters the equation of motion of the system for the displacement $x(t)$:

$$m\ddot{x}(t) + m\gamma\dot{x}(t) + kx(t) = F(t), \tag{1.7}$$

where γ is an electron-dependent dissipative part that comes from retardation effects. (We will derive this equation in chapter 2.) The solution to this equation yields

$$x(t) = \begin{cases} t \leq 0, & X(t)\cos(\omega_d t) + Y(t)\sin(\omega_d t) \\ t > 0, & X(t)\cos(\omega_m t) + Y(t)\sin(\omega_m t) \end{cases}, \tag{1.8}$$

where it is worthy to notice that for negative times the oscillator evolves with the driving frequency ω_d, while for positive times it evolves with the bare mechanical frequency ω_m. The coefficients $X(t)$ and $Y(t)$ are called the quadrature coefficients and their expression is

$$X(t) = \begin{cases} t \leq 0, & X_d \\ t > 0, & X_d e^{-\gamma t/2} \end{cases} \qquad Y(t) = \begin{cases} t \leq 0, & Y_d \\ t > 0, & Y_d \frac{\omega_d}{\omega_m} e^{-\gamma t/2} \end{cases} \quad . \tag{1.9}$$

For negative times, the authors measure the output current as a function of the driving frequency ω_d with the standard mixing technique. The quality factor Q_S is then defined as the ratio between the resonance frequency and its linewidth, $Q_S = \omega_m/\Delta\omega$.

For positive times, instead, there is no driving frequency, so they just measure the mixing current, from which they infer the quadrature coefficients $X(t)$ and $Y(t)$; the quadrature coefficients just give information on the amplitude of the oscillation, disregarding its phase: they are thus influenced *only* by the energy dissipation of the system; their decay is then fitted with an exponential function to derive a second *quality factor* defined as $Q_R = 2\omega_m/\gamma$.

The two quality factors, Q_S and Q_R, should be equal when the dephasing is not important. This is verified for small driving powers, when $Q_R = Q_S = 6250$ in their experiments. For higher driving, however, they find $Q_R = 6140$ and $Q_S = 1410$, which shows that a dephasing is taking place.

In chapter 3 we will discuss at length about the difference between the dissipation of the system and the width of the spectral response of the oscillator, proposing a source for frequency and phase noise that could explain the effect.

1.3.4 A novel fabrication technique

Recently, the group led by S. Ilani at the Weizmann Institute of Science in Israel presented a novel fabrication technique described in [31]: Briefly, they avoid disorders caused by interferences in the realization process of the nanotube and of the electronic circuit by creating two separate chips and *mating* them. The process is described in Fig. 1.8.

As a result, they have a carbon nanotube suspended above several separate gates that can be individually tuned with an impressive level of control. For example, they can set any one of the gates to induce an electron doping on the CNT, while all the others induce hole doping; this creates a quantum dot above the electron-doped gate that is locally constrained by the presence of a potential barrier above the other gates. This potential barrier also determines the intensity of the electronic tunneling coupling to the leads Γ. Alternatively, they can create multiple dot configurations, tailoring the height of the potential barriers in order to obtain the desired electromechanical parameters.

Reference [32] gives a much more in-depth analysis of the spatial dependence of the mechanical oscillation of the system for varying configurations. Using the mating approach, they create a system where a CNT is suspended above 5 gates. For each gate, they study how different resonance modes influence the softening of the system: They show a quadratic dependence of the softening on the amplitude of oscillation, which justifies that intuitive idea that the effect of the electromechanical coupling is larger where the displacement of the nanotube is larger (see Figure 1.9).

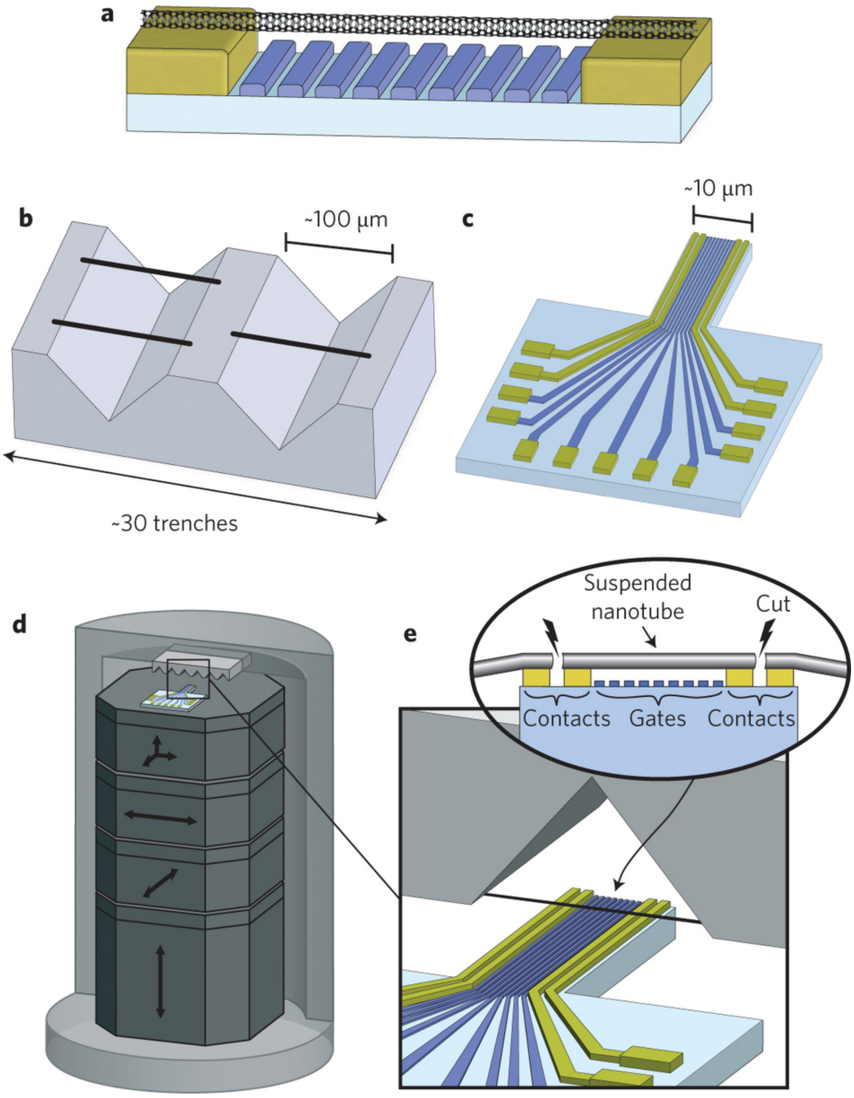

Figure 1.8: The *mating* fabrication technique presented in [31]. Panel a: The final result. Panel b: The first chip, consisting of a set of nanotubes suspended over trenches. Panel c: The second chip, that contains the electronic part – electrodes and the desired number of gates. Panel d: A scanning probe microscope is used to approach the electronic chip to one nanotube and measure its characteristics. Panel e: When a nanotube with the desired characteristics is found, it is cut and attached to the electronic chip.

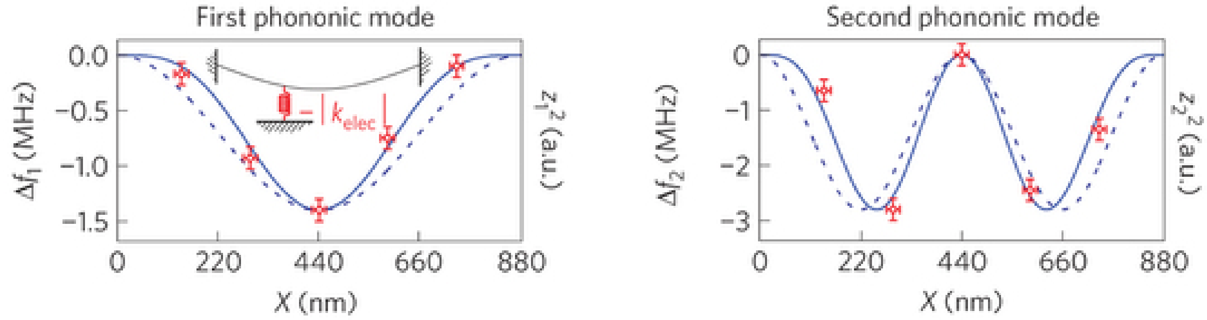

Figure 1.9: The spatial dependence of the softening of the oscillator in when exciting the first or the second phononic mode along a CNT with a length of 880 nm. Red crosses: softening of the oscillator (in MHz). Solid lines: shape of the corresponding phononic mode treating the carbon nanotube as a solid rod. Dashed lines: same as solid lines, but with a string model for the nanotube. A high correlation between the shape of the mechanical resonance and the softening is exhibited. Adapted from [32].

Following the supplemental material of the paper, this can be understood using the wave equation

$$\left[\hat{D} + k_{\text{elec}}\delta(z - z_0)\right] x(z) = \mu\omega^2 x(z) \tag{1.10}$$

that determines the oscillation frequency of the system ω at any point z along the nanotube. Here, x is the amplitude of oscillation, μ is the linear mass of the system, $\hat{D}$ is the differential Euler-Bernoulli operator that gives the oscillation frequency of the system in the absence of electromechanical coupling, z_0 is the position of the gate along the nanotube, and $k_{\text{elec}} = -dF_e/dx$ is the softening due to the electromechanical force F_e (see the following chapter for a derivation of this softening). Using the fact that the bare system oscillates at frequency ω_0, we can say that $\hat{D}x(z) = \mu\omega_0^2 x(z)$. Substituting it in Eq. (1.10) and multiplying by $x(z)$ both sides we obtain

$$k_{\text{elec}}\delta(z - z_0)x^2(z) = \mu(\omega^2 - \omega_0^2)x^2(z)\,, \tag{1.11}$$

which can be integrated over all positions z to finally obtain

$$k_{\text{elec}}x^2(z_0) = \mu(\omega^2 - \omega_0^2)\int_0^L x^2(z)dz\,. \tag{1.12}$$

Now, we define $x(z) = X\xi(z)$, where X is the amplitude of the mode and $\xi(z)$ is its shape. Thanks to that, we can simplify X^2 on both sides. The integral on the right-hand side becomes

$$\int_0^L \xi^2(z)dz = cL\,, \tag{1.13}$$

where c is a numerical factor depending on the details of the shape but close to one.

Putting it all together, defining the total mass $m = \mu L$, the mechanical spring constant $k = m\omega_0^2$, and in the limit of small softening $\omega - \omega_0 \equiv \Delta\omega \ll \omega_0$, we obtain

$$k_{\text{elec}}\xi^2(x_0) = 2c\,\mu L\,\omega_0\Delta\omega \implies \frac{\Delta\omega}{\omega_0} = \frac{k_{\text{elec}}}{2c\,k}\xi^2(z_0)\,. \tag{1.14}$$

This approach allows for a finer study of the dependence of the coupling with the position of the gate electrode. In the case of strongly coupled systems, it can be used, for example, to study the bistable and monostable regimes of a single nanotube by placing the gate in different positions.

In the same paper, Ilani and coworkers also show the possibility of creating a double quantum dot system: Labeling the gates 1 to 5 from left to right, they put an electron doping above gates 2 and 4, and a hole doping above 1, 3, and 5. This approach can be modified by increasing the doping on gates 1 and 5 so that electrons can't tunnel in and out of the nanotube, but internal tunneling between the two quantum dots is still possible. The advantage is that, while an electromechanical coupling is still conserved, the system is succesfully decoupled from the main source of external noise, that is the thermal bath in the external electrodes. The authors claim that the system they use has promising perspective for quantum information and for the study of fundamental phonon-electron interaction, such as superconductivity, ferroelectricity, or Peierls and Jahn-Teller instabilities.

Chapter 2

The model

The system we study is made of a carbon nanotube suspended between two conducting leads, the source and the drain, and above a gate (see Figure 2.1, panel **a**). The nanotube is clamped on the leads by means of the interposition of an oxide that acts as a glue; if the nanotube is semiconducting a Schottky barrier is created, but it is still possible for an electron to tunnel from the lead to the nanotube and vice versa. When one additional electron is placed on the nanotube, it interacts with the electrons on the gate electrode; the nanotube then moves vertically to minimize the energy of the system. The dynamics of the system is quite complex since the electronic interaction changes with the position of the nanotube, but it allows one to obtain mechanical information from current measurement. The remarkable properties that we discussed in the previous chapter allow for very high sensitivity in the measurement, making carbon nanotubes an ideal sensor of motion, force, and mass.

2.1 The electromechanical coupling

The coupling between electrons and movement of the nanotube can be modeled by a capacitive coupling between the CNT and the gate electrode, as can be seen in Figure 2.1, panel **b**. The gate electrode and the nanotube, being separated by an insulator (vacuum or air), can be regarded as a capacitor; its geometry is variable, since the nanotube can move, and so is its capacitance. Also the interface between the nanotube and the source (drain) electrode can be regarded as a capacitor, but, being parallel to the displacement of the nanotube, its capacitance is constant.

The variation of the total potential energy of the three capacitors with the displacement is then linked to the electromechanical force by the formula

$$F_e(x) = -\frac{dU_e(x)}{dx} \tag{2.1}$$

where $U_e(x)$ is the electrostatic energy. Defining $U_e(x)$ requires a bit of subtlety: One would think that it is the sum of the potential energy of the three capacitors, but that is not enough because the electrons inside the island repel each other. We then derive $U_e(x)$ from the electric potential of the island $\varphi(x)$; but again subtlety is required, since $U_e(x) \neq Q\ \varphi(x)$, where Q is the charge (we would commit the same mistake we are trying to correct!): the electric potential is determined by the charge Q, so that the first charge

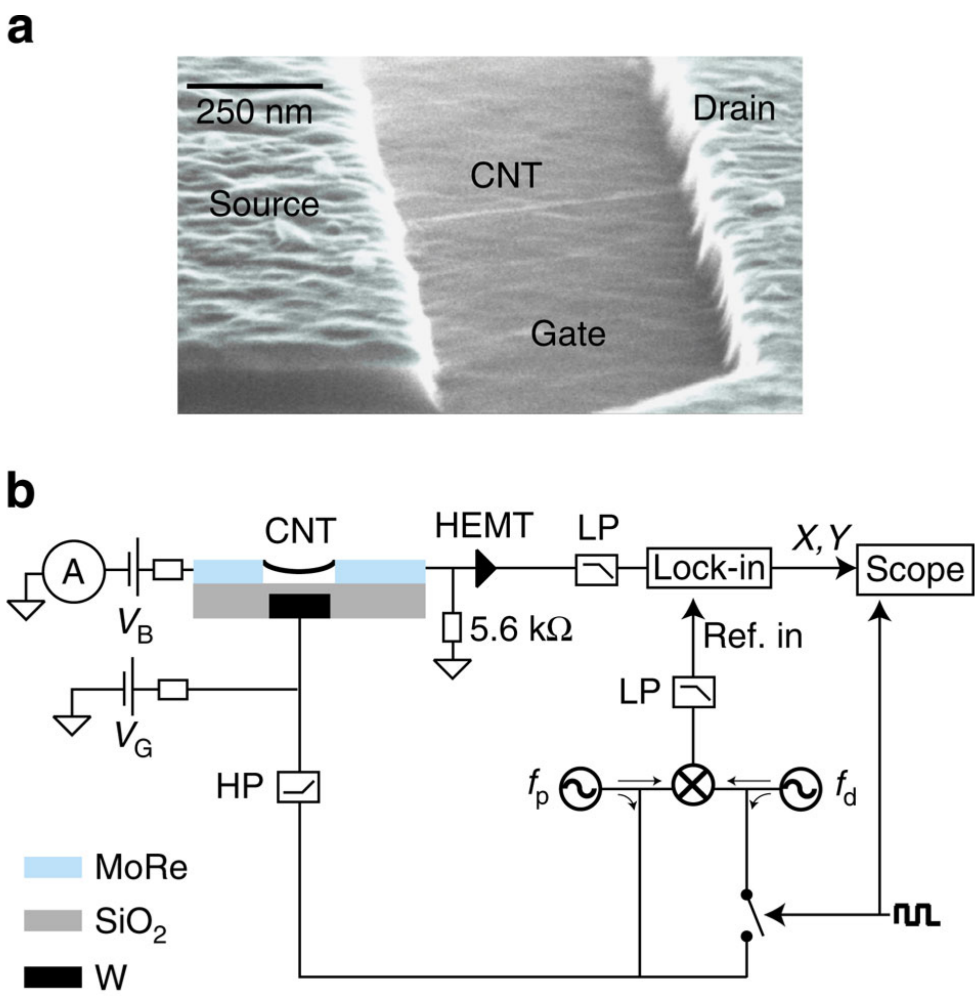

Figure 2.1: The experimental apparatus of [69], which is equivalent to the system we are studying. Panel **a**: A scanning electron microscope image of the device; the CNT is the thin white line between source and drain. Panel **b**: The electrical scheme of the device. The carbon nanotube is represented as the bent line between source and drain electrodes; the system created by the CNT and the gate plate (the black rectangle below the CNT) can be regarded as a capacitor: When the CNT moves along the vertical axis x, the geometrical properties of the capacitor are modified, altering the value of the capacitance $C_g(x)$. More details in the cited paper.

dQ entering the island feels a potential $\varphi(x, Q = 0)$, the second one feels $\varphi(x, Q = dQ)$ and so on and so forth. In the limit for which there are lots of electrons inside the island, we can send dQ to zero and perform an integral. We obtain:

$$U_e(x, Q) = \int_0^Q \varphi(x, Q')dQ'. \tag{2.2}$$

All that is left, now, is to find the potential on the island as a function of the charge inside the island, which is opposite to the charge around it due to the capacitive coupling. From electrostatics we obtain

$$Q = -\sum_i Q_i = -\sum_i C_i (V_i - \varphi), \tag{2.3}$$

where $i = g, s, d$ is an index that accounts for gate, source, and drain electrode, C_i is an electrode capacitance, and V_i is an electrode potential. From this follows

$$\varphi = \frac{\sum_i C_i V_i + Q}{\sum_i C_i} \equiv \frac{q + Q}{C_\Sigma}, \tag{2.4}$$

where we defined $q = \sum_i C_i V_i$ and $C_\Sigma = \sum_i C_i$. Mixing together Eq. 2.2 and 2.4 we obtain:

$$U_e(x,Q) = \frac{qQ}{C_\Sigma} + \frac{Q^2}{2C_\Sigma}. \tag{2.5}$$

From Eq. (2.5) we can find the charge at equilibrium by imposing that it minimizes the potential energy:

$$\frac{dU + e(x,Q)}{dQ} = \frac{q}{C_\Sigma} + \frac{Q}{C_\Sigma} = 0 \iff Q = -q. \tag{2.6}$$

We point out that this has been obtained in the limit of continuous charge. In the opposite limit of discrete electrons, the charge $Q = -N|e|$ is quantized, while $q = \sum_i C_i V_i$, being not a real charge but just a parameter, can take fractional values. Therefore, the condition $Q = q$ can not be satisfied in the general case; the charge that minimizes the potential energy is then be the integer number of electrons closest to q. Typically, $q \approx (N+1/2)|e|$, where $N \gg 1$, and the levels $Q = -N|e|$ and $Q = -(N+1)|e|$ are the only important ones in the problem.

We can now compute the force. From Eq. (2.5), using $\partial C_\Sigma/\partial x = C_g'$ and $\partial q/\partial x = C_g' V_g$:

$$\begin{aligned} F_e(x,Q) &= -\frac{\partial U_e(x,Q)}{\partial x} = -\frac{Q}{C_\Sigma}\frac{\partial q}{\partial x} + \frac{qQ}{C_\Sigma^2}\frac{\partial C_\Sigma}{\partial x} + \frac{Q^2}{2C_\Sigma^2}\frac{\partial C_\Sigma}{\partial x} \\ &= -\frac{C_g'}{C_\Sigma} Q V_g + \frac{C_g'}{2C_\Sigma}\frac{Q+2q}{C_\Sigma} Q\,. \end{aligned} \tag{2.7}$$

Since just two levels enter the dynamics ($Q_0 = -N|e|$ and $Q_1 = -(N+1)|e|$), we can rewrite the force as:

$$F_e(x,Q) = F_e(x,Q_0) + F_0(x) n, \tag{2.8}$$

where $F_0(x)$ is the difference between the force in levels Q_1 and Q_0, while n is 0 when the system is in state Q_0 and 1 otherwise. Solving for $F_0(x)$ we obtain:

$$F_0(x) = \frac{C_g'}{C_\Sigma} e \left[V_g - \frac{2q - (2N+1)e}{C_\Sigma} \right] \approx \frac{C_g'}{C_\Sigma} e V_g, \tag{2.9}$$

where the last relation is a strictly equality if the system is exactly at the degeneracy point $q = (n+0.5)|e|$.

Since we are interested only in the difference between the two levels, we will just keep $F_e(x) \equiv F_0(x) n$. For small displacements of the carbon nanotube, we will also approximate $F_0(x)$ with its value at the equilibrium point F_0. The electromagnetic interaction energy can thus be rewritten as

$$U_e(x) \approx -F_0 x\ n. \tag{2.10}$$

2.2 Hamiltonian of the system

Once the interaction between the nanotube and the leads is known, one can write a Hamiltonian for the system. First of all, to simplify the notations, we neglect the spin degrees of freedom and set the electron charge e, the Planck constant $\hbar$, and the Boltzmann constant k_B to 1. Now, from a formal point of view, one can divide the Hamiltonian of the system in three parts: electronic, mechanical, and interaction.

$$H = H_e + H_m + H_I \,. \tag{2.11}$$

The leads are two large pieces of metal that can be considered to be at thermal equilibrium at all times. The energetic levels inside the carbon nanotube depend on several parameters. In particular, the size of the nanotube and the eventual presence of additional gates can confine the electrons to a small region; the energetic levels inside the nanotube become discrete. In our model we consider spinless electrons and just one electronic level inside the carbon nanotube that can be either empty, thus available for electrons to jump in, or full, from which electrons can jump out. Therefore, the carbon nanotube is considered to be in the regime of *quantum dot.* The electronic Hamiltonian becomes thus:

$$H_e = \sum_{\alpha=L,R} \sum_k \left[(\epsilon_{\alpha k} - \mu_\alpha) c^\dagger_{\alpha k} c_{\alpha k} + \sum_k t_\alpha c^\dagger_{\alpha k} d \;+ \text{h.c.} \right] + \varepsilon_0 d^\dagger d \;\;,$$

where $\alpha =$ L, R is to select left or right lead, $\epsilon_{\alpha k}$ is the electronic spectrum in the α lead, μ_α the chemical potential, ε_0 is the electronic level inside the quantum dot in the absence of electromechanical interaction, and c and d are the appropriate destruction operators for electrons in the lead and the dot respectively.

When the quantum dot interacts with the leads, its sharp electronic level becomes broader. Its width can be calculated starting from this Hamiltonian and is given by $\Gamma_\alpha \equiv \pi t_\alpha^2 \rho_\alpha$, with ρ_α the density of states of the α lead. The effect of left and right lead can be summed together to obtain the total expression of the width $\Gamma = \Gamma_L + \Gamma_R$. We will typically assume that the system is symmetrically coupled to the leads, so that $\Gamma_L = \Gamma_R = \Gamma/2$, and that the zero in energy is defined by the average of the Fermi energy of the two leads, $\mu_L = V/2 = -\mu_R$.

For the mechanical part, we model the nanotube as a guitar string with an infinite impedance on the borders (or equivalently with perfectly fixed extremes), and take the standard linear approximation of the recall force. The nanotube becomes thus a harmonic oscillator with a typical resonance frequency ω_0 and whose Hamiltonian is described by

$$H_m = \frac{p^2}{2m} + \frac{kx^2}{2} \,,$$

where m is the effective mass of the mode and $k = m\omega_0^2$ is the effective spring constant. The motion of the nanotube is fully described by the variables x, the position, and p, the momentum. We will assume that the energy of a single phonon is very small, so that the oscillator can be treated classically due to the large number of phonons that populate the system. As we have already seen, this has been proved true provided that $\omega_0 \ll \max(T, V)$ [13]: Even at zero temperature, the presence of a bias voltage acts as an effective temperature on the system, exciting the nanotube.

Finally, the interaction Hamiltonian has already been written in Eq. 2.10:

$$H_I = -F_0 x \; d^\dagger d \;\;.$$

The result is known as the Anderson-Holstein Hamiltonian:

$$
\begin{aligned}
H = \sum_{\alpha=L,R} \sum_{k} \Big[(\epsilon_{\alpha k} - \mu_\alpha) c^\dagger_{\alpha k} c_{\alpha k} + t_\alpha c^\dagger_{\alpha k} d \ + \text{h.c.} \Big] \\
+ (\varepsilon_0 - F_0 x) d^\dagger d \ + \frac{p^2}{2m} + \frac{k x^2}{2} \, .
\end{aligned}
\tag{2.12}
$$

A scheme of the energetic levels is given in Figure 2.2.

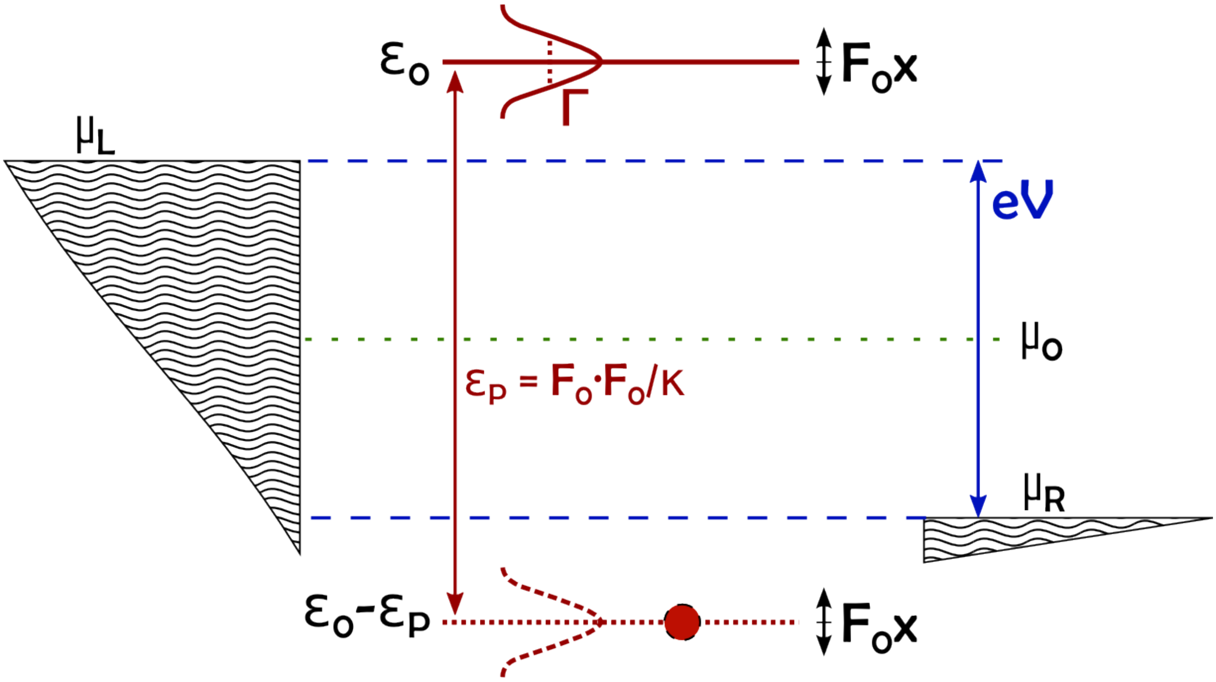

Figure 2.2: The scheme of the electronic levels inside the system. The triangles on the sides represent the metallic leads, while the central levels represent the energy of the state inside the carbon nanotube with one additional electron (bottom), or with no additional electrons (top). The system is in the regime of symmetric gating and strong coupling but, in order to clearly show all the parameters of the system, we have taken a large value of the bias voltage V, in contrast with the choice we do in the body of the thesis. In the situation depicted here, both electronic states are well outside the transition window determined by the Fermi energies of the adjacent leads: when the dot is occupied, the energy of the electron in the dot is too low to find any available state in the leads to go to, and vice versa when the dot is unoccupied the energy of the empty state is too high to find any electron in the leads to enter. Therefore, the electric current is blocked. Adapted from [15].

Our goal is now to describe the motion of the carbon nanotube. However, $x(t)$ is always a stochastic quantity due to the thermal fluctuations of the system because, even when the external temperature is set to zero, the passage of electrons generates an effective temperature in the mechanical subsystem. Therefore, we characterize the distribution of position of the oscillator through its mean value $\langle x(t) \rangle$ and its autocorrelation function $\langle x(t) x(0) \rangle$. The rest of this chapter is devoted to the resolution of the equation of motion for the oscillator and to the finding of the stationary probability distribution of the system, from which we will derive all the physical properties of the system in the next chapter.

2.3 The Born-Oppenheimer approximation and the dynamics of electrons

Since we look at the bending modes of the carbon nanotube, the typical mechanical resonance frequency $\omega_0 \approx 100\,\mathrm{MHz}$ is often much smaller than the typical tunneling rate of electrons $\Gamma \approx 10\,\mathrm{GHz}$. This means that we can have an approximate solution by solving the electronic problem at a fixed position x of the carbon nanotube before calculating its effect on the mechanical motion, following the idea of the Born-Oppenheimer approximation in solids where the electronic problem is solved for a fixed position of the ions.

In the following, we solve the electronic problem using the input-output theory. This theory has been succesfully used especially in optomechanics [70, 71] for describing the evolution of photons. We present here an adaptation for an electromechanical system, where it is used to describe electrons instead.

2.3.1 Dynamics of the electron operators

The equation of motion for the operators d and $c_{\alpha k}$ are:

$$\dot{d}(t) = i[H_e, d(t)]; \qquad \dot{c}_{\alpha k}(t) = i[H_e, c_{\alpha k}(t)]\,.$$

Making use of the standard anti-commutation rules for fermionic operators, one can show that the previous set of equations becomes:

$$\begin{cases} \dot{d}(t) & = -i\epsilon_d \; d(t) - i\sum_{\alpha k} t_\alpha^* \; c_{\alpha k}(t) \\ \dot{c}_{\alpha k}(t) & = -i\epsilon_{\alpha k} \; c_{\alpha k}(t) - it_\alpha \; d(t) \end{cases}, \tag{2.13}$$

where $\epsilon_d = \varepsilon_0 - F_0 x$ is the instantaneous effective energy of the electronic level inside the nanotube. A further simplification can be achieved by defining the operators $\tilde{d}(t)$ and $\tilde{c}_{\alpha k}(t)$ that take into account the deterministic evolution of the isolated system. Introducing the energy difference $\Delta_{\alpha k} = \epsilon_{\alpha k} - \epsilon_d$, the equations of motion become:

$$\begin{cases} \tilde{d}(t) & \equiv e^{i\epsilon_d t} d(t) \\ \tilde{c}_{\alpha k}(t) & \equiv e^{i\epsilon_d t} c_{\alpha k}(t) \end{cases} \Longrightarrow \begin{cases} \dot{\tilde{d}}(t) & = -i\sum_{\alpha k} t_\alpha^* \; \tilde{c}_{\alpha k}(t) \\ \dot{\tilde{c}}_{\alpha k}(t) & = -i\Delta_{\alpha k} \; \tilde{c}_{\alpha k}(t) - it_\alpha \; \tilde{d}(t) \end{cases} \tag{2.14}$$

We can solve the second equation in 2.14 via the method of the variation of parameters and put the result we find inside the first equation. The solution obtained, written for an initial time $t_0 = 0$, is:

$$\tilde{c}_{\alpha k}(t) = -it_\alpha \int_0^t e^{-i\Delta_{\alpha k}(t-t')} \tilde{d}(t') dt' + e^{-i\Delta_{\alpha k} t} \tilde{c}_{\alpha k}(0)\,, \tag{2.15}$$

$$\dot{\tilde{d}}(t) = \sum_{\alpha k} \left[-|t_\alpha|^2 \int_0^t e^{-i\Delta_{\alpha k}(t-t')} \tilde{d}(t') dt' - it_\alpha^* e^{-i\Delta_{\alpha k} t} \tilde{c}_{\alpha k}(0) \right]. \tag{2.16}$$

Since the leads are metallic contacts, the summation over k can be replaced by an integration over the energy by defining the density of states of the system: $\rho_\alpha(\nu_\alpha) = \sum_k \delta\left(\nu_\alpha - \Delta_{\alpha k}\right)$. Since we are well inside the conduction band of the metal, we are allowed to use the *wide band approximation*, i.e. to consider the density of states to be flat. Remembering that $\Gamma_\alpha = \pi |t_\alpha|^2 \rho_\alpha$, as we defined it in the previous section, the summation over k in the first term of the right hand part of Eq.2.16 brings to [1]:

$$\sum_k |t_\alpha|^2 \int_0^t e^{-i\Delta_{\alpha k}(t-t')} = 2\Gamma\ \delta(t-t')\,.$$

To simplify the second term we need to take into account the dependency on time of the $\tilde{c}_{\alpha k}$ operators. In order to treat it, we define the *total incoming field of electrons* from the α lead,

$$c_{\alpha,\mathrm{in}}(t) = \sum_k e^{-i\epsilon_{\alpha k} t} c_{\alpha k}(0)\,; \tag{2.17}$$

$$\tilde{c}_{\alpha,\mathrm{in}}(t) = e^{i\epsilon_d t}\ c_{\alpha,\mathrm{in}}(t) = \sum_k e^{-i\Delta_{\alpha k} t} c_{\alpha k}(0)\,. \tag{2.18}$$

Taking out the phase part in the tunnel matrix element, $t_\alpha = |t_\alpha|\ \exp(-i\phi_\alpha)$, eq.2.16 can be rewritten as:

$$\dot{\tilde{d}}(t) = -\Gamma \tilde{d}(t) - \sum_\alpha i\ e^{-i\phi_\alpha} \sqrt{\frac{\Gamma_\alpha}{\pi\ \rho_\alpha}}\ \tilde{c}_{\alpha,\mathrm{in}}(t)\,,$$

that we solve in Fourier transform:

$$\begin{cases} \tilde{d}(\omega) & = -i\chi(\omega) \sum_\alpha e^{i\phi_\alpha} \sqrt{\frac{\Gamma_\alpha}{\pi\ \rho_\alpha}}\ \tilde{c}_{\alpha,\mathrm{in}}(\omega)\,; \\ \tilde{d}^\dagger(\omega) & = i\chi^*(-\omega) \sum_\alpha e^{-i\phi_\alpha} \sqrt{\frac{\Gamma_\alpha}{\pi\ \rho_\alpha}}\ \tilde{c}^\dagger_{\alpha,\mathrm{in}}(\omega)\,; \end{cases}, \tag{2.19}$$

where we have defined the coefficient $\chi(\omega) = (i\omega + \Gamma)^{-1}$.

We remark here that we define $\tilde{d}^\dagger(\omega)$ as the adjoint operator of $d^\dagger(t)$. The importance of this remark is due to the adjunction and the Fourier transformation not commuting; this leads to the minus sign inside $\chi^*(-\omega)$.

As a final sidenote, we won't have to explicitly find $\tilde{c}_{\alpha,\mathrm{in}}(\omega)$.

2.3.2 Derivation of important physical quantities: number of electrons, its auto-correlator, and electric current

The back-action of the electronic subsystem on the mechanical oscillator is given by the force $F\ n(x,t)$, as we have seen in Sec. 2.1. This force varies on two different time scales: The fast time scale of electrons and the slow time scale of the mechanical oscillator. Since we are interested in the time evolution of the mechanical oscillator, it is convenient to express it as a slowly oscillating *average force* $F_0 n(t)$ plus a fluctuating residue $\xi(t)$, which is determined by the fluctuation of the number of electrons $S_{nn}(t)$.

Therefore, in this paragraph we compute $n(t)$ and $S_{nn}(t)$ starting from Eq. (2.19) for a fixed value of the oscillator position x.

---

[1] Without the wide band approximation, we would probably have a distribution in t with a finite width W given by the inverse of the typical energy scale of the band. However, $W \ll \omega_0^{-1}, \Gamma^{-1}$ and that we can treat it as zero, using the wide band approximation.

Thanks to Wick's Theorem and to the temporal translational invariance of the system, all the physical quantities can be derived starting from a fundamental function:

$$g(\tau) \equiv \left\langle d^\dagger(\tau)\ d(0) \right\rangle \Longrightarrow g(\omega) \equiv \left\langle d^\dagger(\tau)\ d(0) \right\rangle_\omega , \tag{2.20}$$

where the last term is the Fourier transform of $d^\dagger(\tau)\ d(0)$ with respect to the variable τ. From this follows:

$$\left\langle d^\dagger(\omega)\ d(\omega') \right\rangle = 2\pi\delta(\omega+\omega')\ g(\omega) . \tag{2.21}$$

A basic property of the Fourier transform says that $d(\omega) = \tilde{d}(\omega+\epsilon_d)$ and $d^\dagger(\omega) = \tilde{d}^\dagger(\omega-\epsilon_d)$. It follows that

$$\left\langle \tilde{d}^\dagger(\omega-\epsilon_d)\ \tilde{d}(\omega'+\epsilon_d) \right\rangle = 2\pi\delta(\omega+\omega')\ g(\omega) . \tag{2.22}$$

Putting Eq. (2.19) inside Eq. (2.22) we obtain:

$$|\chi(\omega-\epsilon_d)|^2 \sum_\alpha \frac{\Gamma_\alpha}{\pi\rho_\alpha} \left\langle \tilde{c}^\dagger_{\alpha,\mathrm{in}}(\omega-\epsilon_d)\tilde{c}_{\alpha,\mathrm{in}}(\omega'+\epsilon_d) \right\rangle = 2\pi\delta(\omega+\omega')\ g(\omega) , \tag{2.23}$$

and following the reasoning behind Eq. (2.21), we can write

$$\left\langle \tilde{c}^\dagger_{\alpha,\mathrm{in}}(\omega-\epsilon_d)\tilde{c}_{\alpha,\mathrm{in}}(\omega'+\epsilon_d) \right\rangle = 2\pi\delta(\omega+\omega')\ \left\langle c^\dagger_{\alpha,\mathrm{in}}(\tau)\ c_{\alpha,\mathrm{in}}(0) \right\rangle_\omega , \tag{2.24}$$

from which follows immediately

$$g(\omega) = |\chi(\omega-\epsilon_d)|^2 \sum_\alpha \frac{\Gamma_\alpha}{\pi\ \rho_\alpha} \left\langle c^\dagger_{\alpha,\mathrm{in}}(\tau)\ c_{\alpha,\mathrm{in}}(0) \right\rangle_\omega . \tag{2.25}$$

Therefore, in order to compute $g(\omega)$ we need the following:

$$\langle c^\dagger_{\alpha,k}(t) c_{\beta,k'}(0) \rangle_\omega = \delta_{\alpha,\beta}\delta_{k,k'}\delta(\omega-\epsilon_{\alpha k}) f_\alpha(\omega) \tag{2.26}$$

where $f_\alpha(\omega) = \left[1+e^{(\omega-\mu_\alpha)/T}\right]^{-1}$ is the Fermi distribution function. Making use of the definition in Eq.2.17, of the wide band approximation and of the thermal distribution of electrons in the leads, we finally have

$$g(\omega) = 2\,|\chi(\omega-\epsilon_d)|^2 \sum_\alpha \Gamma_\alpha\ f_\alpha(\omega) . \tag{2.27}$$

From this result, we can write a table of the four combinations one can make:

$$\begin{cases} \left\langle d^\dagger(\tau)\ d(0) \right\rangle_\omega = 2\,|\chi(\omega-\epsilon_d)|^2 \sum_\alpha \Gamma_\alpha\ f_\alpha(\omega) \\ \left\langle d^\dagger(-\tau)\ d(0) \right\rangle_\omega = 2\,|\chi(\omega+\epsilon_d)|^2 \sum_\alpha \Gamma_\alpha\ f_\alpha(-\omega) \\ \left\langle d(\tau)\ d^\dagger(0) \right\rangle_\omega = 2\,|\chi(\omega+\epsilon_d)|^2 \sum_\alpha \Gamma_\alpha\ [1-f_\alpha(-\omega)] \\ \left\langle d(-\tau)\ d^\dagger(0) \right\rangle_\omega = 2\,|\chi(\omega-\epsilon_d)|^2 \sum_\alpha \Gamma_\alpha\ [1-f_\alpha(\omega)] \end{cases} .$$

Now let's see how we can use this in order to find some physical quantities. The average number of electrons is defined as

$$\bar{n}(t) = \left\langle d^\dagger(t) d(t) \right\rangle . \tag{2.28}$$

We notice that $\bar{n}(t)$ is constant in our system: its value is equal to $g(t=0)$, so that it can be obtained by integrating the first element in the table above. We obtain:

$$\bar{n} = \int_{-\infty}^{+\infty} \frac{d\omega}{2\pi}\, 2 \cdot \frac{\Gamma_L f_L(\omega) + \Gamma_R f_R(\omega)}{\Gamma^2 + (\omega - \epsilon_d)^2}\,. \tag{2.29}$$

The second quantity we want to find out is the auto-correlation function of the number of electrons, $S_{nn}(\tau)$.

$$S_{nn}(\tau) = \langle n(\tau)\; n(0)\rangle - \bar{n}(t)\; \bar{n}(0)\,. \tag{2.30}$$

If we write down S_{nn} making use of the $d(t)$ and $d^\dagger(t)$ operators, we find a four-terms average. We can then apply Wick's theorem to this quantity and reduce it to the product of two two-terms averages. Remembering that the averages of two annihilation- or creation- operators give no contributions, one can write:

$$S_{nn}(\tau) = \left\langle d^\dagger(\tau) d(0)\right\rangle\; \left\langle d(\tau) d^\dagger(0)\right\rangle\,.$$

Going to the Fourier transform, the simple product in the definition above becomes a convolution product. The values in the table above then tell us that

$$S_{nn}(\omega) = \sum_{\alpha,\beta} \int_{-\infty}^{+\infty} \frac{d\omega'}{2\pi} \frac{2\Gamma_\alpha f_\alpha(\omega')}{\Gamma^2 + (\omega' - \epsilon_d)^2} \cdot \frac{2\Gamma_\beta \left[1 - f_\beta(\omega' - \omega)\right]}{\Gamma^2 + (\omega' - \omega - \epsilon_d)^2}\,.$$

Finally, let's compute the current. We define it as the derivative of the number of electrons on the left lead. Following Eq. (2.3.1), we have

$$I = \dot{N}_L = i\left[H_e, c^\dagger_{Lk} c_{Lk}\right] = i\left(t_L c^\dagger_{Lk} d\; - h.c.\right) = i\left(t_L \tilde{c}^\dagger_{Lk} \tilde{d}\; - h.c.\right) \tag{2.31}$$

Once again, we solve this in Fourier transform. From Eq. (2.15) and Eq. (2.19) we have

$$\begin{cases} \tilde{c}_{Lk}(\omega) = i\,\frac{\tilde{c}_{Lk}(t=0) - it_L \tilde{d}(\omega)}{\omega - \Delta_{Lk} + i\eta} \\ \tilde{d}(\omega) = -i\chi(\omega) \sum_\alpha e^{i\phi_\alpha} \sqrt{\frac{\Gamma_\alpha}{\pi\ \rho_\alpha}}\; \tilde{c}_{\alpha,\mathrm{in}}(\omega) \end{cases} \quad . \tag{2.32}$$

Putting it all together, we obtain that the electric current through the system (here we put $\Gamma_L = \Gamma_R$).

$$I = \int_{-\infty}^{+\infty} \frac{d\omega}{2\pi} \frac{f_L - f_R}{1 + \left[(\omega - \epsilon_d)/\Gamma\right]^2} \equiv \int_{-\infty}^{+\infty} \frac{d\omega}{2\pi} (f_L - f_R)\tau(\omega)\,, \tag{2.33}$$

where the function $\tau(\omega)$ is defined as the transparency of the system.

2.4 The equation of motion for the oscillator

The knowledge of the electronic operators allows for a more insightful look at the evolution of the system. In particular, it is possible to relate the average number of electrons $\bar{n}(t)$ and its auto-correlation spectrum $S_{xx}(\omega)$ to the back-action force that the electronic subsystem exerts on the mechanical oscillator.

In this section, we derive an equation of motion of the Langevin form for the mechanical oscillator following the derivation of reference [25].

2.4.1 Derivation of the Langevin Equation

Starting from the Anderson-Holstein Hamiltonian in Eq. 2.12, Hamilton's equations of motion can be used to derive

$$m\ddot{\hat{x}} = -m\omega_0^2\hat{x} - F_0\hat{n}\,, \tag{2.34}$$

The interesting part of this equation lies on the interplay between $\hat{n}$ and $\hat{x}$: The first one determines the latter, that in turn changes the value of the first. The goal of the rest of this section is to find the effects of this back-action.

First of all we take the average over a period t_{avg} so that $\Gamma^{-1} \ll t_{\text{avg}} \ll \omega_0^{-1}$: (1). The fluctuations around the average value are negligible for $\hat{x}$ because the oscillator moves too slowly. We thus write $x(t)$ instead of $\langle x(t)\rangle_\tau$ in order for the notation to stay readable. (2). For the opposite reason, fluctuations are not negligible for $\hat{n}$. As we will see, $\langle \hat{n}\rangle_\tau = n(x,t)$ on this short time period differs from $\bar{n}(x)$ as calculated in Eq. (2.29). We also define the fluctuations of the force $\xi(x,t) = -F_0\left[n(x,t) - \langle n(x,t)\rangle_\tau\right]$. This leads us to

$$m\ddot{x}(t) = -m\omega_0^2 x(t) - F_0 n(x,t) + \xi(x,t)\,. \tag{2.35}$$

We thus have two quantities to calculate: The average value of the force $-F_0 n(x,t)$, from which we will derive $F_e(x)$ and the electron-induced dissipation coefficient $A(x)$, and its fluctuations $\xi(x,t)$, which will lead to the electron-induced diffusion coefficient $D(x)$.

The Average Value of the Force

The task to compute $n(x,t)$ for the full system is not an easy one. Differently from the result at fixed position of the nanotube, there is here a back-action that the motion of the nanotube exerts on the electronic system. This means that the variable x depends on time, so that we would have to write $n(x(t),t)$.

The new value of $n(x,t)$ can be derived at first order in the interaction Hamiltonian H_i using the Kubo formalism. It says:

$$n(t) = \bar{n} + i\int_{-\infty}^{+\infty} dt'\theta(t-t')\left\langle [n(t), H_i(t')]\right\rangle_0\,, \tag{2.36}$$

where $\bar{n}$ is the average value of n on the unperturbed system (see Eq. (2.29)), the subscript 0 means that we are taking the average on the unperturbed system, and we removed the x dependence to shorten the notation.

Let us remind that $H_i = -F_0\; x(t)\cdot n(t)$. Since $n(t)$ and $x(t)$ act on different Hilbert spaces, they commute and their average value can be separated. This leads us to say:

$$\begin{aligned}
\langle n(t)\rangle &= \bar{n} - iF_0\int_{-\infty}^{+\infty} dt'\theta(t-t')\left\langle [n(t), x(t')n(t')]\right\rangle_0\,,\\
&= \bar{n} - iF_0\int_{-\infty}^{+\infty} dt'\theta(t-t')\left\langle [n(t-t'), n(0)]\right\rangle_0 \langle x(t')\rangle_0\,,\\
&= \bar{n} + F_0\gamma(t) * \langle x(t)\rangle_0\,,
\end{aligned} \tag{2.37}$$

where

$$\gamma(t) \equiv i\theta(t)\ S_-(t)\,,$$
$$S_-(t) \equiv \langle [n(t), n(0)] \rangle_0 = S_{nn}(t) - S_{nn}(-t)\,,$$

and $S_{nn}(t)$ was defined in Eq. 2.30.

The effect of $\bar{n}$ is to add a space- but not time-depending force to the system. It accounts completely for the force $F_e(x)$ that we defined at mean field level in Eq. (2.7):

$$F_e(x) = -F_0\bar{n}\,. \tag{2.38}$$

The other term will define the dissipation of the system $A(x)$. To calculate its value we go to the dual space of the frequency:

$$\langle n(t) \rangle_\omega = F_0\ \gamma(\omega)\ \ \langle x(t) \rangle_{0,\omega}\ , \tag{2.39}$$

where

$$\gamma(\omega) = i\frac{S_-(\omega)}{2} + \int_{-\infty}^{+\infty} \frac{d\omega'}{2\pi} \cdot \frac{S_-(\omega')}{\omega - \omega'}\,. \tag{2.40}$$

Let us write the average of the position on the unperturbed system as

$$\langle x(t) \rangle_{0,\omega} = \langle x(t) \rangle_\omega + \delta x(\omega) \equiv x(\omega) + \delta x(\omega) \tag{2.41}$$

Therefore, the right-hand side of Eq. (2.39) becomes $F_0\ \gamma(\omega)x(\omega) + F_0\ \gamma(\omega)\delta x(\omega)$. The second term is of order F_0^2, because $\delta x(\omega)$ is zero in absence of interaction; we can disregard it and keep only the first order term. This drastically simplifies the differential equation that we have to solve. It now becomes:

$$m(\omega_0^2 - F_0\bar{n} - \omega^2)\ x(\omega) = F_0^2\gamma(\omega)\ x(\omega) + \xi(\omega)\,. \tag{2.42}$$

We can define the role of $\gamma(\omega)$ by its position in the equation. Its real part renormalizes the spring constant. However, this term is much smaller than the main renormalization factor $F_0\bar{n}$ and can thus be neglected. Instead, the imaginary part of $\gamma(\omega)$ has the role of a dissipation, as one can see it by comparing to the Langevin equation of a damped linear oscillator $m(\omega_0^2 - \omega^2)\ x(\omega) = -i\omega A x(\omega)$. In particular, the dissipation coefficient $A(x)$ is given by

$$A(x) = -F_0^2\frac{\mathrm{Im}\gamma}{\omega} = -F_0^2\frac{S_-(\omega)}{2\omega}\,.$$

Now, $S_-(\omega) = S_{nn}(\omega) - S_{nn}(-\omega)$ has a typical frequency scale $\Gamma \gg \omega_0$. Since $x(\omega)$ is sharply peaked around ω_0, we can approximate

$$\frac{S_-(\omega)}{2\omega} \equiv \frac{S_{nn}(\omega) - S_{nn}(-\omega)}{2\omega} \approx \left.\frac{dS_{nn}(\omega)}{d\omega}\right|_{\omega=0}\,,$$

from which we finally derive

$$A(x) = -F_0^2\left.\frac{dS_{nn}(\omega)}{d\omega}\right|_{\omega=0}\,. \tag{2.43}$$

Force fluctuations

Force fluctuations average to zero by definition. In order to characterize them we need to calculate the auto-correlator of $\xi(t)$. We have:

$$\begin{aligned} \langle \xi(t)\xi(0)\rangle &= \langle F_0\left[n(t)-\bar{n}(t)\right]F_0\left[n(0)-\bar{n}(0)\right]\rangle \\ &= F_0^2\,\langle n(t)n(0)-\bar{n}(t)\bar{n}(0)\rangle \\ &= F_0^2 S_{nn}(t) \end{aligned} \tag{2.44}$$

Once again, we can exploit the adiabatic approximation $\omega_0 \ll \Gamma$: We apply the Fourier transform and take the value $\omega = 0$ as argument of $S_{nn}(\omega)$. We then obtain the dissipation coefficient

$$D(x) = F_0^2 S_{nn}(x, \omega = 0)\,. \tag{2.45}$$

Summary

To sum up, the Hamiltonian in Eq. 2.12 can be used to derive an equation of motion of the Langevin form, where the system is subject to a fluctuating force. The equation reads:

$$m\ddot{x} + A(x)\dot{x} + m\omega_0^2 x = F_e(x) + \xi(t)\,, \tag{2.46}$$

where the dissipation $A(x)$, the average force $F_e(x)$, and the stochastic force $\xi(t)$ are due to the electrons tunneling through the quantum dot [13, 16]. The stochastic force is more conveniently described with the parameter $D(x)$ that satisfies $\langle \xi(t)\xi(t')\rangle = D(x)\delta(t-t')$. The explicit expression for A, F_e, and D is:

$$\begin{cases} F_e(x) & = -F_0 n(x,T) \\ D(x) & = F_0^2 S_{nn}(x,T,\omega=0) \\ A(x) & = -F_0^2 \left.\frac{dS_{nn}(x,T,\omega)}{d\omega}\right|_{\omega=0} \end{cases}\,, \tag{2.47}$$

where $n(x,T) = \langle n(t)\rangle = \left\langle d^\dagger(t)d(t)\right\rangle$ is the average number of electrons in the dot and $S_{nn}(x,T,\omega) = \langle n(t)n(0)\rangle_\omega$ is the Fourier transform of the autocorrelator of $n(t)$. The result for $\Gamma_L = \Gamma_R$ is[13]:

$$\begin{cases} F_e(x) & = -F_0 \int_{-\infty}^{+\infty} \frac{d\omega}{2\pi\Gamma}\ (f_L + f_R)\,\tau \\ D(x) & = F_0^2 \sum_{\alpha,\beta} \int_{-\infty}^{+\infty} \frac{d\omega_1}{2\pi\Gamma^2} f_\alpha (1-f_\beta)\tau^2 \\ A(x) & = -F_0^2 \sum_{\alpha,\beta} \int_{-\infty}^{+\infty} \frac{d\omega_1}{2\pi\Gamma^2} f_\alpha \tau \left[f'_\beta \tau - (1-f_\beta)\tau'\right]\,, \end{cases} \tag{2.48}$$

where τ is the transmittivity function $\tau(\omega) = [1 + (\omega - \varepsilon_0)^2/\Gamma^2]^{-1}$.

2.5 Considering the fluctuations: The Fokker-Planck equation and its stationary solution

The Langevin equation in Eq. (2.46) is not easy to solve because of the fluctuating term $\xi(\omega)$, whose effect on the physical properties of the system can be dramatic. Therefore, starting from the Langevin equation of motion, we derive a Fokker-Planck equation for the probability distribution of the system on the x–p phase space $P(x,p,t)$. It reads:

$$\partial_t P = \mathcal{L}_0 P \equiv \frac{p}{m}\partial_x P - F\partial_p P + \frac{A}{m}\partial_p(pP) + \frac{D}{2}\partial_p^2 P\,. \tag{2.49}$$

Depending on the situation, we will use one or the other equation, since they are absolutely equivalent. In particular, all numerical routines are done solving the Fokker-Planck equation.

Following Refs. [16, 17], the solution of $\partial_t P = 0$ is

$$P_{\text{st}}(x,p) = \frac{1}{\mathcal{N}} e^{-E(x,p)/T_{\text{eff}}}, \qquad T_{\text{eff}} = \frac{D(x)}{2A(x)} = \text{const.} \tag{2.50}$$

where $\mathcal{N} = \iint dx\, dp\, \exp\left(-\frac{E(x,p)}{T_{\text{eff}}}\right)$ is a normalization factor. This can be proved by substitution inside Eq. (2.49), provided that the ratio of $D(x)$ over $A(x)$ is constant.

We can verify this condition by computing D and A given by Eq. (2.48). If the temperature and the voltage of the system are sufficiently low, meaning that $\Gamma \gg V, T$, we can expand the function $\tau(\omega, x)$ for small ω; the fast decay of the Fermi functions involved in the integral assures the expansion to always converge. One thus finds the following values for the diffusion and dissipation coefficients:

$$\begin{aligned} A(x) &= \frac{F_0^2}{\pi\Gamma^2}\tau_0^2(x)\left[1 + \frac{2\pi^2}{3}\left[5\tau_0(x) - 6\tau_0^2(x)\right]\left(\frac{T}{\Gamma}\right)^2\right], \\ D(x) &= A(x)\cdot T\left(1 + \frac{V}{2T}\coth\frac{V}{2T}\right), \end{aligned} \tag{2.51}$$

where $\tau_0(x) = \tau(\mu_0, x)$. The corrections are of order $(V/\Gamma)^2$ and they are negligible since, in all our numerical simulation, we use a value of $V = 0.005\Gamma$, unless otherwise specified.

The effective temperature of the system is then:

$$T_{\text{eff}} = \frac{D(x)}{2A(x)} = \frac{T}{2}\left(1 + \frac{V}{2T}\coth\frac{V}{2T}\right)\,. \tag{2.52}$$

Notice that we find an effective temperature $T_{\text{eff}} = V/4 > 0$ even when the physical temperature of the system T is zero.

2.5.1 The probability density function in the energy space

If the dissipation and fluctuation of the system are small, the energy is a quasi-constant of motion: The system performs many orbits on a trajectory of a given energy before drifting to lower energies (dissipation) or being randomly kicked to a different orbit (fluctuation). It is then interesting to find the probability distribution for the system in the phase space (E, t_E), where every point is determined by the energy E that defines the trajectory containing the point and the time t_E spent on the trajectory to reach the point. Their definitions are:

$$E(x,p) = U(x) + \frac{p^2}{2m}, \qquad t_E(x,p) = \int_0^x \frac{dx_1}{v(x_1, E(x,p))}, \tag{2.53}$$

where $v(x_1, E(x,p)) = \sqrt{2/m}\sqrt{E(x,p) - U(x_1)}$ is the velocity of the point on the trajectory and $U(x) = kx^2/2 + U_e(x)$ is the total potential energy of the system.

The variable change is given by

$$dE\, dt_E = |J|\, dx\, dp, \qquad |J| = \begin{vmatrix} \partial_x E & \partial_p E \\ \partial_x t_E & \partial_p t_E \end{vmatrix} = 1 \tag{2.54}$$

The probability distribution as a function of E and t_E becomes thus

$$P_{\rm st}(E, t_E) = P_{\rm st}(x(E,t_E), p(E,t_E))\,|J| = \frac{1}{\mathcal{Z}} \exp\left(-\frac{E}{T_{\rm eff}}\right), \tag{2.55}$$

or, integrating over a single trajectory

$$P_{\rm st}(E) = \frac{1}{\mathcal{Z}} T_E \exp\left(-\frac{E}{T_{\rm eff}}\right), \tag{2.56}$$

2.5.2 An analysis of the probability density function in different regimes

Eq. (2.50) is a general solution valid for all values of electromechanical coupling, provided a bias voltage $V \ll \Gamma$ is applied. It tells us that the probability distribution is strictly connected to the potential energy of the system, i.e., that it is a Gibbs probability distribution. Now, we know the general expression of the potential energy (see Eq. (3.8)): It simplifies for very small couplings, where we can consider just the quadratic term, but also at the transition, where the quadratic term is exactly zero and the behavior of the system is determined by the quartic term.

In the weak coupling regime $\varepsilon_P \ll \Gamma$, the potential can be approximated by $U(x) \approx \frac{\Gamma}{2\pi}\frac{\pi\Gamma}{\varepsilon_P}\left(1 - \frac{\varepsilon_P}{\pi\Gamma}\right) y^2$ (see Eq. (3.9)). The probability distribution becomes thus Gaussian, with a width governed by the effective temperature of the system $T_{\rm eff}$.

At the transition, $\varepsilon_P = \pi\Gamma$, the approximation to the potential gives $U(x) \approx \frac{\Gamma}{12\pi} y^4$. The probability distribution has thus a wider shape, decaying with $\exp(-x^4)$, since the potential is much flatter.

We can also give some qualitative understanding far above the transition. There, the potential has a double well shape coming from the second-order term having a negative sign and the fourth-order term having a positive sign. If the potential barrier between the wells is high enough, the system lives in either of the two and jumps to the other one on a very long time scale due to stochastic fluctuations. The probability distribution will then be given by two almost-separate parts, one pertaining to the left well and one to the right well. Expanding around each minimum, the second order term is positive and might dominate over the others. (This happens when the typical energy of the fluctuations V is much lower than the height of the potential barrier.) In that case, the probability distribution is the sum of the gaussian distribution, each of them around one minimum.

These three cases have been studied numerically and the resulting probability distributions and potentials have been plotted in Figure 2.3.

2.5.3 A fluctuation-dissipation relation

The fluctuation-dissipation theorem links the behavior of the system under a very small external force to the behavior of the system at equilibrium. The first one is modeled by the linear response function $\chi(\omega)$, defined by $x(\omega) = \chi(\omega)F(\omega)$, and the second one by the autocorrelation of the position $S_{xx}(\omega) = \langle x(t)x(0)\rangle_\omega$.

Since the theorem is only valid at equilibrium, we are not sure whether this relation holds in the present case. We will verify the conditions that the system must fulfill to make it hold.

The linear response function $\chi(\omega)$

We can find the linear response of the system by letting $F(x) \to F(x) + F_D \cos(\omega_D t)$ in Eq. (2.49). The evolution operator becomes $\mathcal{L}(t) = \mathcal{L}_0 + 2\mathcal{L}_D \cos(\omega_D t)$, with $\mathcal{L}_D = -F_D \partial_p/2$. After a transient time the solution can be written as a Fourier series

$$P(t) = \sum_n e^{in\omega_D t} P_n\,, \qquad P_n = \sum_{k=0}^{\infty} P_{n,k}\,, \tag{2.57}$$

where each Fourier component P_n has been expanded as a power series of the driving parameter F_D, with $P_{n,k}$ of order F_D^k. This, coupled with the Fokker-Planck equation $\partial_t P(t) = \mathcal{L}(t)P(t)$, leads to the set of equations:

$$\begin{aligned} (in\omega_D - \mathcal{L}_0)P_{n,0} &= 0 \\ (in\omega_D - \mathcal{L}_0)P_{n,k+1} &= \mathcal{L}_D(P_{n+1,k} + P_{n-1,k}), \end{aligned} \tag{2.58}$$

with the condition $\mathrm{Tr}P(t) = 1$. Eq. (2.58) can be solved by recursion. The time dependence of the displacement then reads

$$\tilde{x}(t) \equiv \mathrm{Tr}\left[\hat{\tilde{x}} P(t)\right] \approx F_D \chi(\omega_D) e^{i\omega_D t} + \text{c.c.}\,, \tag{2.59}$$

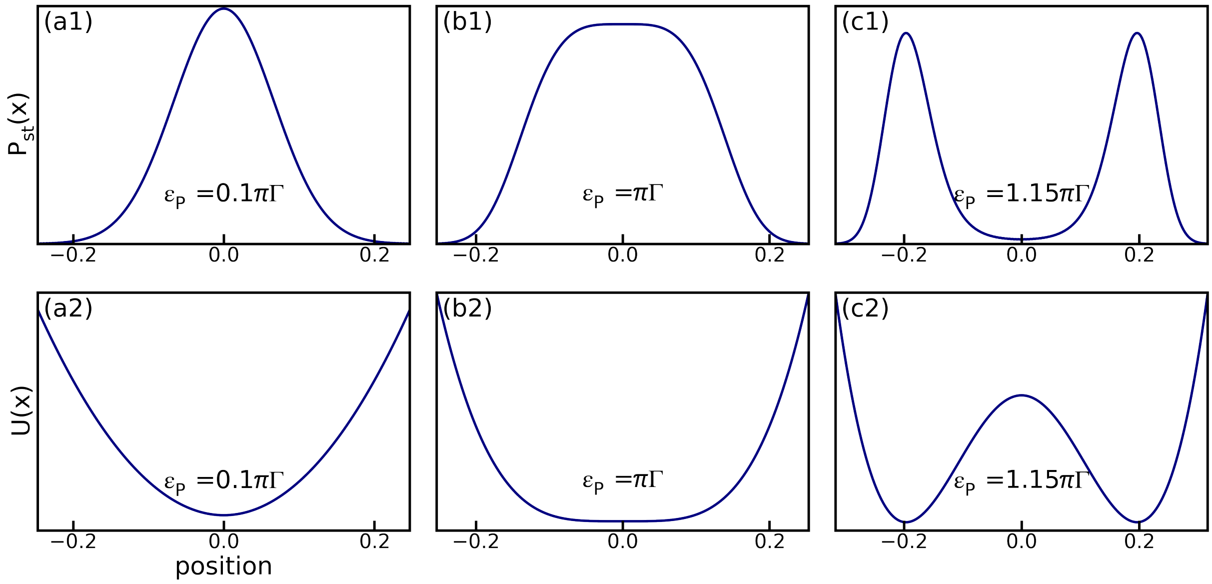

Figure 2.3: The probability distributions – panels (a1), (b1), and (c1) – and the potentials – panels (a2), (b2), and (c2) – for weak coupling, at the transition, and in the bistable state.

where

$$\chi(\omega) = \mathrm{Tr}\left[\frac{\hat{\tilde{x}}}{F_D} P_1(t)\right]_\omega = \mathrm{Tr}\left[\hat{\tilde{x}}(i\omega - \mathcal{L}_0)^{-1}\partial_p P_{\mathrm{st}}\right] . \tag{2.60}$$

The autocorrelation function $S_{xx}(\omega)$

It is defined by $S_{xx}(\omega) = \langle x(t)x(0)\rangle_\omega$. We can compute it numerically following ref. [17]:

$$S_{xx}(\omega) = -2\mathrm{Tr}\left[\hat{\tilde{x}}\frac{\mathcal{L}_0}{\omega^2 + \mathcal{L}_0^2}\hat{\tilde{x}} P_{\mathrm{st}}\right] , \tag{2.61}$$

where $\hat{\tilde{x}}$ is the operator that at each point in the x-p phase space associates its value $x - \langle x\rangle$, $\mathcal{L}_0$ is the Fokker-Planck matrix that comes from writing Eq. (2.49) as $\partial_t P = \mathcal{L}_0 P$, and P_{st} is the steady-state solution given in Eq. (2.50).

Their relation

Looking at the similarities between Eq. (2.60) and Eq. (2.61), the relation between $\chi(\omega)$ and $S_{xx}(\omega)$ comes naturally into question.

If P_{st} has a Gibbs form, such as the one we have found in Eq. (2.50), then $F_D \mathcal{L}_0 \hat{\tilde{x}} P_{\mathrm{st}} = -2T_{\mathrm{eff}} \mathcal{L}_D P_{\mathrm{st}}$. A little algebra then leads to a fluctuation-dissipation relation:

$$\mathrm{Im}\left[\chi(\omega)\right] = \frac{\omega}{2T_{\mathrm{eff}}} S_{xx}(\omega) . \tag{2.62}$$

Thus, for $eV \ll \Gamma$, χ and S_{xx} give access to the same information in two independent ways. For larger voltages Eq. (2.60) always holds, while Eq. (2.62) will be violated.

Chapter 3

The results, or: What we did

The experiments have shown some peculiar behaviors of suspended carbon nanotubes. To explain them, in our work, we have analyzed many accessible physical quantities of the system under different regimes; these include the mechanical softening, the electric current, the autocorrelation function of the current and of the position (from which one can derive the frequency of the mechanical response of the system), the ring-down time, and the linear susceptibility. We obtained numerical and analytical predictions that offer a broader general view and, most importantly, shine a light on the behavior of the system at the transition to the current-blockade regime. As we have seen in the previous chapter, the transition happens at a particular value of the electromechanical coupling; at this critical value we foresee a completely nonlinear behavior of the mechanical resonator associated to a universal quality factor of the system, independent of the voltage, temperature, or current through the system.

A detailed explanation of the last paragraph is the main objective of this chapter. At first we focus on the behavior of the system in the ideal situation of symmetric gating, small bias voltage, zero temperature, no external dissipation, and coupling up to the transition; in the last part of the chapter we will also discuss about the behavior when these conditions are relaxed.

3.1 The mechanical softening of the system

The first and clearest effect of the electromechanical interaction is the softening of the mechanical mode. In this section we will derive this softening at the mean field level, that is, without considering the fluctuations of the system given by the finite temperature or by the bias voltage. This represents a first approximation to the evolution of the system and yields good results especially when the electromechanical coupling is small, because in that case the system is quasi-linear.

In this regime, we only consider the deterministic evolution given by the force $F(x) = -kx + F_0\bar{n}[x(t)]$. The latter has an integral expression (see Eq. (2.29)) whose solution is not trivial if the temperature is not zero; we then work first at zero temperature and will focus on the effects of a finite temperature in Sec. 3.1.5.

3.1.1 The force and the equilibrium positions

In this regime of zero temperature, the force is (we remember that $\mu_L = V/2$ and $\mu_R = -V/2$):

$$F(x) = -kx + \frac{F_0}{2} + \frac{F_0}{2\pi} \sum_{\alpha=L,R} \arctan \frac{\mu_\alpha - \varepsilon_0 + F_0 x}{\Gamma} . \tag{3.1}$$

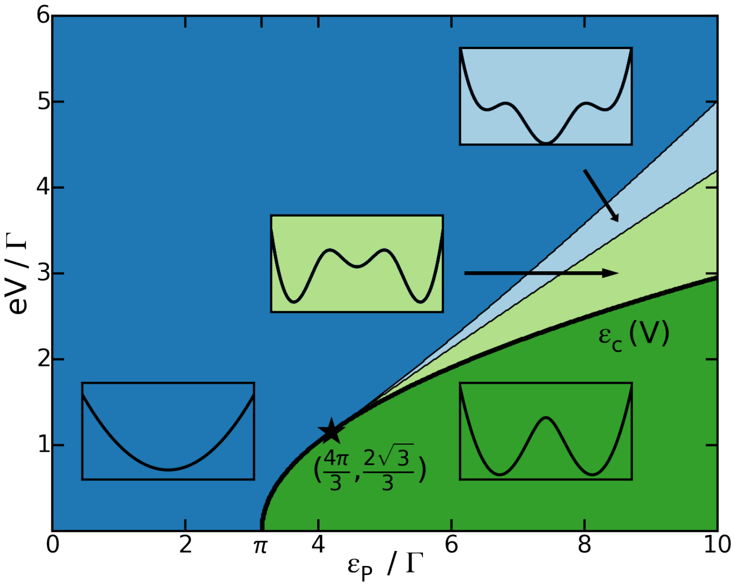

Figure 3.1: Full phase-diagram for the stability of the effective potential in the $eV - \varepsilon_P$ plane. A symmetric gating $\varepsilon_0 = \varepsilon_P/2$ and a zero temperature $T = 0$ K are chosen. The thick line indicates the critical line ε_c. Adapted from [15].

An equilibrium position is defined as the solution of the equation $F(x) = 0$. By inspection one can verify that $x_0 = F_0/2k$ is an equilibrium position if the electronic level takes the value $\varepsilon_0 = F_0^2/2k \equiv \varepsilon_P/2$. We call this *symmetric gating* because the occupied and unoccupied energy levels available to the electrons are symmetrical with respect to the zero in energy (see Figure 2.2). In other words, it represents the new electron-hole symmetry point of the system.

We devote the rest of this subsection to the study of the system under symmetric gating, while the effects of an asymmetric gating are explored in Sec. 3.1.4.

The equilibrium position in x_0 is not always a stable one. Its nature is influenced by the sign of the coefficient of the smaller term in the expansion of the potential around x_0. To find when this condition is satisfied, we express the force in terms of the dimensionless variable $y = F_0(x - x_0)/\Gamma$, for which one can write a Taylor expansion in y:

$$F(y) = F_0 \sum_{n=0}^{\infty} a_{2n+1} y^{2n+1}, \tag{3.2}$$

with

$$a_n = \frac{1}{\pi n!} \arctan^{(n)} \left(\frac{V/2}{\Gamma} \right) - \frac{\Gamma}{\varepsilon_P} \delta_{n,1}. \tag{3.3}$$

From here, the effective potential follows immediately:

$$U(x) = -\int^x F(x')dx' = -\Gamma \sum_{n=0}^{\infty} \frac{a_{2n+1}}{2n+1} y^{2n+2} . \tag{3.4}$$

Therefore, the minimum in $y = 0$ is stable if $a_1 < 0$. This determines the region $\varepsilon_P < \varepsilon_c(V)$, where the critical value $\varepsilon_c(V)$ is defined as

$$\varepsilon_c(V) = \pi\Gamma \left(1 + \frac{V^2}{4\Gamma^2} \right) . \tag{3.5}$$

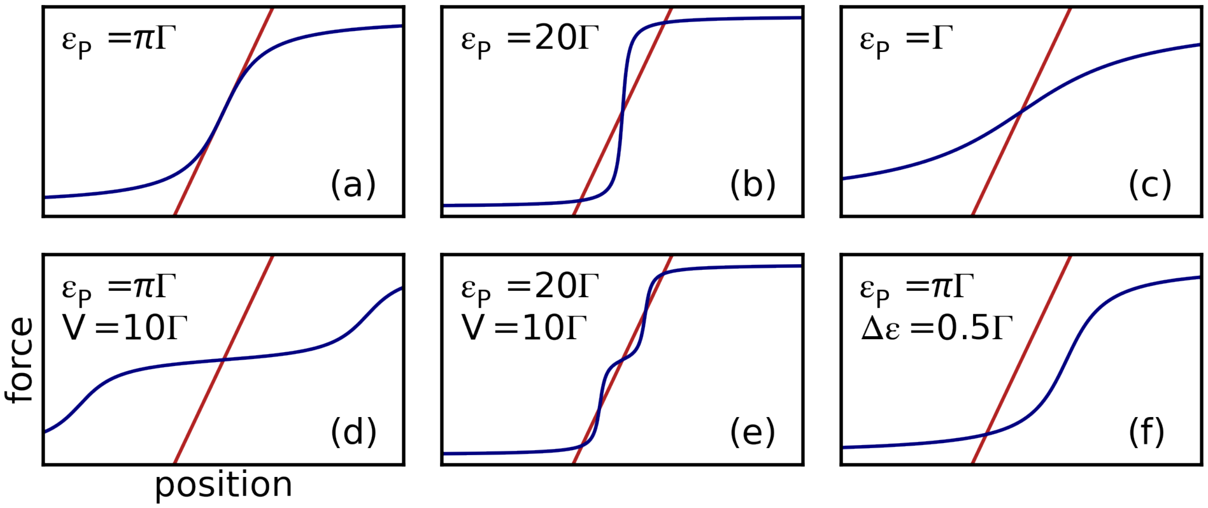

Figure 3.2: Graphical solution of Eq. (3.1) with elastic force in red and electronic force in blue. Every contact point defines an equilibrium position. Panel (a) shows the situation at the transition, while the other five show the effects of changing electromechanical coupling, bias voltage, and gating. Parameters that are not specified are set to zero. Panel (b) and (e) show respectively a situation with three solutions and one with five. Panel (f) shows that the solution in $x = x_0$ is not valid anymore when the gating is asymmetric ($\Delta\varepsilon = \varepsilon_0 - \varepsilon_P/2$).

The graphical solution of the equation $F(y) = 0$ confirms that there is always one solution at $y = 0$, provided the gating is symmetric (see Figure 3.2). However, it also shows that situations with three or five solutions might occur.

Since the function is regular, the stationary points correspond to alternating maxima and minima of the potential. Also, the system is bounded and symmetric, so the most external solution on each side is always stable. This proves that in the region of the phase diagram $\varepsilon_P > \varepsilon_c(V)$ the potential has two symmetric minima (see Figure 3.1). Also, it proves that three solutions imply a maximum in $y = 0$, while one or five solutions a minimum.

The situation is more complex when the origin is stable ($a_1 < 0$), because the total number of solutions is defined by the next coefficients in the Taylor series. When $a_3 < 0$, only one solution is allowed, while for larger values we can still have one or five solutions. By direct calculation one finds that $a_3 < 0$ for $V < 2\Gamma/\sqrt{3}$. For this voltage, the critical coupling is $\varepsilon_c(2\Gamma/\sqrt{3}) = 4\pi\Gamma/3$. Therefore, the point ($\varepsilon_P = 4\pi\Gamma/3$, $V = 2\Gamma/\sqrt{3}$) marks the beginning of the multi-stability along the critical line. The full behavior obtained by numerical solution of $F(y) = 0$ is shown in Fig. 3.1.

3.1.2 The mechanical resonance frequency

Starting from the expression of the force, we can define a *mean-field frequency* ω_m that describes the frequency of oscillation around the stable equilibrium position. It is defined as

$$\omega_m^2 = -\frac{1}{m}\left.\frac{dF}{dx}\right|_{x_{\min}}, \qquad (3.6)$$

by analogy with the definition of the resonance frequency of a harmonic oscillator. It takes the value

$$\begin{cases} \omega_m^2 = \omega_0^2 \left(1 - \frac{\varepsilon_P}{\varepsilon_c}\right) & \text{for } \varepsilon_P \leq \varepsilon_c, \\ \omega_m^2 \approx 2\omega_0^2 \left(\frac{\varepsilon_P}{\varepsilon_c} - 1\right) & \text{for } \varepsilon_P \gtrsim \varepsilon_c, \end{cases} \tag{3.7}$$

where we we recover the expected result $\omega_m = \omega_0$ when the coupling is weak.

Eq. (3.6) explains the softening of the oscillator that has been measured in several experiments. However, we remark that this quantity ω_m is defined only by the behavior of potential of the system in its minimum; ω_m does not take into account the fluctuations in the position that explore the potential energy outside of its minimum. It is however a good approximation of the real resonance frequency of the system in quasi-linear, weak-fluctuations regimes.

Interestingly, at $\varepsilon_P = \varepsilon_c$, this mean-field resonance frequency ω_m goes to zero. The corrections due to fluctuations will then be the dominant term.

3.1.3 The potential of the system

At zero temperature, vanishing bias voltage, and symmetric gating, the full analytical expression of the potential energy reads

$$U(y) = \frac{\Gamma}{2\pi} \left[\frac{\pi\Gamma}{\varepsilon_P} y^2 - 2y \arctan y + \log\left(1 + y^2\right) \right], \tag{3.8}$$

where again $y = F_0(x - x_0)/\Gamma$.

Expanding it around $y = 0$, as we have done in Eq. (3.4), we have at the fourth order

$$U(y) \approx \frac{\Gamma}{2\pi} \frac{\pi\Gamma}{\varepsilon_P} \left[\left(1 - \frac{\varepsilon_P}{\pi\Gamma}\right) y^2 + \frac{1}{6} \frac{\varepsilon_P}{\pi\Gamma} y^4 \right]. \tag{3.9}$$

One can verify that, along the critical line $\varepsilon_P = \varepsilon_c(V)$, the second-order term of the potential vanishes and $U(x)$ can be approximated by a fourth-order potential.

3.1.4 Sweeping around the symmetric gating

One of the most spectacular and direct proof of the back-action of the electronic transport on the mechanical dynamics is the observation of a maximum in the softening of the mechanical mode as a function of the gate voltage in coincidence with the maximum of the conductance of the quantum dot [63, 64, 32].

As a result of the electromechanical coupling, the average electrostatic force acting on the nanotube is obtained as $F_e(x) = F_0 \bar{n}(\varepsilon_0 - F_0 x)$ where $\bar{n} = \langle d^\dagger d \rangle$ is the mean population of the dot. The mean population is quantized and follows the Coulomb diamonds' pattern, that is, it has sharp, well-separated steps at some values of the position of the dot's energy level, one of which is situated at the value $\varepsilon_0 = \varepsilon_P/2$ that indicates symmetric gating. Here, the variation of the force with the position is maximal; the spring constant of the mechanical oscillator varies by a quantity $\delta k = -dF_e/dx|_{x=0} = F_0^2 \partial n_d / \partial\varepsilon_0|_{\varepsilon_P/2}$ and,

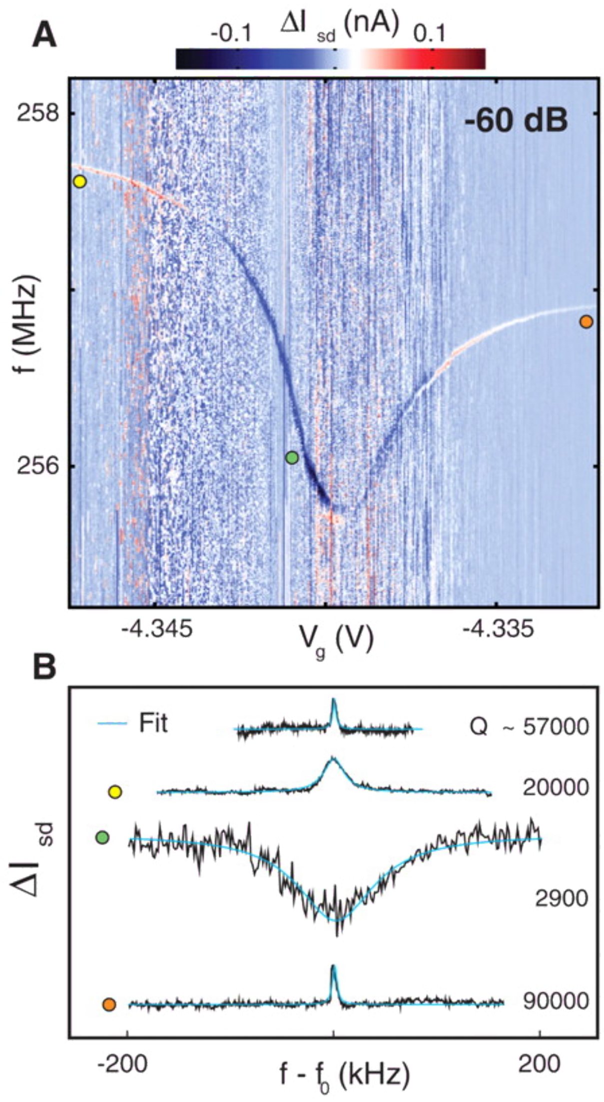

Figure 3.3: Experimental results for a suspended carbon nanotube driven with a radio-frequency (RF) excitation. The temperature is of the order of 100 mK, while Γ, as obtained from the maximum current passing through the junction, appears to be approximately 10 GHz ≈ 400 mK, which puts the system close to the coherent regime that we study. However, the bias voltage is 1.5 mV ≈ 300 GHz; the system is not in the regime of vanishing bias voltage. Panel **A**: Detector current (ΔI) versus frequency and gate-voltage at RF excitation power of 60 dB, as the gate voltage is swept through one Coulomb peak. The softening is represented by the vertical dip: The width we can infer from the graph is around 3 mV. The global descending behavior is due to the increasing tension in the nanotube as the gate voltage is increased.
Panel **B**: Fits of the resonance to a squared Lorentzian line shape at different gate voltages. Traces are taken at the positions indicated by colored circles (aside from the top trace, which is taken at Vg = 4.35 V). Adapted from [64].

consequently, the mechanical mode experiences a softening

$$\frac{\delta\omega_0}{\omega_0} = \frac{\varepsilon_P}{2}\left.\frac{\partial n_d}{\partial\varepsilon_0}\right|_{\varepsilon_P/2} . \tag{3.10}$$

This happens because, changing the position of the energetic levels of the dot around the symmetric gating point, one can enter or exit the resonance window, that is, one can set the quantum dot's electronic level to an energy for which tunnelling is forbidden by Pauli principle (see Figure 2.2). This effectively decouples the electronic and the mechanical part by preventing the electric current to flow, changing the equilibrium position x_0 and, indirectly, the new mechanical resonance value ω_m. Therefore, the maximum of the interaction is obtained for the symmetric value of the gate voltage $\varepsilon_0 = \varepsilon_P/2$ that we already discussed.

In this section we will show that the shape of the variation of the resonance frequency around the symmetric gating point heavily depends on the magnitude of the electromechanical coupling. In particular, around the critical value ε_c, we find a sharp peak, different from the Lorentzian shape that one expects at weak electro-mechanical coupling[63, 32]. We are going to study the effects of an asymmetry in the energetic levels both at weak and strong electromechanical coupling.

To take advantage of the gate symmetry we define $\varepsilon_0 = \varepsilon_P/2 + \Delta\varepsilon_0$. This allows us to rewrite the force as:

$$F = -F_0 \frac{\Gamma}{\varepsilon_P} \left\{ \frac{F_0 x + \varepsilon_P/2}{\Gamma} - \frac{\varepsilon_P}{\pi\Gamma} \arctan \frac{F_0 x + \varepsilon_P/2 + \Delta\varepsilon_0}{\Gamma} \right\} . \tag{3.11}$$

The equilibrium point x_0 can be found by solving $F(x_0) = 0$. This reduces to

$$\eta = \frac{\varepsilon_P}{\pi\Gamma} \arctan(\eta + \tilde{\varepsilon}), \tag{3.12}$$

where $\eta = [(F_0 x + \varepsilon_P/2)\Gamma]$ and $\tilde{\varepsilon} = \Delta\varepsilon_0/\Gamma$. The softening of the system as defined in Eq. (3.6) follows immediately:

$$\frac{\omega_m^2}{\omega_0^2} = 1 - \tau(\eta + \tilde{\varepsilon}) \frac{\varepsilon_P}{\varepsilon_c} , \qquad \tau(x) = \frac{1}{1 + x^2} \tag{3.13}$$

where $\tau(x)$ a function that is equivalent to the transparency of the junction. This will be verified when discussing the electric current.

In the next paragraphs, we compute η and ω_m in three different regimes.

Weak coupling $\varepsilon_P \ll \pi\Gamma$

Eq. 3.12 can be resolved recursively:

$$\eta = \frac{\varepsilon_P}{\pi\Gamma} \arctan[\frac{\varepsilon_P}{\pi\Gamma} \arctan(\eta + \tilde{\varepsilon}) + \tilde{\varepsilon}], \tag{3.14}$$

When the electromechanical coupling is but a small perturbation, at first approximation one has $\eta \approx 0$. Substituting it in the right hand side of the previous equation one finally obtains

$$\eta \approx \frac{\varepsilon_P}{\pi\Gamma} \arctan[\frac{\varepsilon_P}{\pi\Gamma} \arctan(\tilde{\varepsilon}) + \tilde{\varepsilon}], \tag{3.15}$$

which has the correct small and large $\tilde{\varepsilon}$ behavior. A variation in the gate voltage has thus little effect on the equilibrium position of the oscillator, because the electrons interact very weakly with the nanotube.

This leads to the softening (see Eq. (3.6))

$$\omega_m^2 \approx \left[1 - \frac{\varepsilon_P}{\pi\Gamma} \frac{\Gamma^2}{\Gamma^2 + \Delta\varepsilon_0^2} \right] \omega_0^2 , \tag{3.16}$$

which is qualitatively compatible with the experimental results in Figure 3.3.

Critical coupling $\varepsilon_P = \pi\Gamma$

When the electromechanical coupling is critical $\varepsilon_P = \pi\Gamma$, the third-order term of the force becomes important. The equilibrium position is found to be at $F_0 x_0 \approx \varepsilon_P/2 - \sqrt[3]{3\Delta\varepsilon_0\Gamma}$. This strong dependence on $\Delta\varepsilon_0$ is understandable thinking that x is a measure of the displacement of the nanotube due to the number of excess electrons, that can take all values between 0 and 1: When there is no excess electron on the nanotube, the electron-induced displacement is $x = 0$. On the other hand, an entire excess electron causes a displacement ε_P/F_0. A change in the gate voltage breaks the symmetry between the two possible occupation states, making one of the two more probable.

Regarding the softening of the system, we obtain

$$\omega_m = \sqrt[3]{3\frac{|\Delta\epsilon_0|}{\Gamma}}\,\omega_0 \text{ for } \varepsilon_P = \varepsilon_c\,. \tag{3.17}$$

We conclude that also the softening depends very sharply on the gate voltage. It is maximum at the symmetric gating and decreases with a cusp singularity.

The potential energy is also modified. Instead of Eq. (3.9) we find

$$U(y) \approx \frac{\Gamma}{2\pi}\frac{\varepsilon_c}{\varepsilon_P}\left[\left(1-\tau\frac{\varepsilon_P}{\varepsilon_c}\right)y^2 - \mathrm{sgn}(\Delta\varepsilon_0)\frac{2\varepsilon_P}{3\varepsilon_c}\sqrt{\tau^3(1-\tau)}y^3 + \frac{\varepsilon_P}{6\varepsilon_c}\tau^2(4-3\tau)y^4\right]. \tag{3.18}$$

Looking at the previous equation, we can see that the asymmetry modifies two things: It changes the transparency of the system at the equilibrium point in the monostable regime from 1 to τ and it introduces a third-order term in the potential of the system.

Bistable regime $\varepsilon_P > \pi\Gamma$

Finally, for $\varepsilon_P > \pi\Gamma$ and $\tilde{\varepsilon} = 0$ there are two (stable) solutions of Eq. 3.11, $F_0 x_0(\tilde{\varepsilon} = 0) = \varepsilon_P/2 \pm z_0$, with $z_0 > 0$. For small value of $\tilde{\varepsilon} > 0$ one finds:

$$F_0 x_0 = -z_0 + \frac{\varepsilon_c}{\varepsilon_P - \varepsilon_c}\frac{\tilde{\varepsilon}}{4}\,, \tag{3.19}$$

that is valid for $0 < \tilde{\varepsilon} \ll \left(\frac{\varepsilon_P - \varepsilon_c}{\varepsilon_c}\right)^{3/2}$.

For $\tilde{\varepsilon} < 0$ the stable solution is $-x_0$ $[x_0(\tilde{\varepsilon}) = -x_0(-\tilde{\varepsilon})]$, and sweeping $\tilde{\varepsilon}$ through 0 the system jumps from one solution to the other. We can thus simply concentrate on the positive values of $\tilde{\varepsilon}$.

The linear dependence of y_0 leads to a linear dependence of ω_m^2 close to $\tilde{\varepsilon} > 0$. For $0 < \varepsilon_P - \varepsilon_c \ll \varepsilon_c$ one finds:

$$\frac{\omega_m}{\omega_0} = \left(2\frac{\varepsilon_P - \varepsilon_c}{\varepsilon_c}\right)^{1/2} + \frac{\tilde{\varepsilon}}{2}\frac{\varepsilon_P}{\varepsilon_P - \varepsilon_c}\left(\frac{3\varepsilon_c}{2\varepsilon_P}\right)^{1/2}\,. \tag{3.20}$$

The slope diverges at $\varepsilon_P \to \varepsilon_c$, in agreement with the results at criticality that gives $\omega_m \tilde{\varepsilon}^{1/3}$. Since the curve is symmetric, the linear dependence leads to a cusp in the softening dependence on the gate voltage, which can be an indication of the bistability.

3.1.5 The effects of a finite temperature

A finite temperature T broadens the Fermi distribution of the leads $f_\alpha(\omega)$ on the energy scale $\omega \approx T$, inducing corrections to the average population of the dot $n(\varepsilon_0)$ on the scale $(T/\Gamma)^2$. In the coherent tunneling regime we are interested in, the temperature is much lower than the tunneling rate ($T \ll \Gamma$), so that these corrections can be computed using *Sommerfeld expansion*:

$$n(x,T) = n(x,0) - \frac{\pi}{6}\left(\frac{T}{\Gamma}\right)^2 \sum_{\alpha=L,R} \frac{\Gamma \cdot (\mu_\alpha - \varepsilon_0 + F_0 x)}{\left[\Gamma^2 + (\mu_\alpha - \varepsilon_0 + F_0 x)^2\right]^2}\,. \tag{3.21}$$

In the following, we will consider the case of vanishing bias voltage ($V \ll \Gamma$) and symmetric gating ($\Delta\varepsilon_0 = 0$). From Eq. (3.21) it is straightforward to derive the temperature-induced modification of the effective potential. At fourth order in the oscillator position $y = F(x - x_0)/\Gamma$:

$$U(y) \approx \frac{\Gamma}{2\pi}\frac{\pi\Gamma}{\varepsilon_P}\left\{1 - \frac{\varepsilon_P}{\pi\Gamma}\left[1 - \frac{\pi^2}{3}\left(\frac{T}{\Gamma}\right)^2\right]\right\} y^2 + \frac{\Gamma}{12\pi}\left[1 - 2\pi^2\left(\frac{T}{\Gamma}\right)^2\right] y^4 \,. \tag{3.22}$$

As a consequence, the temperature-dependent mechanical mode softening is written

$$\omega_m(T) \approx \omega_0 \sqrt{1 - \frac{\varepsilon_P}{\pi\Gamma}\left[1 - \frac{\pi^2}{3}\left(\frac{T}{\Gamma}\right)^2\right]} \,, \tag{3.23}$$

from which it follows that, at the mean-field level, the mechanical mode softening is preserved even a finite temperature $T/\Gamma \ll 1$, but with a renormalized value for the critical electromechanical coupling $\varepsilon_P = \varepsilon_c(T)$

$$\varepsilon_c(T) = \frac{\pi\Gamma}{1 - \frac{\pi^2}{3}\left(\frac{T}{\Gamma}\right)^2} \approx \pi\Gamma\left[1 + \frac{\pi^2}{3}\left(\frac{T}{\Gamma}\right)^2\right] \,. \tag{3.24}$$

Hence, when increasing the temperature, a larger electromechanical coupling is needed to achieve the current-blockade transition. This is consistent with the fact that a finite temperature smoothens the dependence of the dot population with ε_0 and thus decreases the softening of the mode (see Eq. (3.21)).

To conclude the discussion of Eq. (3.22), we remark that the effect of a finite temperature is not only to renormalize the critical coupling $\varepsilon_c(T)$ but also to reduce the quartic non-linearity of the oscillator. This effect will be crucial in the next section when investigating the behavior of the mechanical spectrum close to criticality.

The full analytical treatment of mean-field temperature with the digamma function

A more complete result can be obtained using the digamma function

$$\Psi(z) = \frac{d}{dz}\ln\left(\boldsymbol{\Gamma}[z]\right) = \frac{\boldsymbol{\Gamma}'[z]}{\boldsymbol{\Gamma}[z]} \,, \tag{3.25}$$

where $\Gamma(z)$ is the Euler gamma function. At finite temperature the population of the dot can be expressed as:

$$n = \frac{1}{2} + \frac{1}{2\pi}\mathrm{Im}\sum_{\alpha=L,R}\Psi\left(\frac{1}{2} + \frac{\Gamma + i(\mu_\alpha - \epsilon_0 + F_0 x)}{2\pi T}\right) \,. \tag{3.26}$$

We are interested in studying how the transition is modified by the temperature in the symmetric case $\epsilon_0 = \varepsilon_P/2$. At the transition, the equilibrium position in the symmetric point x_0 changes from stable to unstable. It is sufficient than to study when the derivative of the force changes sign to have the evolution of the critical value with the temperature.

For simplicity we focus on the $V = 0$ case. The critical value of the coupling constant for which $dF/dx|_{x_0} = 0$ reads then:

$$\varepsilon_c(T) = -\left(\frac{\partial n}{\partial \epsilon_0}\right)^{-1} = \frac{2\pi^2 T}{\Psi^{(1)}(1/2 + \Gamma/2\pi T)}\,, \tag{3.27}$$

with $\Psi^{(n)}(z) = d^n\Psi(z)/dz^n$ the n-derivative of the digamma function The digamma function has an interesting property for which[72]

$$\Psi^{(1)}(1/2) = \pi^2/2, \qquad \Psi(z) \approx 1/z + 1/(2z^2) + 1/(6z^3) + \ldots \qquad \text{for large } z. \tag{3.28}$$

Putting it inside Eq. (3.27) one finds the following asymptotic behaviors:

$$\varepsilon_c(T \gg \Gamma) = 4T\left[1 - \frac{\Psi^{(2)}(\frac{1}{2})}{\pi^3}\frac{\Gamma}{T}\right] \approx 4T\left(1 + 0.543\frac{\Gamma}{T}\right)\,, \tag{3.29}$$

$$\varepsilon_c(T \ll \Gamma) = \pi\Gamma\left(1 + \frac{\pi^2}{3}\frac{T^2}{\Gamma^2}\right) \approx \pi\Gamma\left(1 + 3.29\frac{T^2}{\Gamma^2}\right)\,, \tag{3.30}$$

where we can verify that the low temperature limit is the same that we found using Sommerfeld expansion.

Finally we take a look at the potential to study how the terms change with temperature. Using $\Psi(z) = d\log\mathbf{\Gamma}(z)/dz$, we can write:

$$U(y) = \frac{\Gamma^2}{2\varepsilon_P}y^2 + 2T\mathrm{Re}\log\mathbf{\Gamma}\left[\frac{1}{2} + \frac{\Gamma}{2\pi T}(1 + iy)\right]\,, \tag{3.31}$$

where we have used the dimensionless position y introduced above. (Attention! We use $\mathbf{\Gamma}[x]$ for the Euler gamma function and Γ for the energy constant; another way to tell them apart is the dimension analysis.) One can verify using the asymptotic behavior for large z of $\log\mathbf{\Gamma}[z] = z\log z - z - \log(z/2\pi)/2 + \ldots$ [72] that Eq. (3.31) reduces to Eq. (3.8) for $T \ll \Gamma$.

Expanding the potential in a power series $U(y) = \sum_{n=2}^{\infty} U_n y^n$, the generic n-term of the expansion reads:

$$U_n = \delta_{n,2}\frac{\Gamma^2}{\varepsilon_P} + \frac{\Gamma}{\pi n!}\Psi^{(n-1)}\left(\frac{1}{2} + \frac{\Gamma}{2\pi T}\right)\cdot\left(\frac{\Gamma}{2\pi T}\right)^{n-1}\,, \tag{3.32}$$

with U_n non vanishing only for even values of n.

This gives immediately that the quartic term U_4 is always positive and vanishes for large T as $1/T^4$. We can qualitatively understand this result thinking that expanding in the position is like expanding in the energetic level of the dot, since $\epsilon_d = \varepsilon_0 - F_0 x$; and the electromechanical coupling, responsible for all higher-order terms, depends linearly on the average occupation of the dot, which in turn is very weakly influenced by the position of the energetic level for large temperatures.

In the opposite limit $T \ll \Gamma$ one finds for the quartic term of the expansion the result contained in Eq. (3.22).

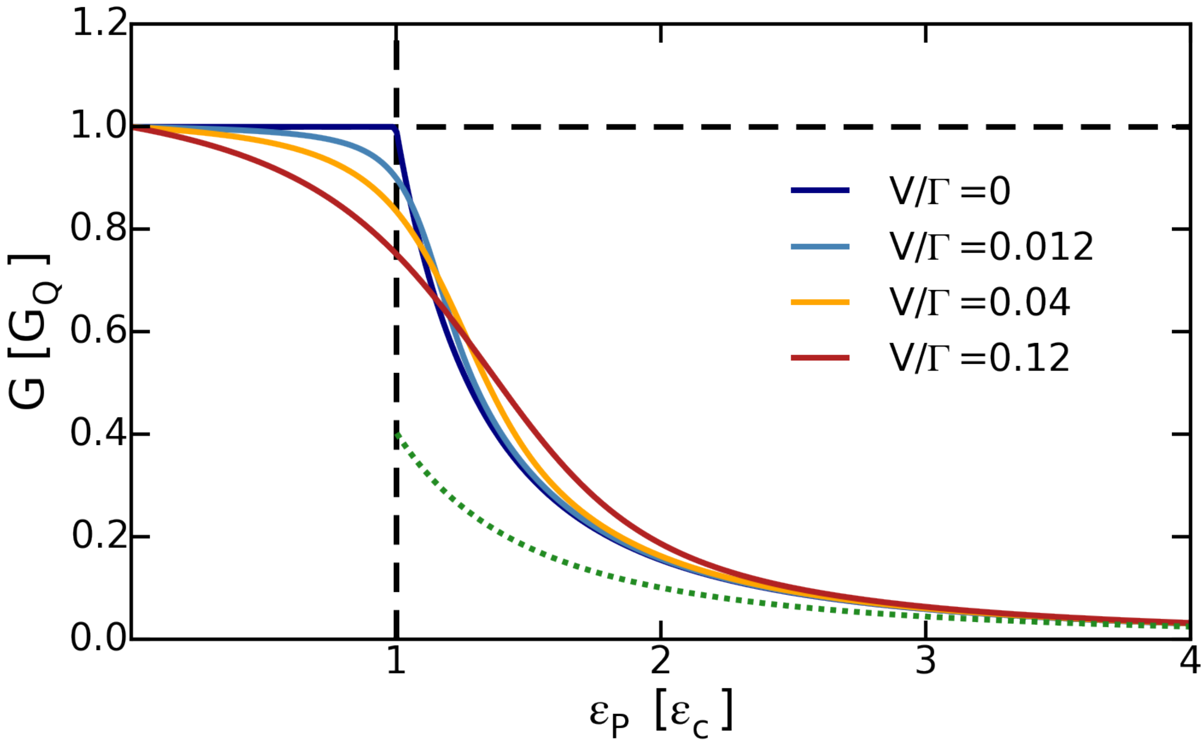

Figure 3.4: Mean conductance $\langle G(x)\rangle$ through a CNT quantum dot coupled to the mechanical oscillator as a function of the coupling $\varepsilon_P = F_0^2/k$. Curves obtained at $\Gamma = 1000\,\omega_0$, $T = 0\,\mathrm{K}$, symmetric gating, and various bias voltages. The black dashed lines are just a reference for the eye. The dotted green line is the asymptotic behavior in the bi-stable phase $\varepsilon_P \gg \varepsilon_c$. Adapted from [15].

3.2 The electric current

The total current through the system at a given position $I(x,t)$ can be seen as the difference between the current flowing from the left to the right and the current flowing in the opposite direction.

Thanks to the adiabatic approximation, the right-flowing current is given by the integral of the transparency over all available states for the process, which have one electron on the left side and one hole on the right side. Therefore one obtains $I_R(x,t) = G_Q \int_{-\infty}^{+\infty} d\omega f_L(1-f_R)\tau(x)$, where we use the definition of quantum of conductance $G_Q = e^2/h$ and we remember the definitions of the Fermi-Dirac distribution $f_\alpha(\omega) = \left[1 + e^{(\omega-\mu_\alpha)/T}\right]^{-1}$ and the transparency $\tau(\omega)$. We don't write explicitly the dependence on the integration variable contained in $f_L(\omega)$, $f_R(\omega)$, and $\tau(x,\omega)$ for sake of readability of the formulas.

Swapping the subscripts L and R we obtain the current flowing in the opposite sense. The total current becomes thus (see Eq. (2.33):

$$I(x) = G_Q \int_{-\infty}^{+\infty} d\omega (f_L - f_R)\tau(x) \approx G_Q V \tau_0(x)\,, \tag{3.33}$$

where the approximation holds for small bias voltage $V \ll \Gamma$ and at zero temperature and $\tau_0(x)$ is the transparency taken at the average energy value $\mu_0 = (\mu_L + \mu_R)/2 = 0$ (see Figure 2.2).

The value of the transparency is $\tau(\omega) = [1 + (\omega - \varepsilon_0)^2/\Gamma^2]^{-1}$.

$$\tau_0(x) = \frac{1}{1+\left(\frac{\varepsilon_0 - F_0 x}{\Gamma}\right)^2} \,. \tag{3.34}$$

In order to find the total current we need to average $I(x)$ over the probability distribution of the system given in Eq. (2.50):

$$\langle I(x)\rangle = G_Q V \frac{\displaystyle\int_{-\infty}^{+\infty} \exp\left[-\frac{U(y)}{T_{\text{eff}}}\right] \frac{dy}{1+y^2}}{\displaystyle\int_{-\infty}^{+\infty} \exp\left[-\frac{U(y)}{T_{\text{eff}}}\right] dy}, \tag{3.35}$$

where $U(y)$ is the potential of the system as a function of the quantity $y = F_0(x - x_0)/\Gamma$. As we can see plugging Eq. (3.8)] in Eq. (3.35), there are just two parameters: the reduced coupling ε_P/Γ and the reduced effective temperature T_{eff}/Γ.

The numerical results of Eq. (3.35) are shown in Figure 3.4. For the electro-mechanical coupling, there is a critical value $\varepsilon_P = \varepsilon_c$ at which the current through the system starts to grow smaller; however, this process take place on a long time scale $(\Gamma/\varepsilon_P)^2$; for this reason the transition towards the current blockade is not easy to study by looking at the current. As a final remark, the effective temperature smears out the transition.

The next section is devoted to a more in-depth analysis of the electric current in all regimes.

3.2.1 Analytic calculations of the electric current through the system

In order to explain analytically Figure 3.4, we push one step further the evaluation of Eq. (3.35). We first consider the mono-stable phase $\varepsilon_P \leq \varepsilon_c$. The equilibrium position of the oscillator is $x_0 = F_0/2k$ and the potential can be approximated to the fourth order by Eq. (3.9). Every subsequent order in the expansion of the potential is even in the power of y; estimating y^{2n} over the Gibbs distribution $P_{\text{st}}(x,p)$ given in Eq. (2.50) and calculated using the fourth-order potential in Eq. (3.9), we obtain $y^{2n} \propto (T_{\text{eff}}/\varepsilon_c)^{n/2}$.

In the same way, we expand in power series the mean transmission factor provided in Eq. (3.34): $\langle\tau(x)\rangle = \sum_{n=0}^{+\infty}(-1)^n \langle y^{2n}\rangle$. Therefore, computing the conductance is formally equivalent to finding the moments $\langle y^{2n}\rangle$ of the Gibbs distribution $P_{st}(x)$ with the effective Duffing-like potential given by Eq. (3.9).

It is remarkable that this problem admits an exact analytical solution valid in the whole mono-stable regime $\varepsilon_P \leq \varepsilon_c$:

$$\langle I(x)\rangle = G_Q V \sum_{n=0}^{+\infty} \left(-6\sqrt{\frac{\pi^2}{3}\frac{T_{\text{eff}}}{\varepsilon_c}}\right)^n \Xi_n\left[\alpha_c\right] \,, \tag{3.36}$$

$$\Xi_n\left[\alpha_c\right] = \frac{\sum_{p=0}^{+\infty} \frac{(-\alpha_c)^p}{p!} \mathbf{\Gamma}\left[\frac{1+2(n+p)}{4}\right]}{\sum_{p=0}^{+\infty} \frac{(-\alpha_c)^p}{p!} \mathbf{\Gamma}\left[\frac{1+2p}{4}\right]} \,, \qquad \alpha_c = \frac{\varepsilon_c - \varepsilon_P}{\varepsilon_P}\sqrt{\frac{3}{\pi^2}\frac{\varepsilon_c}{T_{\text{eff}}}} \,, \tag{3.37}$$

where we introduced the adimensional parameter α_c quantifying the departure from the critical point $\varepsilon_P = \varepsilon_c$ and where $\mathbf{\Gamma}\left[x\right]$ stands for the Euler Gamma function.

Weak-coupling regime

The analytical evaluation of Eq. (3.36) for weak coupling is difficult because the parameter α_c is large and the summations need many terms to converge. It is more convenient to calculate the integral in Eq. (3.35). That's because in the regime of weak electromechanical coupling $\varepsilon_P \ll \varepsilon_c$, the quartic part of the effective potential in Eq. (3.8) is a small perturbation; at first order, therefore, we neglect it and use the quadratic potential $U(y) \approx (\Gamma\varepsilon_c/2\pi\varepsilon_P)y^2$. The exponential $\exp[-U(y)/T_{\text{eff}}]$ becomes Gaussian with variance $\sigma^2 = \pi T_{\text{eff}}\varepsilon_P/\Gamma\varepsilon_c \ll 1$, which allows for the expansion of the term $1/(1+y^2)$ at the second order in small y.

Therefore, only two Gaussian integrals need to be calculated. In the end we obtain

$$\langle I(x)(t)\rangle \approx G_Q V(1-\sigma^2) = G_Q V\left(1 - \frac{\varepsilon_P}{\varepsilon_c}\frac{\pi T_{\text{eff}}}{\Gamma}\right) \tag{3.38}$$

We recover from Eq. (3.38) the main features of Figure 3.4 for $\varepsilon_P \ll \varepsilon_c$: The unit transmission at zero coupling and the departure from balistic conductance induced both by non-linearities of the potential and by finite effective temperature.

At criticality

Eq. (3.36) allows for an asymptotic evalution of the mean conductance around the critical value ($\varepsilon_P = \varepsilon_c$). We consider the low-temperature limit $T_{\text{eff}} \ll \varepsilon_c$, where the summation in Eq. (3.36) can be approximated by using just the first two terms. We then obtain

$$\langle I(x)\rangle = G_Q V\left\{1 - 6\sqrt{\frac{\pi^2}{3}\frac{T_{\text{eff}}}{\varepsilon_c}}\ \Xi_1[\alpha_c]\right\}. \tag{3.39}$$

Since α_c is proportional to $\frac{\varepsilon_c-\varepsilon_P}{\varepsilon_P}$, at criticality it vanishes. Developing around zero, we keep just the terms up to first order in p in the expansion of 3.39. We obtain

$$\begin{aligned}\langle I(x)\rangle &\approx G_Q V\left\{1 - \sqrt{12\pi^2\frac{T_{\text{eff}}}{\varepsilon_c}}\frac{\mathbf{\Gamma}\left[\frac{3}{4}\right]}{\mathbf{\Gamma}\left[\frac{1}{4}\right]} - 6\frac{\varepsilon_c-\varepsilon_P}{\varepsilon_c}\frac{\mathbf{\Gamma}\left[\frac{3}{4}\right]}{\mathbf{\Gamma}\left[\frac{1}{4}\right]}\left[\frac{\mathbf{\Gamma}\left[\frac{3}{4}\right]}{\mathbf{\Gamma}\left[\frac{1}{4}\right]} - \frac{\mathbf{\Gamma}\left[\frac{5}{4}\right]}{\mathbf{\Gamma}\left[\frac{3}{4}\right]}\right]\right\}, \\ &\approx G_Q V\left(1 - 3.68\sqrt{\frac{T_{\text{eff}}}{\varepsilon_c}} + 0.815\frac{\varepsilon_c-\varepsilon_P}{\varepsilon_c}\right). \end{aligned} \tag{3.40}$$

The first two terms correspond to the conductance of the device at criticality, while the last one quantifies the impact of departure from criticality. In contrast to the perturbative regime (see Eq. (3.38)) the conductance scales with $(T_{\text{eff}}/\varepsilon_c)^{1/2}$ and the (negative) slope is voltage-independent. However, this is only valid when the condition $\left(\frac{\varepsilon_c-\varepsilon_P}{\varepsilon_P}\right)^2 \ll T_{\text{eff}}/\varepsilon_c$ is satified. Therefore, it breaks at $V = T = 0$, leading to the singular behavior that one can see in the blue line in Figure 3.4, where the conductance is 1 for every $\varepsilon_P \leq \varepsilon_c$ and then decreases with a discontinuity in the first derivative.

Deep in the bistable regime $\varepsilon_P \gg \varepsilon_c$

We finally consider the last regime of strong electromechanical coupling ($\varepsilon_P \gg \varepsilon_c$), for which the mechanical oscillator becomes bi-stable with two new equilibrium positions at

$x_\pm = x_0 \pm F_0/2k$ or, equivalently, $y_\pm = F_0 x_\pm/\Gamma = \pi\varepsilon_P/2\varepsilon_c$ (see the effective potential in Eq. (3.8)). In this regime, Eq. (3.36) is not valid anymore, therefore we will compute the current from another starting point: Eq. (3.35).

The elastic transmission factor of the device in absence of fluctuations, calculated at both the new equilibrium positions $y_\pm$, goes to zero quadratically as

$$\tau(y_\pm) = \frac{1}{1+y_\pm^2} = \frac{1}{1+\left(\frac{\pi\varepsilon_P}{2\varepsilon_c}\right)^2} . \tag{3.41}$$

This is a signature of the blocked-current regime of the device, the charge state of the dot being frozen either in its empty or fully occupied charge state.

Fluctuations change the conductance. To include them, we have to calculate Eq. (3.35). We first develop the potential at second order around each minimum position; it becomes $U(y) \approx \Gamma\varepsilon_c/(2\pi\varepsilon_P)\ (y-y_\pm)^2$. (This amounts to consider the system distribution as two separate gaussians, each on a different minimum.) The variance of the gaussian distribution is given by $\sigma^2 = \pi\varepsilon_P T_{\text{eff}}/(\Gamma\varepsilon_c)$; since the typical length scale of the transparency is $y_\pm$ and $\sigma \ll |y_\pm|$, we can expand the transparency at second order around $y_\pm$.

Defining $\tilde{y} = y - y_+$ and exploiting the symmetry between y_+ and y_-, the integral of Eq. (3.35) becomes

$$\begin{aligned}\langle I(x)(t)\rangle &\approx G_Q V \tau(y_\pm)\ \frac{\displaystyle\int_{-\infty}^{+\infty} \exp\left[-\frac{\tilde{y}^2}{2\sigma^2}\right]\left[1+\frac{3y_+^2-1}{(1+y_+^2)^2}\tilde{y}^2\right] d\tilde{y}}{\displaystyle\int_{-\infty}^{+\infty} \exp\left[-\frac{\tilde{y}^2}{2\sigma^2}\right] dy} \\ &\approx G_Q V \tau(y_\pm)\ \left[1+\frac{3\sigma^2}{y_+^2}\right] \approx G_Q V \tau(y_\pm)\left(1+\frac{12 T_{\text{eff}}}{\varepsilon_P}\right) .\end{aligned} \tag{3.42}$$

The conductance decays slowly as a function of the electromechanical coupling, as reproduced by the numerical curves plotted in Figure 3.4.

3.3 The effect of nonlinearities

Fluctuations populate levels at higher energy. Every energy is associated to a different trajectory in the x–p phase-space. Considering that the potential of the system is in general not harmonic, it is impossible to define a single resonance frequency: Each trajectory is associated to a different period T_E and thus to a different frequency $\omega(E) = 2\pi/T_E$. Therefore, each trajectory contributes to the power spectral density of the system at a different frequency. To sum over all their contributions and obtain the total power spectral density, it is thus fundamental to express $\omega(E)$.

3.3.1 An analytical approach

The period of the oscillator at a given energy is given by the total time that the system spends on the trajectory. To compute it, we use the simple relation $\dot{x}\,dt = dx$ and integrate it. It gives:

$$T_E = 2\int_{x_L(E)}^{x_R(E)} \frac{dx}{\dot{x}(E)} = \sqrt{2m}\int_{x_L(E)}^{x_R(E)} \frac{dx}{\sqrt{E-U(x)}}\,, \tag{3.43}$$

$$\omega_E = 2\pi/T_E\,, \tag{3.44}$$

where $x_L(E)$ and $x_R(E)$ are the inversion positions for the trajectory at energy E given by $U(x_L) = U(x_R) = E$. In the general case, there is no expression in terms of elementary functions for T_E and, consequently, for $\omega(E)$. However, it is possible to find it in the approximation in Eq. (3.9) for which only the second- and fourth-order terms of the potential are important[14, 73]:

$$\frac{\omega(E)}{\omega_0} = \frac{\pi}{2}\frac{\sqrt{A(E)}}{K[-m(E)]}\,, \tag{3.45}$$

with

$$A(E) = \frac{\varepsilon_c - \varepsilon_P}{2\varepsilon_c} + \sqrt{\frac{3(\varepsilon_c-\varepsilon_P)^2\varepsilon_c + 4\pi^2\varepsilon_P^2 E}{12\varepsilon_c^3}}\,,$$

$$m(E) = \frac{\sqrt{(\varepsilon_c-\varepsilon_P)^2 + 4\pi^2\varepsilon_P^2 E/3\varepsilon_c} - (\varepsilon_c-\varepsilon_P)}{\sqrt{(\varepsilon_c-\varepsilon_P)^2 + 4\pi^2\varepsilon_P^2 E/3\varepsilon_c} + (\varepsilon_c-\varepsilon_P)}\,,$$

and $K[-m(E)]$ is the complete elliptic integral of the first kind with parameter $-m(E)$.

At the critical point $\varepsilon_c = \varepsilon_P$ it becomes

$$\frac{\omega(E)}{\omega_0} = \left(\frac{\pi^3}{48}\right)^{\frac{1}{4}} \frac{\Gamma[3/4]}{\Gamma[5/4]} \left(\frac{E}{\Gamma}\right)^{\frac{1}{4}} \approx 1.212\left(\frac{E}{\Gamma}\right)^{\frac{1}{4}}. \tag{3.46}$$

In all other situations we can expand for small energies around the minimum position, obtaining $\omega(E) = \omega_m + \omega'(E=0)E$. Remarkably, the expression of $\omega'(E=0)$ is quite simple:

$$\omega(E) = \omega_m + \omega'(0)E, \tag{3.47}$$

$$\omega'(0) \equiv \left.\frac{d\omega}{dE}\right|_{E=0} = \frac{\pi^2}{4}\frac{\omega_0}{\varepsilon_c}\frac{\varepsilon_P^2}{\varepsilon_c^2}\left(\frac{\varepsilon_c}{\varepsilon_c-\varepsilon_P}\right)^{\frac{3}{2}}. \tag{3.48}$$

3.3.2 A numerical approach

With a numerical approach we can solve Eq. (3.43) and 3.44 in all regimes. We plot the results in Figure 3.5.

Nonlinearities imply a non-constant dispersion relation that is particularly interesting above the transition (solid line), where there is a singular value, with infinite derivative, that divides the dispersion relation in two branches: The left branch is associated to trajectories revolving around a single minimum, while the right one is for trajectories around both minima. The singular point corresponds to the energy at which the oscillator reaches the top of the barrier between the two minima (see Figure 2.3) with zero velocity, never completing the trajectory and having a zero associated frequency. The lines that we show never actually reach zero because of numerical limitations, being the singular point of measure zero in the space of real numbers.

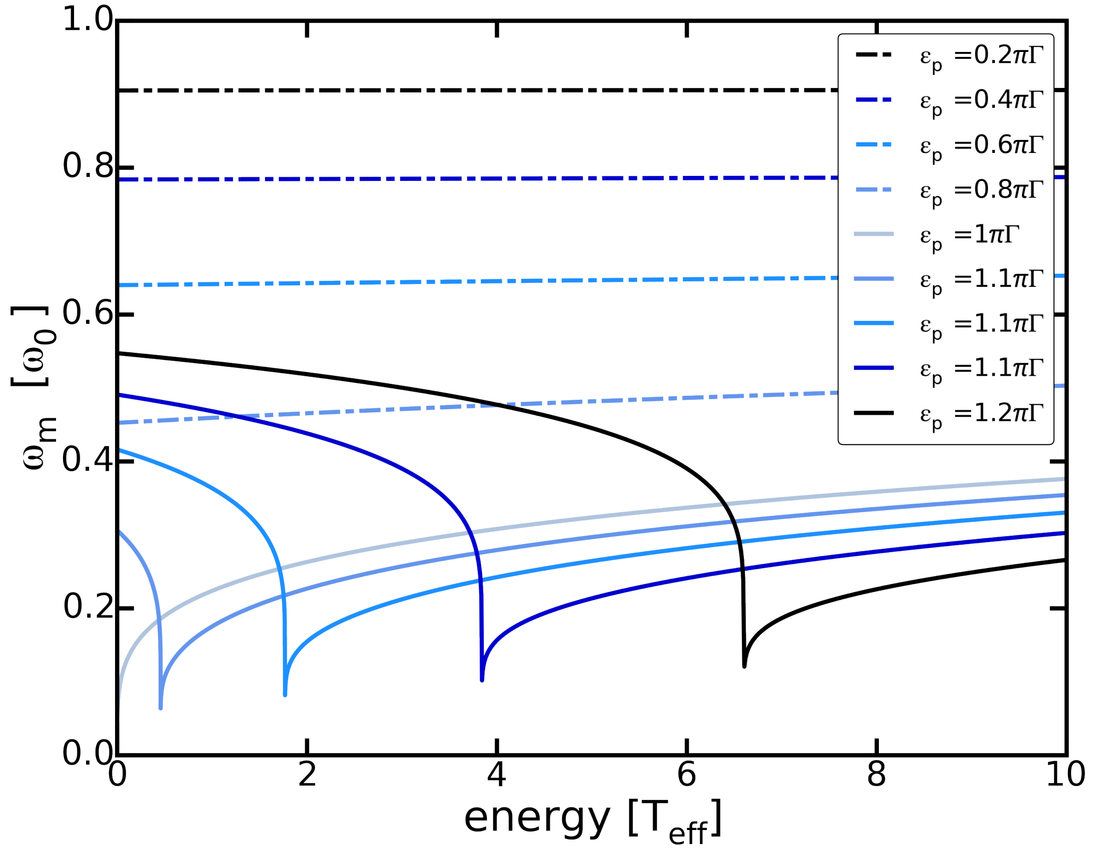

Figure 3.5: The resonance frequency for different energies. The dashed lines refer to the system in the monostable regime.

3.4 The autocorrelation functions

The autocorrelation of the physical quantity $f(t)$ is defined as $S_{ff}(t) = \langle f(t)f(0)\rangle$, while its Fourier transform is known as its *power spectral density*, or simply its *spectrum*. In experiments, it is currently possible to analyze the autocorrelation function of the electric current $S_{II}(t)$. The autocorrelation function of the displacement $S_{xx}(t)$ is still unaccessible directly, nevertheless it is interesting because it offers a simpler theoretical picture and because, being the current modulated by the displacement, it is strictly connected to $S_{II}(t)$.

One of the interests in the measurement of the current-fluctuation spectrum is that, in contrast to other observables used to detect mechanical motion like the ring-down time, there is no need to drive the resonator in order to measure its power spectral density. This allows a very low-noise measurements of the mechanical resonance frequency of the carbon nanotube to be performed. They show a tremendously high quality factor Q: it was reported a value of Q up to five millions applying this technique [66].

Also, autocorrelation functions contain much more information than just the average value of the corresponding functions: Unlike the latter, they depend on time even in the stationary state, giving thus information on the dynamic aspect of the steady-state system. For example, the spectrum of the nanotube displacement can be used to determine the resonance frequency of the system ω_M, its width $\Delta\omega$, and the corresponding quality factor Q.

Contributions to the electronic spectrum

The power spectral density of the electric current is determined by two different physical contribution: one coming from the mechanical displacement of the nanotube and the other from charge fluctuations induced by electronic shot-noise. The time-scale separation between the fast electronic degrees of freedom and the slow mechanical ones allows for their distinction.

For fixed and given x, the purely electronic contribution to the noise reads[74]

$$S^e_{II}(\omega \ll \Gamma) = \tau(x)[1-\tau(x)]\langle I\rangle\,, \tag{3.52}$$

and to obtain the observed value it is sufficient to average the above expression with $P_{\text{st}}(x,p)$. Notice that this contribution to the spectrum is flat for $\omega \ll \Gamma$; therefore this noise doesn't contribute to determining the resonance frequency $\omega_M \approx \omega_0$.

For this reason, we will neglect the purely electronic contribution in the body of our work.

Current- and displacement-fluctuation spectra are defined as

$$S_{II}(\omega) = \int_{-\infty}^{+\infty} dt e^{-i\omega t}\left[\langle I[x(t)]I[x(0)]\rangle - \langle I[x(0)]\rangle^2\right]\,, \tag{3.49}$$

$$S_{xx}(\omega) = \int_{-\infty}^{+\infty} dt e^{-i\omega t}\left[\langle x(t)x(0)\rangle - \langle x]\rangle^2\right]\,. \tag{3.50}$$

As already done for $S_{xx}(\omega)$ in Eq. (2.61), we can compute $S_{II}(\omega)$ numerically following Pistolesi et al. [17][1]:

$$S_{II}(\omega) = -2\text{Tr}\left[(\hat{I}-\langle I\rangle)\frac{\mathcal{L}_0}{\omega^2+\mathcal{L}_0^2}(\hat{I}-\langle I\rangle)P_{\text{st}}\right]\,, \tag{3.51}$$

where $\hat{\hat{I}}$ is the operator that at each point in the x-p phase space associates its value $I-\langle I\rangle$ and we remember that $\mathcal{L}_0$ is the Fokker-Planck matrix that comes from writing Eq. (2.49) as $\partial_t P = \mathcal{L}_0 P$ while P_{st} is the steady-state solution given in Eq. (2.50).

The analytical results for $S_{xx}(\omega)$ are presented in Figure 3.6. From there, one can see the critical softening at mean field (orange dashed line) and the presence also of higher order harmonics, as well as the broadening of the line around the critical point, represented by the black blob in the bottom-right corner.

In the next section we will calculate the power spectral densities analytically.

3.4.1 Analytic calculations of $S_{xx}(\omega)$

Following Dykman *et al.* [75], in the regime of very small damping rate $A/m \ll \Delta\omega$, Eq. (3.50) can be approximated by

$$S_{xx}(t) = \int dx_0 dp_0 P_{\text{st}}(x_0,p_0)\tilde{x}_{x_0p_0}(t)\tilde{x}_{x_0p_0}(0). \tag{3.53}$$

---

[1] See the box for more details

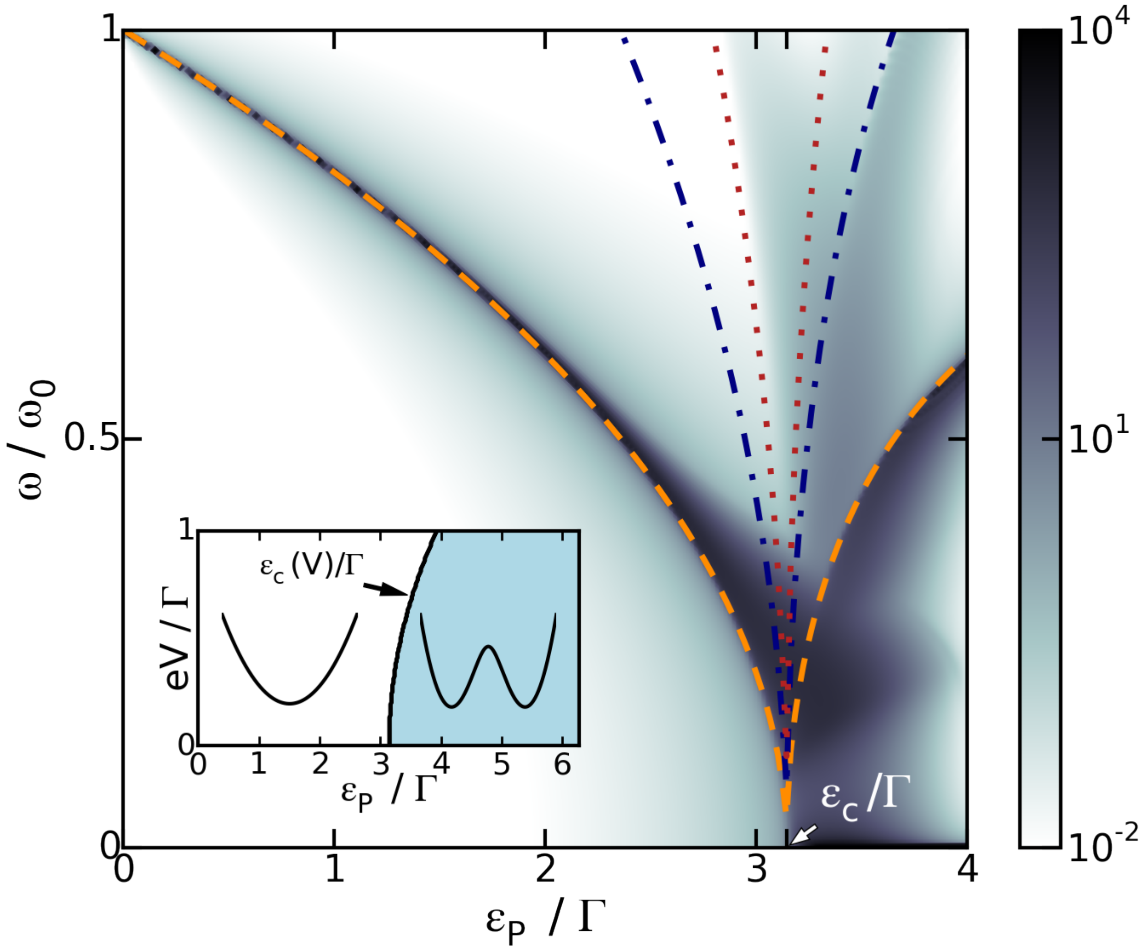

Figure 3.6: Density plot of S_{xx} as a function of ω and ε_P. The values of ω_m (orange dashed line), $2\omega_m$ (blue dot-dashed line), and $3\omega_m$ (red dotted line) are shown. The units of S_{xx} are $x_{\text{zpm}}^2/\omega_0 = (m\omega_0^2)^{-1}$, where $x_{\text{zpm}} = (m\omega_0)^{-1/2}$ is the zero-point motion displacement. The symmetry of the potential implies that only odd harmonics are present for $\varepsilon_P < \varepsilon_c$. Inset: phase diagram in the plane eV-ε_P for the stability of the effective potential. Taken from [14].

where $x(t)$ is the periodic function that satisfies the equation of motion $m\ddot{x} = F(x)$ with initial conditions $x(0) = x_0$ and $\dot{x}(0) = p_0/m$, and $\tilde{x}_{x_0p_0}(t) = x_{x_0p_0}(t) - \langle x_{x_0p_0}(t)\rangle$.

The integral is calculated over the whole phase space for the classical oscillator and $P_{\text{st}}(x,p)$ is the stationary distribution given in Eq. (2.50). The damping A/m and the fluctuation D enter this expression in defining the form of P_{st}, but not in the dynamics of $x(t)$.

In the limit of small dissipation, the nanotube oscillates many times on a trajectory at fixed energy E before changing it. Therefore, it is convenient to go to the phase space identified by the energy E and the time over the trajectory τ. The expression Eq. (3.53) can be rewritten as follows:

$$\int_0^{+\infty} dE \int_0^{T(E)} d\tau P_{\text{st}}(E)\tilde{x}_E(t+\tau)\tilde{x}_E(\tau), \tag{3.54}$$

where $T(E)$ is the period of the closed trajectory $x_E(t)$ of fixed energy E and $P_{\text{st}}(E) = \mathcal{N}e^{-E/T_{\text{eff}}}$.

Since $x(t)$ is periodic with period $T(E) = 2\pi/\omega(E)$, we can introduce its Fourier series

$\tilde{x}_E(t) = \sum_n e^{in\omega(E)t} x_n(E)$. The spectrum then takes the form:

$$S_{xx}(\omega) = \int_0^{+\infty} dE \mathcal{P}(E) \sum_n 2\pi\delta(\omega - n\omega(E)) x_n^2(E) \,, \tag{3.55}$$

with $\mathcal{P}(E) = P_{\rm st}(E)T(E)$ and $\omega(E)$ calculated in Eq. (3.45).

Finally, introducing the energies E_n which satisfy the equation $\omega = n\omega(E_n)$, we obtain the expression for the spectral function (with $\omega > 0$) as:

$$S_{xx}(\omega) = \mathcal{N} \frac{(2\pi)^2}{\omega} \sum_{n=0}^{+\infty} \frac{e^{-E_n/T_{\rm eff}}}{|\omega'(E_n)|} x_n^2(E) \,. \tag{3.56}$$

The computation of S_{xx} is now reduced to the computation of $x_n^2(E)$. This is done analytically for two limiting cases: (i) The oscillator is weakly nonlinear, with the quartic term just a small perturbation to the quadratic one ($\varepsilon_P \ll \varepsilon_c$). (ii) The oscillator is purely quartic, with the vanishing of the quadratic term ($\varepsilon_P = \varepsilon_c$).

Case (i) weakly nonlinear oscillator

Sufficiently far from the transition ($\varepsilon_P \ll \varepsilon_c$), we can treat the quartic part of the potential as a small perturbation. We can thus calculate S_{xx} by expanding Eq. (3.56) to leading order in the nonlinearity. The main contribution comes from the first harmonic whose amplitude can be approximated with the harmonic expression $x_1^2(E) \approx E/2m\omega_0^2$. The energy-dependent resonating frequency is approximated by the expression (cf. Eq. (3.48)):

$$\omega(E) = \omega_m + \omega'(0)E + \ldots \tag{3.57}$$

where $\omega_m/\omega_0 = (1 - \varepsilon_P/\varepsilon_c)^{1/2}$. We obtain then:

$$S_{xx}(\omega) = \frac{\pi}{m\omega_m\omega|\omega'(0)|} \frac{\omega - \omega_m}{\omega'(0)T_{\rm eff}} e^{-\frac{\omega-\omega_m}{\omega'(0)T_{\rm eff}}} \,. \tag{3.58}$$

From Eq. (3.58) and Figure 3.7 we see that the spectral density has a maximum at

$$\omega_M = \omega_m + \omega'(0)T_{\rm eff} \tag{3.59}$$

and is defined only for $\omega > \omega_m$. (There is actually an upper bound of the order of ω_0, but the effective temperature being very low this limit is not visible.) The full width at half maximum (FWHM) of the spectral line $\Delta\omega$ reads

$$\Delta\omega \approx 2.446 \; \omega'(0)T_{\rm eff} \,, \tag{3.60}$$

corresponding to the FWHM in Figure 3.7.

We thus find that the effect of the nonlinearity on the width of the resonance is linear with the effective temperature and controlled by $\omega'(0)$, at least as far as the quartic term does not become dominant. At the end of the next subsection we will estimate the range of validity of this approach by comparing its result with the one obtained from the purely quartic oscillator.

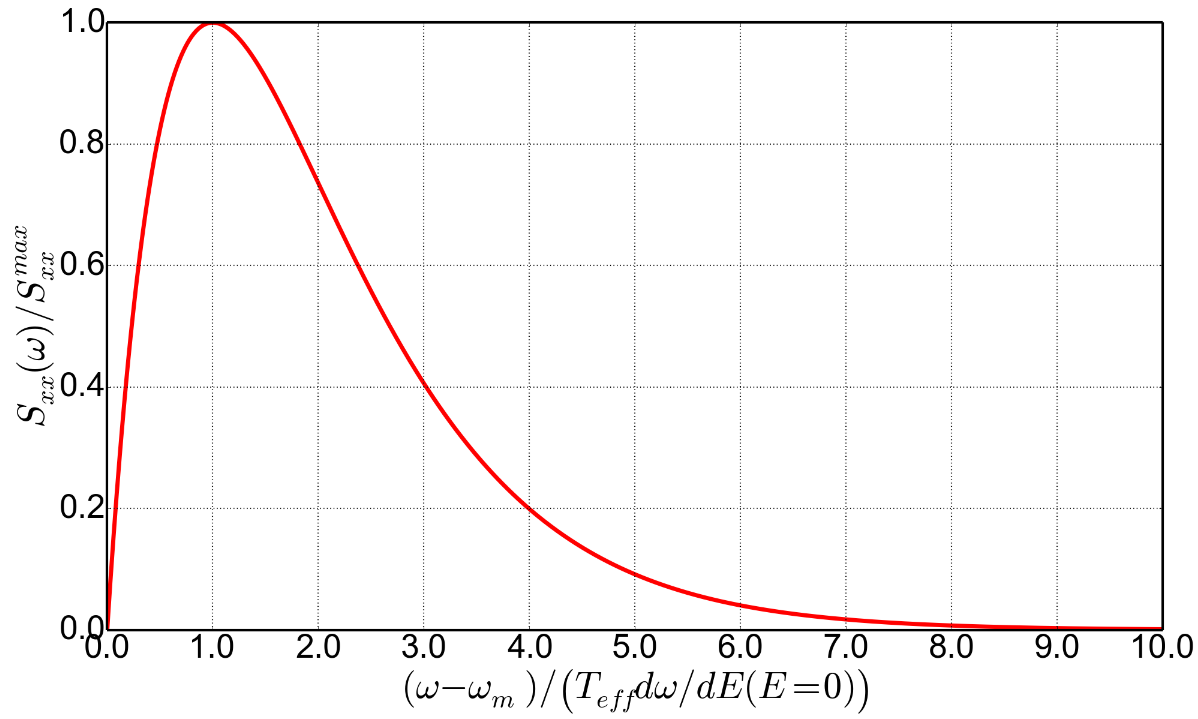

Figure 3.7: Normalized displacement spectral density $S_{xx}(\omega)/S_{xx}^{\max}$ as a function of the rescaled frequency $(\omega-\omega_m)/\omega'(0)T_{\text{eff}}$ in the case of weak electromechanical coupling $\varepsilon_P \ll \varepsilon_c$. Taken from [14].

Case (ii) purely quartic oscillator

At the critical point ($\varepsilon_P = \varepsilon_c$), the quadratic part of the potential vanishes and the mechanical oscillator becomes purely quartic. In this regime, we obtain for the oscillator frequency (cf. Eq. (3.46)):

$$\frac{\omega(E)}{\omega_0} = B\left(\frac{E}{\Gamma}\right)^{1/4}, \tag{3.61}$$

with $B \approx 1.212$. Therefore the oscillator frequency is proportional to $(E/\Gamma)^{1/4}$.

Remarkably, the displacement spectral density of the quartic oscillator also has a simple analytical expression:

$$S_{xx}(\omega) = \tilde{B}\frac{\Gamma^2}{\omega_0 F_0^2}\left(\frac{\Gamma}{T_{\text{eff}}}\right)^{3/4}\sum_{n=1}^{+\infty} e^{-E_n/T_{\text{eff}}}\frac{\alpha_n^2 E_n}{n\Gamma},$$

where

$$\alpha_n = \frac{1}{f(1)}\int_{-1}^{1} du \frac{u}{\sqrt{1-u^4}}\cos\left(n\pi\frac{f(u)}{f(1)}\right) \tag{3.62}$$

is a parameter depending on the harmonic index n and involving the integral function

$$f(u) = \int_{-1}^{u}\frac{dv}{\sqrt{1-v^4}}, \tag{3.63}$$

and $\tilde{B} = 16 \cdot (27\pi)^{\frac{1}{4}} f(1)/\Gamma[3/4] \approx 103.9$, while the energy E_n satisfies the equation

$$\omega = n\omega(E_n) \implies E_n = \frac{3f^4(1)}{\pi^5 n^4}\frac{\omega^4}{\omega_0^4}\Gamma \approx \frac{0.463}{n^4}\frac{\omega^4}{\omega_0^4}\Gamma \tag{3.64}$$

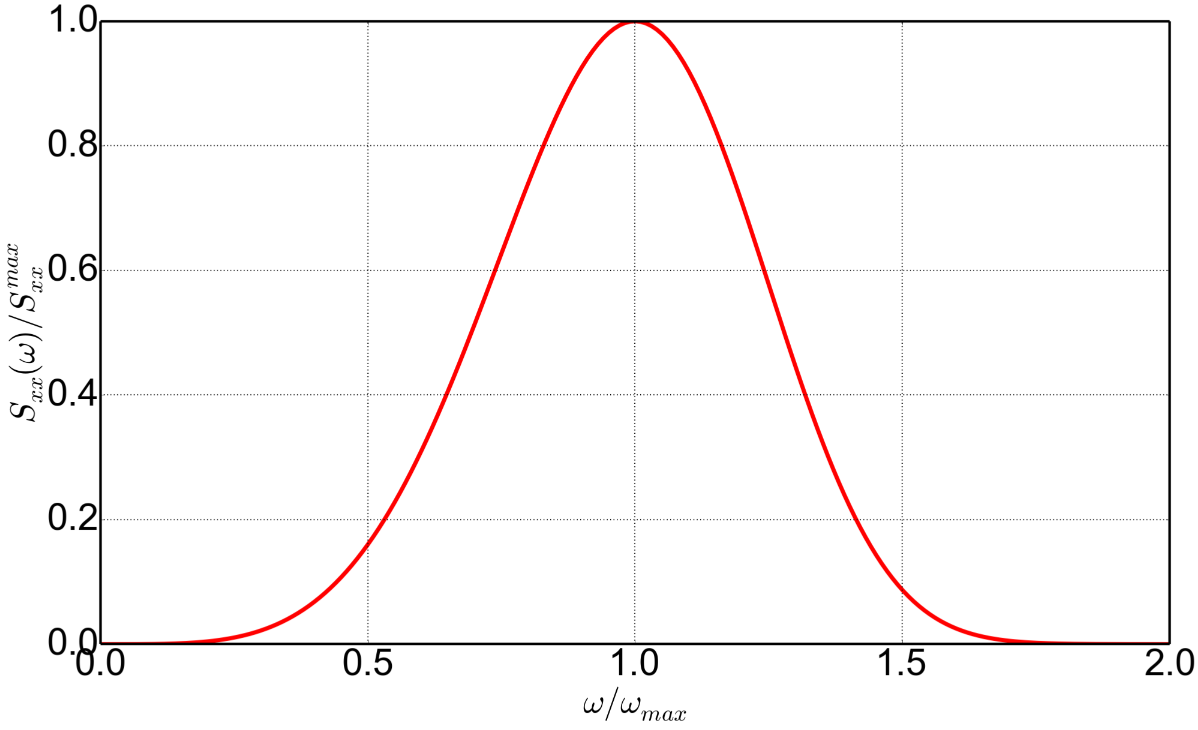

Figure 3.8: Normalized displacement spectral density $S_{xx}(\omega)/S_{xx}^{max}$ as a function of the rescaled frequency ω/ω_M at the critical point ($\varepsilon_P = \varepsilon_c$). The spectral line maximum is located at frequency $\omega_M = B\omega_0 \left(eV/4\Gamma\right)^{1/4}$. Taken from [14].

We evaluate numerically the values of α_n for the first harmonics:

$$\alpha_1 \approx -0.477, \qquad \alpha_3 \approx -0.021, \qquad \alpha_5 \approx -9.3 \cdot 10^{-4}\,. \tag{3.65}$$

In Eq. (3.4.1), the main contribution to $S_{xx}(\omega)$ is given by the first harmonic $n = 1$, the other harmonics $n \geq 3$ having a smaller weight. The normalized line shape of the displacement spectral density can be further approximated retaining only the contribution of the first harmonic:

$$\frac{S_{xx}(\omega)}{S_{xx}(\omega_M)} \approx \left(\frac{\omega}{\omega_M}\right)^4 e^{-\left[\left(\frac{\omega}{\omega_M}\right)^4 - 1\right]}\,, \tag{3.66}$$

where

$$\omega_M \approx 1.212\omega_0 \left(\frac{T_{\text{eff}}}{\Gamma}\right)^{\frac{1}{4}} \tag{3.67}$$

is the position of the maximum of the spectral density. From Eq. (3.66) and Figure 3.8, we see that the spectral density has a different line shape compared to the weak non linear oscillator in Figure 3.7. Its FWHM is given by

$$\Delta\omega \approx 0.585\,\omega_M\,, \tag{3.68}$$

corresponding to the FWHM in Figure 3.8.

In contrast to the quasi-harmonic oscillator [see Eq. (3.60)], the resonance width of the quartic oscillator at the critical point does not scale linearly with the effective temperature, but with a scaling law $\propto (T_{\text{eff}}/\Gamma)^{1/4}$.

Let us finally find the range of validity of the approximation used in Sec. 3.4.1. We first remark that $\Delta\omega$ in Eq. (3.60) diverges close to the transition, indicating the breakdown

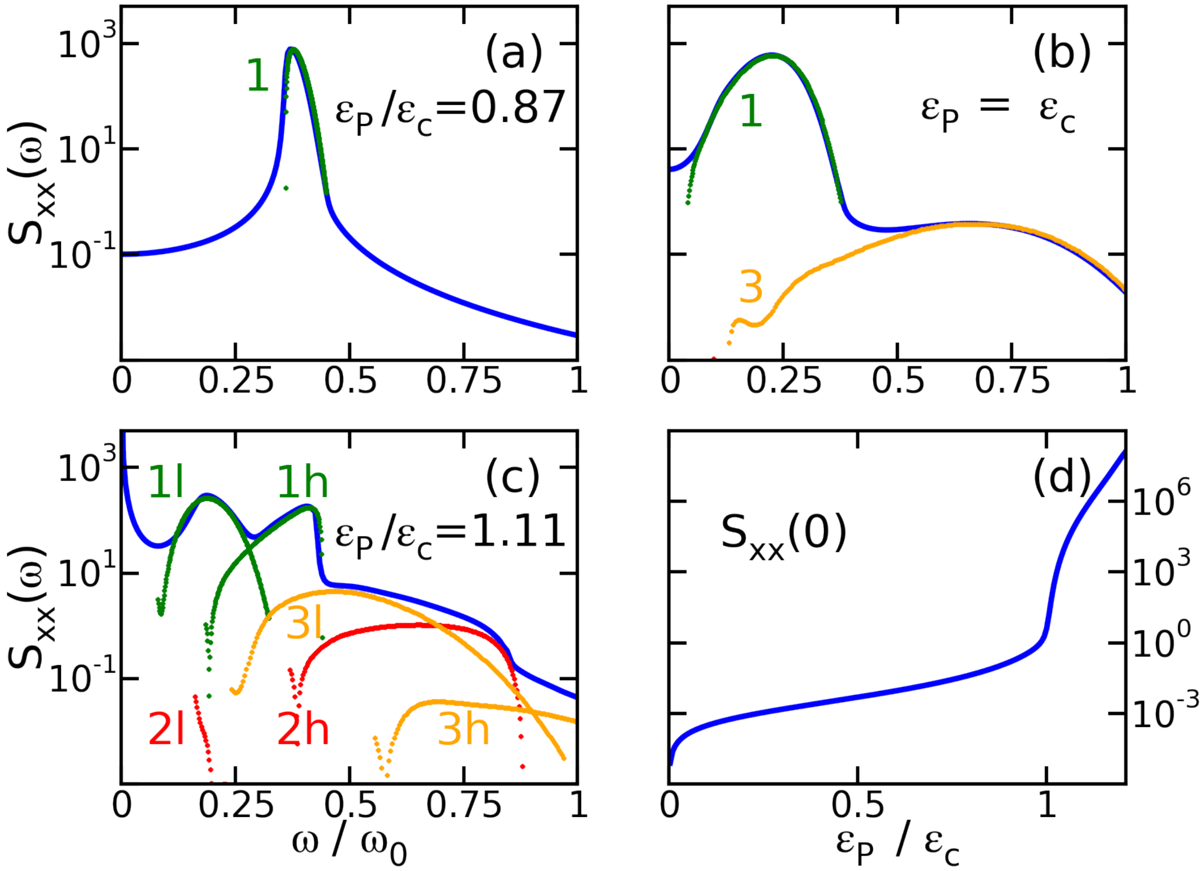

Figure 3.9: Comparison of the full numerical solution of the Fokker-Planck equation for S_{xx} (blue solid lines) with the one obtained with Eq. (3.55) (dots) for $\varepsilon_P/\varepsilon_c = 0.87$, 1, 1.11 (a, b, and c panel, respectively) in units of $(m\omega_0^2)^{-1}$. The numbers label the order of the harmonic, while the letters h and l in the c panel indicate the high- and low-frequency contributions. Panel d: $S_{xx}(0)$ as a function of ε_P/Γ indicating the onset of the telegraph noise at the transition. Taken from [14].

of the quasi-harmonic approximation. At the transition, $\Delta\omega$ expressed in Eq. (3.68) is finite. We estimate the crossover between both regions to happen when both estimations of the resonance width $\Delta\omega$ in Eq. (3.60) and in Eq. (3.68) are equal; we find it to be for $1-\varepsilon_P/\varepsilon_c \approx 1.71(eV/\varepsilon_c)^{1/2}$.

Comparison of the analysis

To test our results, we numerically solved Eq. (3.55) for the first harmonics and compared the results with those coming from the numerical solution of Eq. (2.61). As we can see from Figure 3.9, the agreement is remarkable and extends even after the criticality. On that purpose, let us focus a little on the double peak of the spectral function for $\varepsilon_P > \varepsilon_c$: In this case, as we have already seen, the system is bistable. However, the barrier between the two meta-stable states grows as the electromechanical coupling increases. For $\varepsilon_P - \varepsilon_c \ll \varepsilon_c$, it is still low enough to allow some of the higher-energy states to travel around both minima in a period. Their period of oscillation is thus roughly double the period of the oscillation around a single minimum, implying a halved resonance frequency. Therefore, the high-frequency peak can be explained by the contributions of the low-energy trajectories that revolve around each minimum, while the low-frequency one by the high-energy trajectories revolving around both minima.

3.4.2 Analytic calculation of $S_{II}(\omega)$

The current fluctuation spectrum $S_{II}(\omega)$ is particularly interesting because it can be measured in absence of a driving force[7]. It can be connected to the mechanical displacement spectrum, but the relation between the two is not always straightforward, particularly when close to the transition[15].

First of all, we refer to Eq. (3.49) for the definition of $S_{II}(\omega)$. We thus consider only the current fluctuations originating from the displacement fluctuation. We can write

$$S_{II}(\omega) = \int_{-\infty}^{+\infty} dt e^{i\omega t} \langle \tilde{I}[x(t)]\tilde{I}[x(0)]\rangle \,, \tag{3.69}$$

with $\tilde{I}(x) = \hat{I}(x) - \langle I(x)\rangle$ and $I(x)$ given by Eq. (3.33). At zero-temperature, we use Eq. (3.35) to derive

$$S_{II}(t) = G_Q^2 V^2 \langle \tilde{\tau}[x(t)]\tilde{\tau}[x(0)]\rangle \ . \tag{3.70}$$

where $\tilde{\tau} = \tau - \langle \tau(t)\rangle$. An expansion of the transmission factor τ around the equilibrium position(s) of the oscillator relates the current spectrum $S_{II}(\omega)$ to the displacement spectrum (see Eq. (3.50)). Thanks to this, we can calculate $S_{II}(\omega)$ analytically in the regime of very small damping rate $A/m \ll \Delta\omega$, with $\Delta\omega$ the width of the main peak in the spectral density induced by the oscillator non-linearity, as we have done for $S_{xx}(\omega)$ in the previous section. Following the method introduced in references [14, 15] and based on ref. [76], the auto-correlation function for the current fluctuations in this regime can be well approximated by (see Eq. (3.53))

$$S_{II}(t) = (G_Q V)^2 \int_0^{+\infty} dE \int_0^{T_E} d\tau P_{st}(E,\tau)\tilde{\tau}[x_E(t+\tau)]\tilde{\tau}[x_E(\tau)] \,. \tag{3.71}$$

In the next paragraphs we present the results for the current spectrum in different regimes.

S_{II} for weak coupling $\varepsilon_P \ll \varepsilon_c$

The procedure we use is more or less the same as for the $S_{xx}(\omega)$. The effective potential has a single minimum at $x_0 = F_0/2k$, around which the system oscillates. When the amplitude of these oscillations is sufficiently small (essentially for $T_{\text{eff}} \ll \Gamma$, see also the section on the finite temperature) we can expand the transmission factor as $\tau[x(t)] \approx 1 - [F_0 \tilde{x}(t)/\Gamma]^2$. This leads to the following expression for the current fluctuations:

$$S_{II}(t) \approx (G_Q V)^2 \left(\frac{F_0}{\Gamma}\right)^4 \left\langle \tilde{x}^2(t)\tilde{x}^2(0)\right\rangle \ . \tag{3.72}$$

In this regime the probability distribution given by 2.50 is still Gaussian, and one can apply Wick theorem to Eq. (3.72) to directly relate the current spectrum to the displacement spectrum. In Fourier transform:

$$S_{II}(\omega) = 2(G_Q V)^2 \left(\frac{F_0}{\Gamma}\right)^4 \int_{-\infty}^{+\infty} \frac{d\omega'}{2\pi} S_{xx}(\omega-\omega') S_{xx}(\omega') \,. \tag{3.73}$$

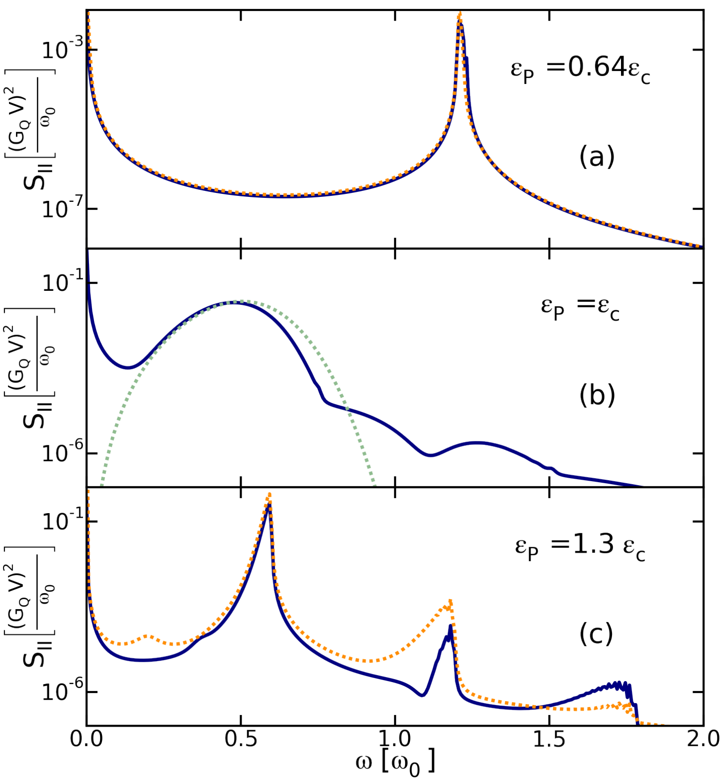

Figure 3.10: Power spectral density of current fluctuations $S_{II}(\omega)$ for different values of the coupling constant $\varepsilon_P/\varepsilon_c = 0.64,\ 1,\ 1.3$ (as indicated in each panel) and for $\Gamma/\omega_0 = 10^3$, $V/\Gamma = 5 \cdot 10^{-3}$, $T = 0$. Blue solid lines give the result of the numerical evaluation of Eq. (3.51), while dotted lines show analytical results: In panel (a) the (orange) dotted line represents the convolution of the mechanical fluctuations $S_{xx}(\omega)$, as given in Eq. (3.73). In panel (b) the (green) dotted line gives the analytical result of current fluctuations coming from Eq. (3.78). In panel (c) the (orange) dotted line is proportional to S_{xx}, as written in Eq. (3.82). Image taken from [15].

To conclude, for extremely small $\varepsilon_P \ll \varepsilon_c$ the displacement spectrum $S_{xx}(\omega)$ shows two Lorentzian peaks at frequencies $\pm\omega_m$ whose width is dominated by the dissipation $A/m \gg \Delta\omega$. Therefore, $S_{II}(\omega)$ will show three Lorentzian peaks, centered at $\omega = 0$ and $\omega = \pm 2\omega_m$ and with a width $2A/m$.

S_{II} for intermediate coupling $\varepsilon_P < \varepsilon_c$

As for $S_{xx}(\omega)$, the nonlinearity in the potential generates a finite width in $\Delta\omega$; when $\Delta\omega \gg A/m$ the Gaussian approximation for the probability distribution cannot be used anymore. We can nevertheless directly calculate the current spectrum using Eq. (3.71). We expand $x_E(t)$ in Fourier series and we restrict to the first harmonics ($n = \pm 1$). We find that the spectral density has two contributions, one regular and one singular [we define $f_1(u) = u^2 e^{-u}$]:

$$S_{II}(\omega) \approx S_{II}^{\text{reg}}(\omega) + S_{II}^{\text{sing}}(\omega)\,, \tag{3.74}$$

$$\frac{S_{II}^{\text{reg}}(\omega)}{(G_Q V)^2} = \frac{\pi}{4}\frac{\varepsilon_P^2}{\Gamma^2}\frac{\omega_m T_{\text{eff}}}{|\omega'(0)|\Gamma^2\omega}\ f_1\left(\frac{\omega - 2\omega_m}{2\omega' T_{\text{eff}}}\right)\,, \tag{3.75}$$

$$\frac{S_{II}^{\text{sing}}(\omega)}{(G_Q V)^2} = \frac{7\pi^5}{2}\frac{\varepsilon_P^2 T_{\text{eff}}^2}{\varepsilon_c^2(\varepsilon_c - \varepsilon_P)^2}\ \delta(\omega)\,. \tag{3.76}$$

If properly taken into account, the dissipative terms would broaden the singular contribution by $2A/m$. It is interesting to notice that this sharp low-frequency contribution is not related to telegraph noise, due do the hopping of the system between two metastable states, since there is a single minimum of the potential.

The location ω_M of the maximum of the power spectral density and the full width at half maximum $\Delta\omega$ of the spectral line read

$$\begin{aligned}\omega_M &= 2\left(\omega_m + 2\omega' T_{\text{eff}}\right), \\ \Delta\omega &\approx 6.79\ \omega' T_{\text{eff}}.\end{aligned}$$

We notice that these quantities are roughly twice what we obtained for the displacement spectrum (see Eq. (3.59) and 3.60). The numerical results obtained from Eq. (3.51) in this regime are shown in Figure 3.10 panel (a). A comparison with the analytical calculation (dotted line) shows that the agreement is very good. We observe that the peak at vanishing frequency appears also in the non-Gaussian limit and that its width is of the same order of width dominated by the non-linear fluctuations of the peak at $\omega \approx 2\omega_m$.

S_{II} at the transition $\varepsilon_P = \varepsilon_c$

The probability distribution is no longer Gaussian, because the potential is purely quartic, $U(y) = (\Gamma/12\pi)y^4$. We can't use Wick's theorem here, but we can evaluate the current spectrum analytically directly using Eq. (3.71). As we have seen for the displacement spectrum, the first harmonic of the oscillator displacement reads

$$x_1(E) \approx -0.477\frac{\Gamma}{F_0}\left(12\pi\frac{E}{\Gamma}\right)^{\frac{1}{4}} \tag{3.77}$$

The spectrum has the form given by Eq. (3.74) with

$$S_{II}^{\text{reg}}(\omega) \approx 6.797\frac{(G_Q V)^2}{\omega_0}\left(\frac{T_{\text{eff}}}{\Gamma}\right)^{3/4} f_2\left(\frac{\omega}{\omega_M}\right) \tag{3.78}$$

$$S_{II}^{\text{sing}}(\omega) \approx 30.2(G_Q V)^2\frac{T_{\text{eff}}}{\Gamma}\delta(\omega), \tag{3.79}$$

with a universal line-shape of the resonance given by $f_2(u) = u^6 e^{-3/2(u^4-1)}$. From these expression we infer that the maximum position and its width are [2]

$$\frac{\omega_M}{\omega_0} \approx 2.68\left(\frac{T_{\text{eff}}}{\Gamma}\right)^{1/4} \qquad \Delta\omega \approx 0.479\,\omega_M\,, \tag{3.80}$$

In analogy to the displacement spectrum, we find that the peak in the noise spectrum has a universal quality factor $Q = \omega_M/\Delta\omega$; however, in this case its value is approximately 2.09, while for the displacement spectrum it is 1.71. The difference is a signature of the non-Gaussian fluctuations breaking the simple relation (3.73).

In Figure 3.10-(b) we compare the prediction of Eq. (3.78) (green-dotted line) with the full numerical calculation obtained with Eq. (3.51) (full line). The overall shape of the main peak is well reproduced. We verified that the small over-estimation (the plot is in logarithmic scale) of the peak width is due to the absence in the analytical calculation of the sixth-order term of the potential.

---

[2] The numerical coefficients in Eqs. 3.78, 3.79, and 3.80 are given by

$$\begin{aligned}B_1 &= 216\alpha_1^4\frac{\mathbf{\Gamma}\left[\frac{5}{4}\right]}{\mathbf{\Gamma}\left[\frac{3}{4}\right]^2}\left(\frac{4\pi^5}{3e^6}\right)^{1/4} \approx 6.797\,, \\ B_2 &= 24\pi^2\alpha_1^4\frac{4\mathbf{\Gamma}\left[\frac{7}{4}\right]\mathbf{\Gamma}\left[\frac{3}{4}\right] - \mathbf{\Gamma}\left[\frac{5}{4}\right]^2}{\mathbf{\Gamma}\left[\frac{3}{4}\right]^2} \approx 30.2\,. \\ B_3 &= \frac{\pi}{(2\pi)^{1/4}}\frac{\mathbf{\Gamma}\left[\frac{3}{4}\right]}{\mathbf{\Gamma}\left[\frac{5}{4}\right]} \approx 2.68\end{aligned}$$

S_{II} **in the bistable phase** $\varepsilon_P > \varepsilon_c$

An analytical description in the bistable regime is difficult for electromechanical couplings still close to the critical value $\varepsilon_P \geq \varepsilon_c$, but as soon as the potential minima become sufficiently deep, we can again describe the system as a set of two harmonic oscillators around the new minima. Therefore, for $\varepsilon_P \gg \varepsilon_c$, the probability distribution becomes Gaussian around each minimum, representing the blocked current state in the occupied and empty electronic state.

As a consequence of the Gaussianicity of the distribution, Wick theorem still holds if we expand displacement fluctuations separately around each minimum $x_\pm = x_0 \pm F_0/2k$. We can thus evaluate Eq. (3.70) obtaining:

$$\begin{aligned} S_{II}(t) = 2\left(G_Q V\right)^2 \tau \Bigg[&(1-\tau)\frac{F_0^2 S_{xx}(t)}{\Gamma^2} + \tau^3(3-4\tau)^2 \left(\frac{F_0^2 S_{xx}(t)}{\Gamma^2}\right)^2 + \\ &12\tau(1-\tau)(1-2\tau)\frac{F_0^2 \langle x^2(t)\rangle}{\Gamma^2}\frac{F_0^2 S_{xx}(t)}{\Gamma^2}\Bigg] . \end{aligned} \tag{3.81}$$

(Note that we recover Eq. (3.73) if we set $\tau = 1$.)

For strong coupling, $\tau \ll 1$ and Eq. (3.81) can be approximated as

$$S_{II}(\omega) \approx 2\left(G_Q V \frac{F_0}{\Gamma}\right)^2 \tau(1-\tau) S_{xx}(\omega) . \tag{3.82}$$

Deep in the bistable regime we thus find that a simple linear relation between $S_{II}(\omega)$ and $S_{xx}(\omega)$ holds. In Figure 3.10-(c) we plot $S_{II}(\omega)$ obtained from Eq. (3.82) in orange-dotted line, compared to the full numerical calculation of Eq. (3.51). We see that all the features are well reproduced with a reasonably good quantitative agreement.

3.5 Explaining the low Q-factor: The ring-down behavior

Figure 3.9 and Figure 3.10 show a very low value of the quality factor of the oscillator close to the transition, that we analytically computed to be of the order of 1, meaning that the width of the spectrum is of the same order of ω_0. However, this can not be explained with the dissipation of the system, which is several orders of magnitude smaller. The reason is to be found in the dephasing that occurs to the statistical ensemble of harmonic oscillator due to frequency noise.

First of all, the ring-down of a system is the transient happening after a driving is suddenly switched off: The oscillator loses its energy and slowly drifts towards the equilibrium position. What happens in our system is that all the oscillators go back to equilibrium in a slightly different way because they are subject to a different realization of the stochastic force due to the quantum fluctuation of electrons. Their trajectories, being slightly different, very soon lose their coherence; after a very short time their phase is completely random. Therefore, their position averages to zero, while every single realization has still energy left that needs to be dissipated. This creates two different timescales, the dephasing time γ_ϕ^{-1} and the dissipation time γ_E^{-1}, which satisfy $\tau_\phi \ll \tau_E$ at the transition. The dephasing time τ_ϕ is also the responsible for the width of the spectrum, as we will see later.

3.5.1 Analytical calculation of the ring-down displacement

We first impose a driving for negative times, then study the evolution of $\langle x(t)\rangle$ and $\langle E(t)\rangle$ over all the realizations for positive times. The decay of $\langle E(t)\rangle$ is influenced only by the energy dissipation of the system, whose timescale is given by γ_E^{-1}. This is because the energy is not oscillating over time, so the average is insensitive to the frequency noise. Instead, the decay of $\langle x(t)\rangle$ is given by the two different timescales γ_ϕ^{-1} and γ_E^{-1}.

We thus calculate these two quantities and compare them to see the effects of the dephasing, showing that they become predominant close to the transition.

For a discussion on the system under driving, we refer to Sec. 2.5.3. The evolution equation for the probability distribution is given by ($\mathcal{L}_D = -F_D\partial_p/2$):

$$\partial_t P(t) = \{\mathcal{L}_0 + 2\mathcal{L}_D \cos(\omega_D t)\} P(t)\,. \tag{3.83}$$

One can show that, for weak driving, an approximate solution of Eq. (3.83) has the form

$$P(x_0, p_0, t) = P_{st}(x_0 - x_i(t), p_0 - p_i(t))\,, \tag{3.84}$$

where $x_i(t)$ and $p_i(t)$ are solutions of the equations of motion

$$\begin{cases} \dot{x}_i(t) = p_i(t)/m \\ \dot{p}_i(t) = F(x_i) + F_D\cos(\omega_D t) - A(x_i)p_i(t)/m \end{cases} . \tag{3.85}$$

Eq. (3.84) says that, in the weak driving limit, the probability distribution for the driven oscillator is obtained by moving rigidly the center of the stationary Gibbs distribution along the deterministic trajectory of the damped oscillator.

If the driving is weak also compared to the effective temperature, one can expand $P(x_0, p_0, t)$ to linear order in the driving strength:

$$P(x_0, p_0, t) \approx P_{st}(x_0, p_0)\left\{1 - \frac{x_i(t)F(x_0) - p_i(t)p_0/m}{T_{\text{eff}}}\right\} . \tag{3.86}$$

The ring-down dynamics at time $t > 0$ is encoded into the average response of the oscillator displacement:

$$x(t) = \iint dx_0 dp_0 P(x_0, p_0, 0) x_{x_0,p_0}(t). \tag{3.87}$$

For simplicity we choose $x_i(0) = x_i$ and $p_i(0) = 0$. This means that the driving is turned off exactly at the moment when the oscillator is standing still and inverting its trajectory. This additional constraint that we put has no impact on the result, since we will be interested in the envelope of all the possible situations, but allows for easier calculations. Introducing Eq. (3.86) and $\tilde{x}_{x_0p_0}(t) = x_{x_0p_0}(t) - \langle x_{x_0p_0}(t)\rangle$ inside Eq. (3.87), we obtain:

$$\tilde{x}(t) \approx -\frac{x_i}{T_{\text{eff}}} \int dx_0 \int dp_0 P_{st}(x_0, p_0) F(\tilde{x}_0) \tilde{x}_{x_0,p_0}(t)\,, \tag{3.88}$$

which can be rewritten as:

$$\tilde{x}(t) \approx -\frac{x_i}{T_{\text{eff}}} \int_0^{+\infty} dE \int_0^{T(E)} dt P_{st}(E) F[\tilde{x}_E(0)] \tilde{x}_E(t) \,. \tag{3.89}$$

To calculate this integral, we first perform the Fourier expansion of the periodic trajectories $\tilde{x}_E(t) = \sum_n e^{in\omega(E)t} x_n(E)$, as we did also in Sec. 3.4.1. Then, we expand the force in Eq. (3.1) to third order in x and take, as usual, two different limits: Weak coupling, i.e. small third-order term, and critical coupling, i.e. vanishing linear term. Doing that, we can further average over energy and phase of the orbit in Eq. (3.89):

$$\begin{aligned}\tilde{x}(t) \approx & \frac{x_i}{T_{\text{eff}}} \int_0^{+\infty} dE \mathcal{P}(E) \left\{ m\omega_m^2 \sum_n x_n^2(E) e^{in\omega(E)t} + \right. \\ & \left. \sum_{\{n_i\}} \frac{F_0^4 x_{n_1}(E) x_{n_2}(E) x_{n_3}(E) x_{n_4}(E)}{3\pi m \Gamma^3} e^{in_4\omega(E)t} \delta_{n_4, \sum_{j=1}^3 n_j} \right\} .\end{aligned} \tag{3.90}$$

Eq. (3.90) enables to compute the ring-down dynamics of the oscillator displacement $\tilde{x}(t)$ as well as to extract a characteristic dephasing time γ_φ^{-1} of the mechanical oscillator.

Weakly non linear oscillator

Far from the transition ($\varepsilon_P \ll \varepsilon_c$), the oscillator is weakly non-linear, and we can use the same approximations as in Sec.3.4.1 to derive from Eq. (3.90) an analytical expression for the oscillator displacement:

$$\tilde{x}(t) \approx x_i \frac{\left(1 - \gamma_\varphi^2 t^2\right) \cos(\omega_m t) - 2\gamma_\varphi t \sin(\omega_m t)}{\left(1 + \gamma_\varphi^2 t^2\right)^2} \,, \tag{3.91}$$

where the dephasing time γ_φ^{-1} of the oscillator is given by:

$$\gamma_\varphi^{-1} = \frac{1}{\omega'(0) T_{\text{eff}}} \,. \tag{3.92}$$

Eq. (3.91) shows that after the driving has been switched off, the oscillator follows an oscillating behavior given by the natural frequency of the vibration $\omega_m = \omega(0)$. This fast oscillation decays as a power law, in contrast to the exponential relaxation expected from the energy dissipation.

As a result, we find that the typical decay or dephasing time γ_φ^{-1} of the oscillator is inversely proportional to the broadening of the displacement spectral density $\Delta\omega$ (see Eq. (3.60)), namely:

$$\Delta\omega \approx 2.446 \gamma_\varphi \,. \tag{3.93}$$

Purely quartic oscillator

At the critical point ($\varepsilon_P = \varepsilon_c$), the quadratic part of the potential vanishes and the mechanical oscillator becomes purely quartic. We adopt the same approximations as in Sec.3.4.1 to derive from Eq. (3.90) an analytical expression for the oscillator displacement:

$$\frac{\tilde{x}(t)}{\tilde{x}(0)} \approx \frac{1}{\Gamma[7/4]} \int_0^{+\infty} dy y^{\frac{3}{4}} e^{-y} \cos\left(y^{\frac{1}{4}} \omega_M t\right) , \tag{3.94}$$

where the frequency $\omega_M = 1.212\omega_0 \left(T_{\text{eff}}/\Gamma\right)^{1/4}$ is the same as in Sec.3.4.1.

3.5.2 Numerical calculation of the ring-down displacement

To numerically calculate the ring-down displacement we use the solution given by Eq. (2.58) as the initial condition for the moment $t = 0$ when the driving is turned off. Then, we find $\tilde{x}(t)$ and $E(t)$ from the time evolution of the probability distribution in absence of driving, that is, with $\mathcal{L} = \mathcal{L}_0$.

Let's write the probability distribution at $t = 0$ as the sum between the stationary distribution in absence of driving P_{st} and a correction δP. The evolution for positive times (no more driving) is given by

$$\partial_t \left[P_{\mathrm{st}} + \delta P(t)\right] = \mathcal{L}_0 \left[P_{\mathrm{st}} + \delta P(t)\right] \implies \partial_t \delta P(t) = \mathcal{L}_0 \delta P(t)\,, \tag{3.95}$$

where we used the fact that $\partial_t P_{\mathrm{st}} = \mathcal{L}_0 P_{\mathrm{st}} = 0$.

However, from a numerical point of view, the calculation of $\delta P(t)$ is very expensive. Therefore, we use the Laplace transform, which is defined as $\delta P(z) = \int_0^{+\infty} \delta P(t) \exp(-zt) dt$. Eq. (3.95) thus becomes

$$\left[\partial_t \delta P(t)\right]_z = z\delta P(z) - \delta P(t = 0) = \mathcal{L}_0 \delta P(z)\,, \tag{3.96}$$

where the first equality comes from the properties of the Laplace transform. Notice that we have to keep the initial condition $\delta P(t = 0)$.

The displacement $\tilde{x}(t)$ from the equilibrium position x_0 is determined only by $\delta P(t)$. It reads

$$\tilde{x}(t) = \iint (\hat{x} - x_0)\delta P(x, p, t)\; dx\; dp\,, \tag{3.97}$$

where the integral is taken over all the phase space x-p. We take the Laplace transform of the previous equation and substitute the probability distribution using Eq. (3.96). We obtain finally:

$$\langle \tilde{x}(z) \rangle = \mathrm{Tr}\left[\hat{\tilde{x}}(z - \mathcal{L}_0)^{-1} P(t = 0)\right]\,. \tag{3.98}$$

Similarly, we can calculate the Laplace transform of the total energy by letting $\hat{\tilde{x}} \to E(\hat{x}, \hat{p})$ in Eq. (3.98). One can then obtain the time dependence by numerically implementing the Cauchy theorem

$$\langle \tilde{x}(t) \rangle = \oint_C \langle \tilde{x}(z) \rangle e^{-zt} dz/(2\pi i), \tag{3.99}$$

where C is a contour that encloses the poles of $\langle \tilde{x}(z) \rangle$ for $\mathrm{Re}z < 0$.

We find that the energy exponentially decays on the scale γ_E^{-1}, even at the transition. On the other hand, as shown in Figure 3.11, $\langle \tilde{x}(t) \rangle$ decays on a much shorter scale γ_φ^{-1}. Figure 3.11-d shows the ε_P dependence of $\Delta\omega$, $2\gamma_\varphi$, and γ_E. The width $\Delta\omega$, obtained from S_{xx}, coincides within the numerical accuracy with $2\gamma_\varphi$, proving that frequency noise is the responsible of the faster decay of $\langle \tilde{x}(t) \rangle$. Both present a pronounced maximum at $\varepsilon_P = \varepsilon_c$, indicating the transition.

A complete comparison of the result with the two methods is given in Figure 3.11.

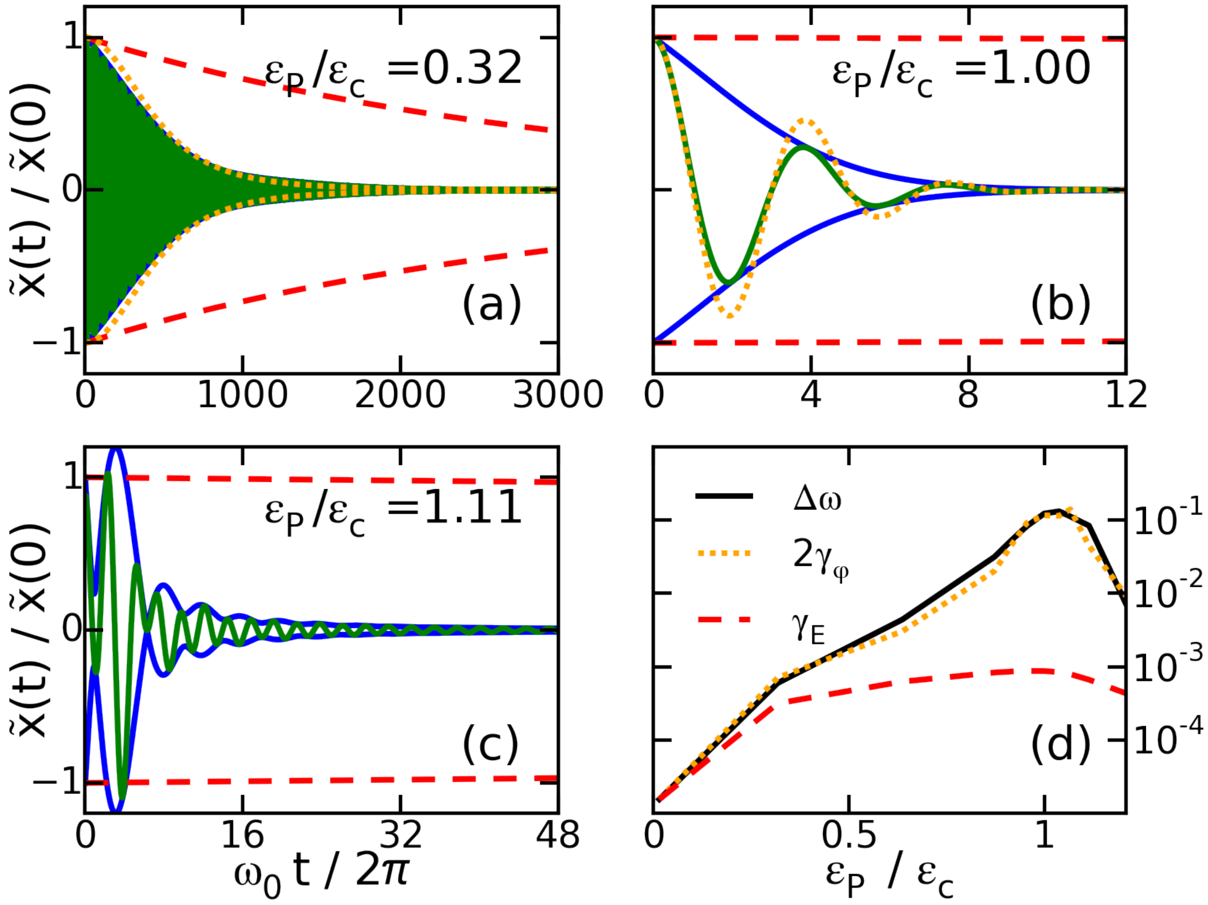

Figure 3.11: Time dependence of $\langle\tilde{x}(t)\rangle$ (green solid line) and its envelope (blue solid line) for $\varepsilon_P/\varepsilon_c =$ 0.32, 1, and 1.11 (a, b, and c panel, respectively). The exponential decay on the scale $2/\gamma_E$ is shown red dashed. In panel a and b the orange dotted line gives the result of the analytical expressions discussed in the text. Panel d: comparison of the ε_P-dependence of $\Delta\omega$, $2\gamma_\varphi$, and γ_E. Image taken from [14].

3.6 The influence of asymmetry on displacement and current spectra

We continue here the discussion we started in Sec. 3.1.4 on the effect of a detuning of the electronic level $\tilde{\varepsilon}$ inside the nanotube. We have seen that, at mean-field level, the detuning causes an asymmetry in the potential that reflects in a decrease of the softening of the oscillator. In particular, at the critical value $\varepsilon_P = \varepsilon_c$, the softening has a singular cusp shape as a function of the detuning. We can expect this feature to be altered by fluctuations, or at least smoothened. To verify it, we analyze now the autocorrelation functions of the oscillator.

3.6.1 The displacement spectrum

We obtain the displacement and current spectra using the numerical methods described in Sec. 3.4.

We study first the evolution of the resonance frequency of the oscillator ω_M, defined as usual as the frequency where the displacement spectra $S_{xx}(\omega)$ is maximum, as a function of the detuning of the dot (see solid lines in Figure 3.12 and 3.14). The dotted lines show the analytical mean-field value ω_m as obtained from Eq. (3.16), with the exception of the

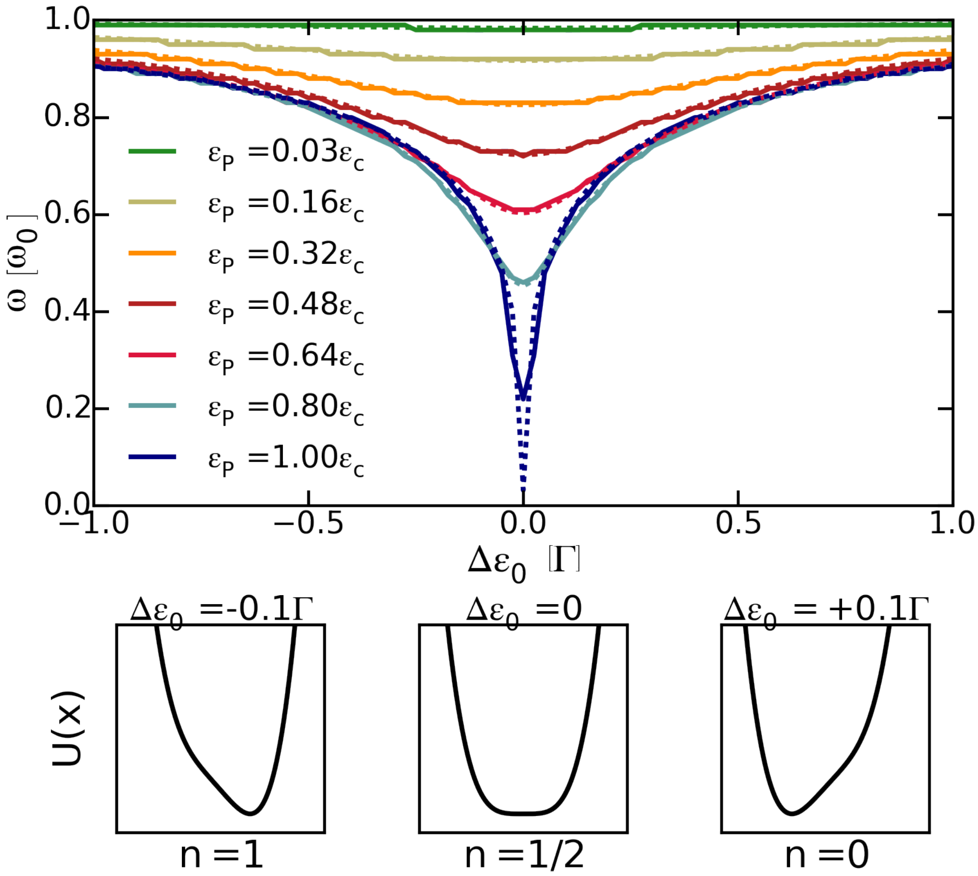

Figure 3.12: Softening as a function of the gating for various ε_P. The dotted lines indicate the numerical solution of the mean field equations, Eq. (3.12), and solid lines are the numerical results with fluctuations. Below, the potential is plotted for an energy range (vertical axis) of $4T_{\mathrm{eff}}$. Adapted from [15].

black dotted line, at criticality, which is calculated using Eq. (3.17).

The resonance frequency of the oscillator, both considered with (ω_M) or without (ω_m) fluctuations, is minimum for symmetric gating and symmetric with the detuning of the dot level. For weak coupling, i.e. $\varepsilon_P \approx 0.03 - 0.32\varepsilon_c$, the dependence is quadratical and thus smooth; at the criticality, however, it is much sharper and goes with $(\Delta\varepsilon_0/\Gamma)^{1/3}$.

For $\varepsilon_P \ll \varepsilon_c$ the agreement between ω_m and ω_M is essentially perfect, while for $\varepsilon_P = \varepsilon_c$ we have ω_M sensibly larger than ω_m for a perfectly tuned system. Again, the interplay between strong nonlinear form (x^4) of the potential at criticality and fluctuations is at the origin of this difference: It prevents ω_M to reach the critical value of the softening $\omega_m = 0$ that is expected by mean-field calculations; we remark that the values in this case have already been calculated explicitly in Eq. (3.7) and Eq. (3.67). Things are slightly different for a detuned system: At finite value of $\tilde{\varepsilon}$, the effective potential of the oscillator gets an asymmetric minimum (see lower panel of Figure 3.12) which is responsible for a non-vanishing $\omega(E = 0) = \omega_m$, as given by Eq. (3.17). As a consequence, at sufficiently large detuning $\tilde{\varepsilon} \geq 0.1\Gamma$, the peak follows again the mean-field prediction.

As explained before, the calculation of ω_M gives only a hint about the mechanical dynamics, which are actually much more complex. As an example, we plot the full numerical evaluation of the displacement noise at criticality in color code in Figure 3.13 (left panel, the right panel shows the current noise). Here, we have a close look at what happens around the symmetric point. We see the emergence of a secondary peak that is not described by the mean-field mode softening for small dot-level detuning ($\tilde{\varepsilon} < 0.05\Gamma$). This is due to the dispersion relation $\omega(E)$ of the oscillator developing a minimum at a

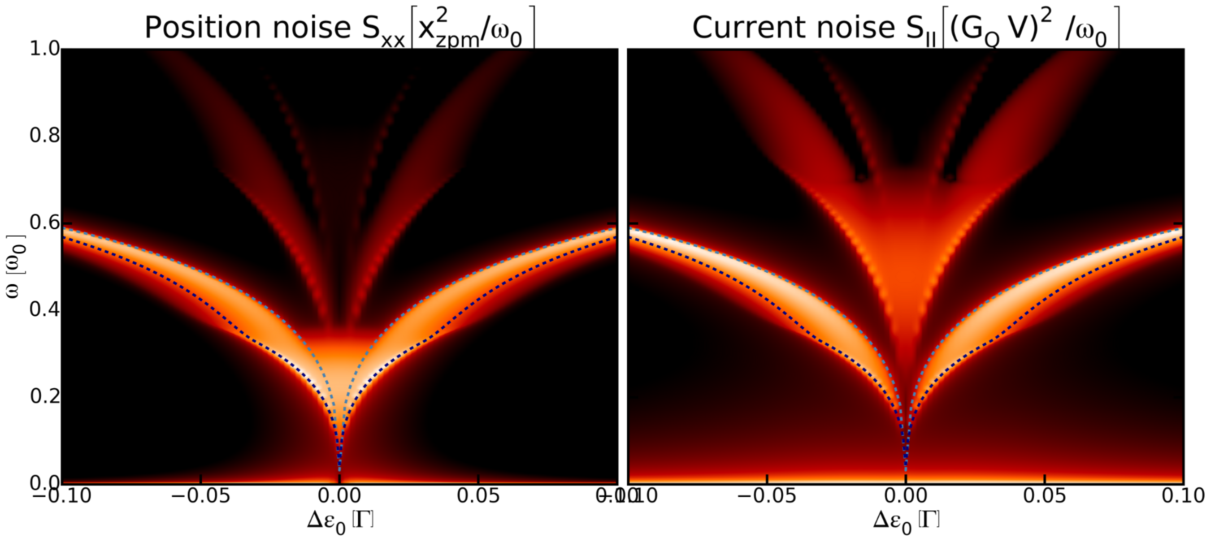

Figure 3.13: Density plot of the displacement-spectrum S_{xx} (left panel) and current spectrum S_{II} (right panel) at criticality ($\varepsilon_P = \varepsilon_c$) as a function of dot-level detuning $\Delta\varepsilon_0$ and frequency ω. The dashed light-blue line shows the position of ω_m from the solution of Eq. (3.12) and Eq. (3.13). The dashed dark-blue line shows the position of $\omega(E_0)$ at which the dispersion relation has a minimum. The maximum value in the density scale has been chosen according to the most important finite-frequency peak, and the minimum value has been chosen 4 orders of magnitude below. The plot is presented in logarithmic scale. Note that a zero-frequency noise peak is present and is typically several orders of magnitude above the max of the scale, especially in the current plot. The parameters are the same of the previous two figures. Taken from [15].

finite value of the energy $E_0(\tilde{\varepsilon}) > 0$, as can be seen from Figure 3.5: For $\omega \approx \omega(E_0)$ one can show that there is a square-root divergence of the spectrum

$$S_{xx}(\omega) \propto E_0\sqrt{\frac{\omega''(E_0)}{2\left[\omega - \omega(E_0)\right]}}. \tag{3.100}$$

This divergence is broadened only by dissipation and thus leads to a very narrow peak. The double-peak feature rapidly disappears close to criticality, where one recovers the spectrum described by Eq. (3.66), and also for larger detuning, where it is cut off by the exponentially small probability of populating the state with energy $E_0(\tilde{\varepsilon})$.

Particularly interesting is the case $\varepsilon_P > \varepsilon_c$, of which we have plotted an example in Figure 3.14 for $\varepsilon_P = 1.1\varepsilon_c$. As we have seen analytically in Eq. (3.20), we expect a cusp in the mean-field peak position close to $\tilde{\varepsilon} = 0$. This is also found numerically at least for $\tilde{\varepsilon}$ not too small – branch (1) in the plot. When we look more in details close to $\tilde{\varepsilon} = 0$, we find two minima in the effective potential, one stable and one meta-stable. We assign the peaks in branch (1) to oscillations around the stable minimum. The contribution of the meta-stable state rapidly vanishes due to its population, exponentially small in the regime $T_{\text{eff}} \ll \Gamma$. It can still be seen close to its merging with the stable-minimum peak, arising at branch (2). However, its presence is fundamental to generate branch (3), that is associated to oscillations around both minima and of which frequency is roughly half the frequency of branch (1).

3.6.2 Relation between current and displacement spectra

We can calculate also the current spectrum. We show in Figure 3.13 the result for $\varepsilon_P = \varepsilon_c$. In order to understand the relation with the displacement spectrum one can generalize

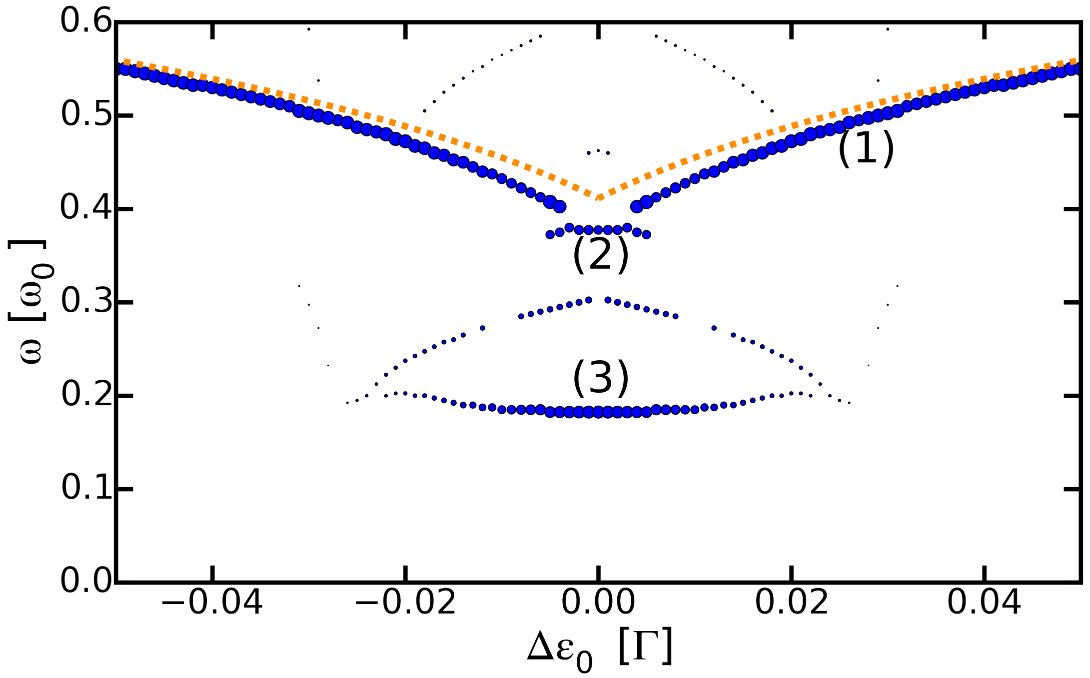

Figure 3.14: Same as Fig. 3.12 but for $\varepsilon_P = 1.1\varepsilon_c$, corresponding to the bistable region. The orange dotted lines indicate the numerical solution of the mean field equations, Eq. 3.12. The dots indicate the positions of the dominant maxima in the $S_{xx}(\omega)$ spectrum (see next chapter), with a dot size proportional to the peak height. Adapted from [15].

Eq. (3.70):

$$\begin{aligned}\frac{S_{II}(t)}{(F_0/\Gamma)^2} \approx (G_Q V)^2\, \tau^3 \Big\{ & 4(1-\tau) S_{xx}(t) \\ & + \frac{\Gamma^2}{F_0^2}\tau(3-4\tau)^2 \left[\langle y^2(t) y^2(0)\rangle - \langle y^4(0)\rangle\right] \\ & + \frac{\Gamma^2}{F_0^2} 16(1-\tau)(1-2\tau) \left[\langle y(t) y^3(0)\rangle - \langle y^4(0)\rangle\right] \Big\}\end{aligned} \qquad (3.101)$$

The first term in Eq. (3.101) is proportional to the mechanical noise $S_{xx}(t)$. It dominates the spectral signal for detuned dot-level position ($\Delta\varepsilon_0 \neq 0$ and $\tau \neq 1$) and is at the origin of the double V-shape seen in Figure 3.13-(b). The second and third terms in Eq. (3.101) are related to the fourth-order correlation functions of the oscillator position. The second term dominates the spectrum in the region close to the critical point ($\Delta\varepsilon_0 = 0$ and $\tau = 1$). The line-shape in this regime is well reproduced by Eq. (3.78) giving the regular part of the spectral density. Finally, we remark the presence of a low-frequency noise due to the singular part of the spectral density written in Eq. (3.79).

To conclude, we have seen that the transition to the bistable phase can be detected by studying the displacement or current spectrum as a function of the detuning of the single-electron level. Specifically the shape of the softening depends strongly on the value of the interaction and a cusp should appear for coupling larger than the critical value. Fluctuations smoothen the picture, but the characteristic cusp should be a valuable indication of the true nature of the transition.

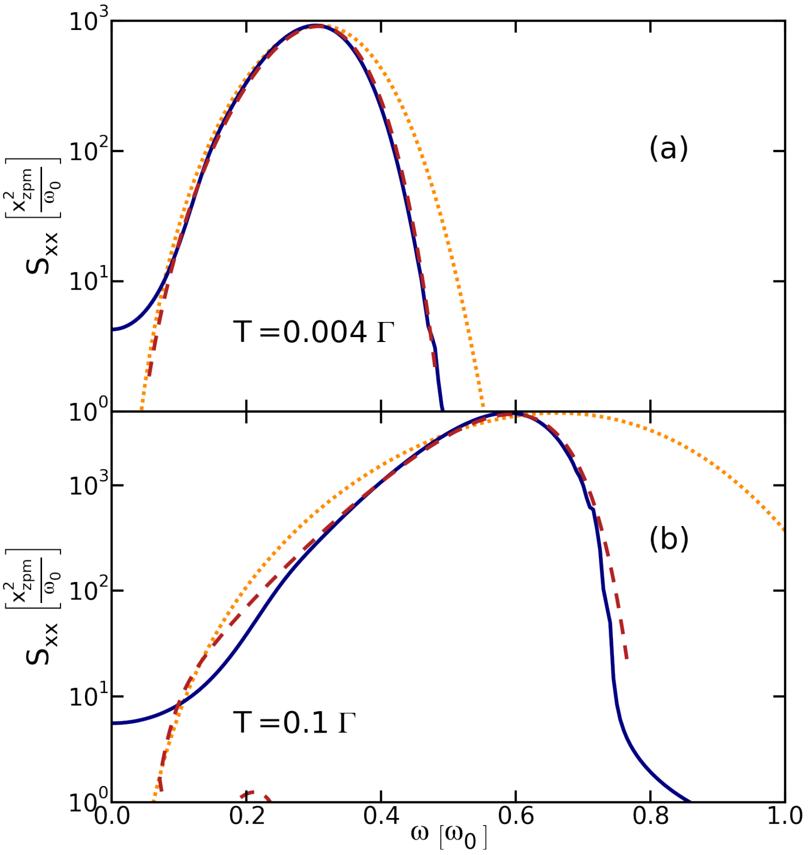

Figure 3.15: $S_{xx}(\omega)$ for (a) $T/\Gamma = 4{\cdot}10^{-3}$ and (b) $T/\Gamma = 0.1$. Solid blue lines show the numerical results from Eq. (2.61), dotted orange lines the analytical low-T approximation of Eq. (3.66), and dashed red lines Eq. (3.53) evaluated numerically on the exact potential. The low temperature approximation works very well even for $T = 0.1\Gamma$, panel (b), provided we use the full potential and not just its fourth-order approximation. Adapted from [15].

3.7 Effect of thermal fluctuations on mechanical noise

An important test for our theory to pass is how it works at finite temperature, since the zero temperature condition is not reachable in real experiments. Also, strictly speaking, it doesn't make much sense to talk about zero temperature in our model, that is based on the assumption that $T \gg \omega_0$. Therefore, in this section we will consider the effect of a finite temperature on the displacement spectrum, continuing the discussion started in Sec. 3.1.5 about the effects of the temperature in the mean-field theory.

Statistical physics says that, at thermal equilibrium (thus $V = 0$ in our case), the distribution function always has a Gibbs form

$$P(E,\tau) = \frac{1}{Z} e^{-\frac{E}{T_{\text{eff}}}} \,, \tag{3.102}$$

with $T_{\text{eff}} = T$. One can thus obtain both the current and the displacement spectrum from expressions like Eq. (3.71), the only difference being the specific form of the effective potential U that leads to different expressions for $\omega(E)$ and $x_E(t)$.

Specifically, at the critical line the quadratic term vanishes and, as long as the quartic term dominates over the higher order terms, the universal line-shape for $S_{xx}(\omega)$ given in Eq. (3.66) holds, provided a renormalized value of the maximum position of the peak ω_M:

$$\omega_M(T) \approx 1.212\omega_0 \left(\frac{T}{\Gamma}\right)^{\frac{1}{4}} \left[1 - \frac{\pi^2}{2}\left(\frac{T}{\Gamma}\right)^2\right] . \tag{3.103}$$

Hence, with increasing temperature, the maximum of the spectral line $S_{xx}(\omega)$ moves toward higher frequencies and its width increases. In the upper panels of Fig. 3.15 we plot

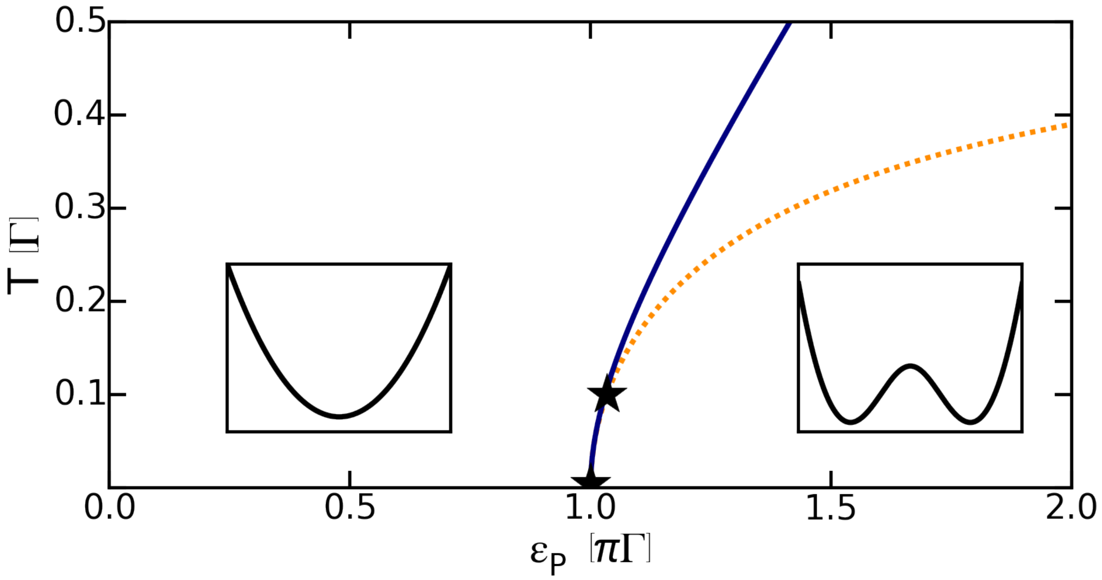

Figure 3.16: Phase diagram of the system in the plane T-ε_P; the bistability is only on the right (see potential in the insets). Numerical (solid blue) and analytical (dotted orange, Eq. (3.24), valid for $T \ll \Gamma$) transition lines are shown. The blackstars indicate the values at which the two panels of Figure 3.15 are calculated. Adapted from [15].

the displacement spectrum $S_{xx}(\omega)$ obtained at two different temperatures: $T/\Gamma = 4 \cdot 10^{-4}$ [panel (a)] and $T/\Gamma = 0.1$ [panel (b)]; the orange dotted line presents the analytical results given by Eq. (3.66) and the blue solid line presents the full numeric calculations given by Eq. (3.51). We observe that the analytical results are qualitatively consistent with the numerics, and more specifically the peak shifts toward higher frequencies and the resonance enlarges with increasing temperature. However a quantitative discrepancy is evident, especially in panel (b). This is due to the sixth and higher order terms becoming important because of the increase of thermal fluctuations. Here is why: Let's assume that the distribution function is $P \sim e^{-U_4 x^4/T}$. We can then evaluate the contribution of any term in the expansion of $U(y)$:

$$\langle x^n \rangle = \frac{\mathbf{\Gamma}\left[\frac{n+1}{4}\right]}{\mathbf{\Gamma}\left[\frac{1}{4}\right]} \left(\frac{T}{U_4}\right)^{n/4} . \tag{3.104}$$

We thus find that

$$\frac{U_n \langle x^n \rangle}{U_4 \langle x^4 \rangle} \sim \frac{U_n}{U_4} \left(\frac{T}{U_4}\right)^{\frac{n-4}{4}} \tag{3.105}$$

From expression (Eq. (3.32)) one finds that $U_n \sim \Gamma$ for $T \to 0$. This gives the necessary condition $(T/\Gamma)^{(n-4)/4} \ll 1$ in order to neglect the term of order n with respect to the term of order 4. For the case in panel (b) the condition for the sixth terms reads $\sim \sqrt{T/\Gamma} \approx 0.3$, so the sixth order term is already important. We verified that evaluating numerically the expression equivalent to Eq. (3.71) for S_{xx} with the exact form of the potential (see dashed lines in the figure) we recover the results of the full numerical solution.

3.8 The effects of a dissipative coupling

Up to this moment, we considered the coupling with the electrons to be the only source of dissipation of the system. In this section we consider the effect of a coupling to a

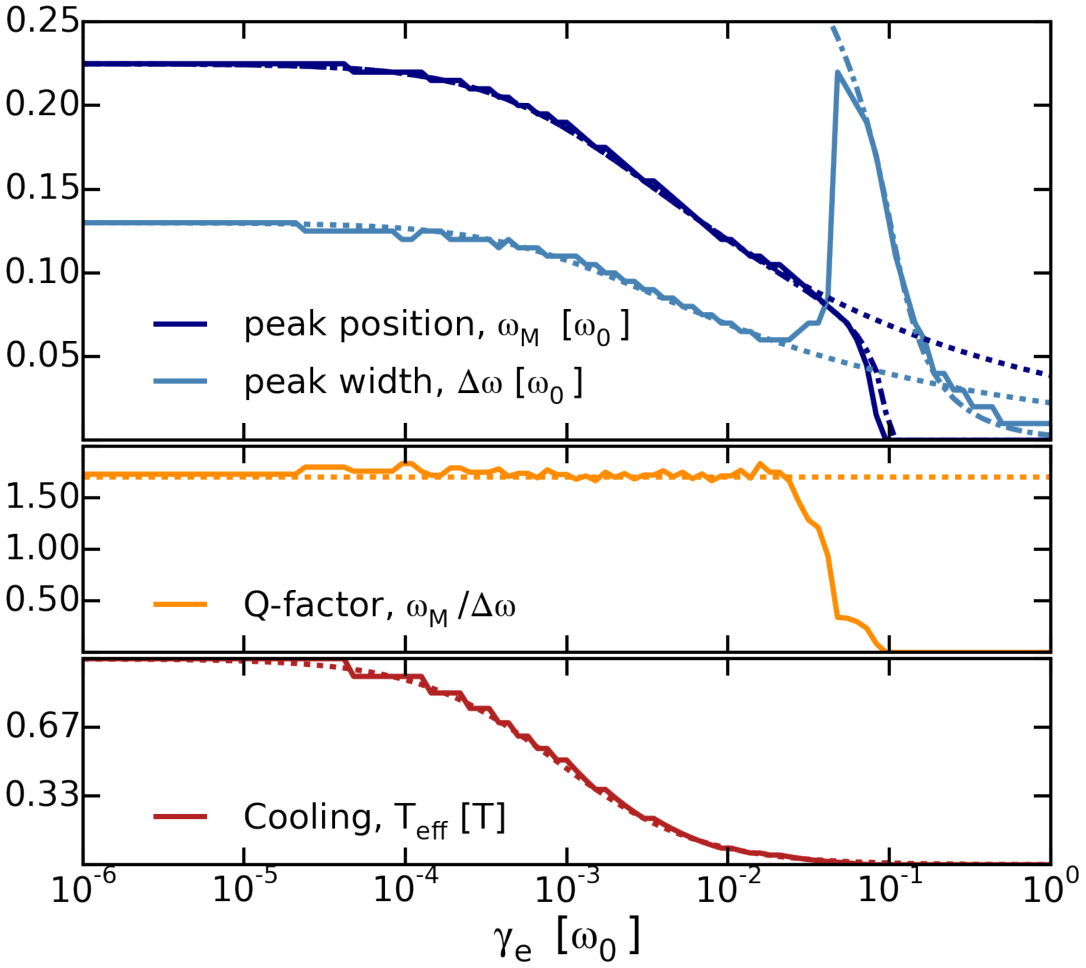

Figure 3.17: We plot as a function of the damping constant γ_e the position and the width of the maximum of $S_{xx}(\omega)$ (upper panel), the quality factor (middle panel), and the effective temperature T_eff (lower panel). Solid lines represent the numerical results obtained by solving the Fokker-Planck equation. The dashed lines in the upper and central panel indicate the evolution of ω_m and $\Delta\omega$ given by the analytical expression $\omega_M = 1.2\omega_0(T_\mathrm{eff}/\Gamma)^{1/4}$ and $Q = \omega_M/\Delta\omega = 1.71$ valid at criticality. The dot-dashed line in the upper panel is given by Eq. (3.111) and Eq. (3.110). The parameters are $\Gamma = 1000\,\omega_0$, $\varepsilon_P = \varepsilon_c$, $T = 0$, and $V/\Gamma = 5 \cdot 10^{-3}$. Adapted from [15].

bath at the same temperature of the electronic degrees of freedom, but with an independent coupling constant modeled by the damping rate γ_e. The fluctuations induced by this coupling satisfy the fluctuation-dissipation theorem, leading to a modification of the Fokker-Planck Eq. (2.49) as follows:

$$\frac{A}{m} \to \frac{A}{m} + \gamma_\mathrm{e}, \qquad D \to D + 2\gamma_\mathrm{e} m T\,. \tag{3.106}$$

In the limit $T, V \ll \Gamma$ the stationary solution is still of the Gibbs form (3.102) with effective temperature

$$T_\mathrm{eff}(\gamma_\mathrm{e}) = \frac{D + 2m\gamma_\mathrm{e}T}{2A + 2m\gamma_\mathrm{e}} = \frac{T_\mathrm{eff}(0) + Tm\gamma_\mathrm{e}/A}{1 + m\gamma_\mathrm{e}/A}\,. \tag{3.107}$$

From this expression one can conclude that for $m\gamma_\mathrm{e}/A \ll 1$ and $Tm\gamma_\mathrm{e}/A \ll T_\mathrm{eff}(0)$ the effect of an additional dissipative channel can be neglected. Since $T_\mathrm{eff}(0) \geq T$ as given by Eq. (2.52), the first condition is sufficient to neglect the effect of fluctuations.

When $m\gamma_\mathrm{e}/A$ is not small there are two possibilities. If $T \gg V$, then one simply finds $T_\mathrm{eff}(\gamma_\mathrm{e}) = T_\mathrm{eff}(0) = T$, independently of γ_e. More interesting is the opposite limit, of

$T \ll V$, in this case $T_{\text{eff}}(0) = V/4$ and we find:

$$T_{\text{eff}}(\gamma_{\text{e}}) = \frac{T_{\text{eff}}(0)}{1 + m\gamma_{\text{e}}/A} \,. \tag{3.108}$$

The effect of the dissipation is then to cool down the oscillator. This is not surprising: the presence of a voltage bias induces heating and by coupling the mechanical oscillator to the cold environment one can reduce the effective temperature. Thus we find that for the observation of the transition the presence of an additional (and in general unavoidable) dissipation, is either uninfluential or an advantage (in the case $T \ll V$).

In order to see this we solve numerically the problem and show in Fig. 3.17 as a function of γ_{e} for $T = 0$ the dependence of the main peak position of $S_{xx}(\omega)$, its width, its quality factor Q, and the effective temperature of the system T_{eff}. One sees that increasing the dissipation reduces the position of the main peak and its width, but the ratio remains perfectly constant, as shown by the evolution of the quality factor. All the dependence can be explained by the renormalization of the effective temperature predicted by Eq. (3.108).

The only point that requires some additional explanation is the way the peak becomes overdamped when $\gamma_{\text{e}} \approx \omega_M$. We found that this can be understood in terms of a simple model. Let's consider the displacement spectrum for a damped harmonic oscillator of frequency ω_{t} and damping γ driven by a force noise $\xi(t)$:

$$S_{xx}(\omega) = (|\xi(\omega)|^2/m^2)[(\omega^2 - \omega_{\text{t}}^2)^2 + \omega^2\gamma^2]^{-1} \,. \tag{3.109}$$

Assuming a white noise $\xi(\omega) \approx \xi(0)$ we find that $S_{xx}(\omega)$ has two maxima at $\omega = \pm\omega_1$ with

$$\omega_1 = (\omega_{\text{t}}^2 - \gamma^2/2)^{1/2} \tag{3.110}$$

for $\gamma < \sqrt{2}\omega_{\text{t}}$ and a single maximum at $\omega = 0$ for $\gamma \geq \sqrt{2}\omega_{\text{t}}$. Assuming that ω_M plays the role of ω_{t} we plot as a dot-dashed line in the upper panel of Fig. 3.17 the expected behavior of the maximum on $S_{xx}(\omega)$ as predicted by Eq. (3.110). This agrees remarkably well with the full numerics, even if the origin of the peak is due to quartic fluctuations. We think that the reason is that the dissipation dominates, thus it is not very important the origin of the peak. Pushing even further the model in the overdamped regime we looked at the evolution of the peak by calculating the value of ω for which $S_{xx}(\omega_2) = S_{xx}(0)/2$. We find

$$\omega_2 = \left[\omega_{\text{t}}^2 - \frac{\gamma^2}{2} + \sqrt{\left(\omega_{\text{t}}^2 - \frac{\gamma^2}{2}\right)^2 + \omega_{\text{t}}^4}\,\right]^{1/2} \tag{3.111}$$

We compare then $2\omega_2$ with the full width half maximum found numerically. Note that numerically when the peak has only one side that allows to find the half-value we simply double the distance from the maximum to this frequency. Again a comparison of the linear model and the full numerics works remarkably well.

Chapter 4

Conclusions and future perspectives

4.1 Conclusions

In this thesis work, we have described the transition to a mechanical bistability induced by the strong coupling between the mechanical degree of freedom and the charge in an oscillating quantum dot in the experimentally relevant regime of $\Gamma \gg \omega_0$. We have studied the phase diagram of the problem as a function of the bias voltage (cf. Figure 3.1), the temperature (cf. Figure 3.15), and the gate voltage (cf. Figs. 3.12 and 3.14). The critical value of the coupling ε_c to observe the transition depends on the voltage quadratically (cf. Eq. (3.5)) and on the temperature linearly (cf. Eq. (3.27)).

Since reaching large coupling is a difficult experimental problem, the ideal situation for the observation of the transition is the low temperature and low bias voltage case for which $\varepsilon_c = \pi\Gamma$. In this regime the mechanical degrees of freedom have a much stronger response at the transition than the electronic ones. The perfect example is the conductance (cf. Figure 3.4): It has a singular behavior at exactly vanishing temperature and bias voltage, where the slope is discontinuous, but in practice it becomes smooth very rapidly when $V > 0$ and it has a slow power law decrease for large coupling. For sufficiently large coupling, this leads to a well defined blockade,[17] but in the range relevant for the experiments the conductance does not provide an unambiguous proof of the bistability.

The main effect at the transition is the softening of the mechanical mode as predicted by the behavior of the electronic effective potential. This reflects in the response function to an external driving force, in the ring-down time, and in particular in the displacement fluctuation spectrum $S_{xx}(\omega)$ [14]. The Q-factor of the resonator takes the minimum and universal value 1.71 at criticality. This extremely low value is due to the frequency noise caused by the interplay between fluctuations and nonlinearities; the frequency noise introduces a dephasing that can be much more important in determining the width of the resonance than the intrinsic dissipation of the system. This especially happens at the transition, where the separation of time scales is maximal.

Up to our knowledge, a direct measurement of the mechanical quantities we have studied has not yet been done. However, a similar information can be found also in the current spectral density $S_{II}(\omega)$, that has already been measured for suspended carbon nanotubes [66]. We found that measurement of $S_{II}(\omega)$ can give a direct access to $S_{xx}(\omega)$

in some situations, but the relation is not always simple. In the most interesting case of resonant tunnelling ($\Delta\varepsilon_0 = 0$) the transparency of the junction depends quadratically on the displacement, leading to Eq. (3.73) between S_{II} and S_{xx}.

Unfortunately, this relation breaks down at the transition due to the strong nonlinearity. Nevertheless, one can directly obtain the current noise and compare it to S_{xx}: They have similar remarkable features [cf. Eq. (3.78) and (3.79)]. In particular, the behavior of the peak position (ω_M) and of its width constitutes robust fingerprints of the transition.

We investigated the role of a detuning of the dot level $\Delta\varepsilon_0$ and of a finite temperature T on this critical behavior. We showed that the dependence of the mode softening with $\Delta\varepsilon_0$ is extremely sharp close to criticality, scaling with $(3|\Delta\varepsilon_0|/\Gamma)^{1/3}$. This is in striking contrast with the Lorentzian behavior expected in the weak-coupling limit and actually observed in all current experiments. We found that the main effect of the temperature is to change the value of the critical coupling needed to observe the transition and, of course, to increase the fluctuations by changing the effective temperature. Finally we showed that the effect of a dissipation not due to the electrons is actually in general useful to keep the oscillator cold in the case the voltage bias is larger than the electronic temperature.

We gave thus a global picture of the transition, investigating the main physical quantities, and showing that several features can be used to characterize without ambiguity the transition to the bistable state. These results give clear indications, opening the way to the observation of this phenomenon with state-of-the-art experiments.

4.2 Future perspectives

The experimental observation of the transition would indicate that one has entered a completely new regime, where the interaction due to a single electron has a dramatic effect on transport and mechanical behavior. In molecular devices this kind of effects might have been observed [77, 78, 79, 80], but in these systems the tuning of the electron-phonon coupling is nearly impossible. An observation of the transition in nano electromechanical systems would open the way to controlled investigations of the strong coupling regime. The increase in the coupling leads naturally to an increase in the sensitivity of the detection, with improvement in the quality of the device, for instance, for mass or force detection. From the fundamental point of view, a better understanding of the behavior of mechanical resonators in the ultra-strong coupling regime could pave the way for testing decoherence [81] as well as reaching the ultimate limits in the control of mechanical motion at the nano-scale [82].

From the theoretical point of view there are still open questions. At the moment it is difficult to perform experiments in the quantum regime ($\omega_0 \sim T$), but the observation of very high frequency mechanical resonators [65] hints at possible future developments; this should motivate further theoretical studies. An even more stringent question is opened by a recent publication [83], where by mapping the quantum problem to an effective Kondo problem it was shown that the bistability in the quantum regime may be washed out. The study was performed in equilibrium and focussed only on the probability distribution. An investigation of the response functions S_{xx} in that regime would be extremely interesting in order to clarify the expected evolution of measurable quantities at the transition for low temperatures.

Other applications can be thought of in fields that are further away from the main scope of our thesis. For example, going to the quantum regime would allow for applications in quantum information. For such a task, one needs to have a certain amount of qubits, that is, quantum systems with two separable states that can be individually addressed. On top of that, one needs also one-qubit gates, that is, a way of manipulating qubits individually, two-qubits gates, that relie on the possibility to couple a specific pair of qubits, long decoherence times to make computation and read the results, an initialization system, and a read-out system. Apart from the read-out system and the initialization system, on which one should still work, it is easy to imagine everything to be implemented with suspended carbon nanotubes in the quantum regime.

Finally, from a purely practical point of view, NEMS could maybe be used in the future to realize ultra-light and portable gas detectors to be used for the safety of many types of manual workers.

Bibliography

[1] Michael Roukes. Plenty of Room Indeed. *Scientific American*, 17:4–11, 2007.

[2] H. J. Mamin, M. Poggio, C. L. Degen, and D. Rugar. Nuclear magnetic resonance imaging with 90-nm resolution. *Nat Nano*, 2(5):301–306, May 2007.

[3] B. Lassagne, D. Garcia-Sanchez, A. Aguasca, and A. Bachtold. Ultrasensitive mass sensing with a nanotube electromechanical resonator. *Nano Letters*, 8(11):3735–3738, 2008. PMID: 18939809.

[4] P. Rabl, S. J. Kolkowitz, F. H. L. Koppens, J. G. E. Harris, P. Zoller, and M. D. Lukin. A quantum spin transducer based on nanoelectromechanical resonator arrays. *Nat Phys*, 6(8):602–608, August 2010.

[5] I. Mahboob, K. Nishiguchi, H. Okamoto, and H. Yamaguchi. Phonon-cavity electromechanics. *Nat Phys*, 8(5):387–392, May 2012.

[6] I. Mahboob, K. Nishiguchi, A. Fujiwara, and H. Yamaguchi. Phonon Lasing in an Electromechanical Resonator. *Phys. Rev. Lett.*, 110(12):127202, March 2013.

[7] J. Moser, J. Güttinger, A. Eichler, M.J. Esplandiu, D. E. Liu, M. I. Dykman, and A. Bachtold. Ultrasensitive force detection with a nanotube mechanical resonator. *Nat Nano*, 8:493–496, June 2013.

[8] S. Pecker, F. Kuemmeth, A. Secchi, M. Rontani, D. C. Ralph, P. L. McEuen, and S. Ilani. Observation and spectroscopy of a two-electron Wigner molecule in an ultraclean carbon nanotube. *Nature Physics*, 9(9):576–581, September 2013.

[9] Markus Aspelmeyer, Tobias J. Kippenberg, and Florian Marquardt. Cavity optomechanics. *Rev. Mod. Phys.*, 86(4):1391–1452, December 2014.

[10] Vera Sazonova, Yuval Yaish, Hande üstünel, David Roundy, Toms A. Arias, and Paul L. McEuen. A tunable carbon nanotube electromechanical oscillator. *Nature*, 431(7006):284–287, 2004.

[11] A. Hamo, A. Benyamini, I. Shapir, I. Khivrich, J. Waissman, K. Kaasbjerg, Y. Oreg, F. von Oppen, and S. Ilani. Electron attraction mediated by Coulomb repulsion. *Nature*, 535(7612):395–400, July 2016.

[12] Michael Galperin, Mark A. Ratner, and Abraham Nitzan. Hysteresis, switching, and negative differential resistance in molecular junctions: a polaron model. *Nano Lett.*, 5(1):125–130, January 2005.

[13] D. Mozyrsky, M. B. Hastings, and I. Martin. Intermittent polaron dynamics: Born-oppenheimer approximation out of equilibrium. *Phys. Rev. B*, 73(3):035104, January 2006.

[14] G. Micchi, R. Avriller, and F. Pistolesi. Mechanical signatures of the current blockade instability in suspended carbon nanotubes. *Physical Review Letters*, 115(20):206802, November 2015.

[15] G. Micchi, R. Avriller, and F. Pistolesi. Electromechanical transition in quantum dots. *Physical Review B*, 94(12):125417, September 2016.

[16] F. Pistolesi and S. Labarthe. Current blockade in classical single-electron nanomechanical resonator. *Phys. Rev. B*, 76:165317, Oct 2007.

[17] F. Pistolesi, Ya. M. Blanter, and Ivar Martin. Self-consistent theory of molecular switching. *Phys. Rev. B*, 78:085127, Aug 2008.

[18] Yaxing Zhang, J. Moser, J. Güttinger, A. Bachtold, and M. I. Dykman. Interplay of driving and frequency noise in the spectra of vibrational systems. *Phys. Rev. Lett.*, 113:255502, Dec 2014.

[19] Robert G. Knobel and Andrew N. Cleland. Nanometre-scale displacement sensing using a single electron transistor. *Nature*, 424(6946):291–293, July 2003.

[20] Hiroyuki Tamura, Kenji Shiraishi, and Hideaki Takayanagi. Quantum dot atoms, molecules, and superlattices. In Supriyo Bandyopadhyay and Hari Singh-Nalwa, editors, *Quantum Dots and Nanowires*, chapter 2. American Scientific Publishers, USA, 2003.

[21] A. D. Armour, M. P. Blencowe, and Y. Zhang. Classical dynamics of a nanomechanical resonator coupled to a single-electron transistor. *Physical Review B*, 69(12):125313, March 2004.

[22] D. Mozyrsky and I. Martin. Quantum-Classical Transition Induced by Electrical Measurement. *Physical Review Letters*, 89(1):018301, June 2002.

[23] Ya. M. Blanter, O. Usmani, and Yu. V. Nazarov. Single-electron tunneling with strong mechanical feedback. *Phys. Rev. Lett.*, 93:136802, Sep 2004.

[24] N. M. Chtchelkatchev, W. Belzig, and C. Bruder. Charge transport through a single-electron transistor with a mechanically oscillating island. *Physical Review B*, 70(19):193305, November 2004.

[25] Aashish A. Clerk and Steven Bennett. Quantum nanoelectromechanics with electrons, quasi-particles and Cooper pairs: effective bath descriptions and strong feedback effects. *New J. Phys.*, 7(1):238, 2005.

[26] C. B. Doiron, W. Belzig, and C. Bruder. Electrical transport through a single-electron transistor strongly coupled to an oscillator. *Phys. Rev. B*, 74:205336, 2006.

[27] O. Usmani, Ya M. Blanter, and Y. V. Nazarov. Strong feedback and current noise in nanoelectromechanical systems. *Phys. Rev. B*, 75:195312, 2007.

[28] Guillaume Weick, Fabio Pistolesi, Eros Mariani, and Felix von Oppen. Discontinuous Euler instability in nanoelectromechanical systems. *Physical Review B*, 81(12):121409, March 2010.

[29] Guillaume Weick, Felix von Oppen, and Fabio Pistolesi. Euler buckling instability and enhanced current blockade in suspended single-electron transistors. *Physical Review B*, 83(3):035420, January 2011.

[30] A. Eichler, J. Moser, J. Chaste, M. Zdrojek, I. Wilson-Rae, and A. Bachtold. Nonlinear damping in mechanical resonators made from carbon nanotubes and graphene. *Nat Nano*, 6(6):339–342, June 2011.

[31] J. Waissman, M. Honig, S. Pecker, A. Benyamini, A. Hamo, and S. Ilani. Realization of pristine and locally tunable one-dimensional electron systems in carbon nanotubes. *Nature Nanotechnology*, 8(8):569–574, August 2013.

[32] A. Benyamini, A. Hamo, S. Viola Kusminskiy, F. von Oppen, and S. Ilani. Real-space tailoring of the electronphonon coupling in ultraclean nanotube mechanical resonators. *Nature Physics*, 10(2):151–156, January 2014.

[33] S. Ilani. Private communications.

[34] Stephan Braig and Karsten Flensberg. Vibrational sidebands and dissipative tunneling in molecular transistors. *Physical Review B*, 68(20):205324, November 2003.

[35] Jens Koch and Felix von Oppen. Franck-Condon Blockade and Giant Fano Factors in Transport through Single Molecules. *Physical Review Letters*, 94(20):206804, May 2005.

[36] Jens Koch, Felix von Oppen, and A. V. Andreev. Theory of the Franck-Condon blockade regime. *Physical Review B*, 74(20):205438, November 2006.

[37] Renaud Leturcq, Christoph Stampfer, Kevin Inderbitzin, Lukas Durrer, Christofer Hierold, Eros Mariani, Maximilian G. Schultz, Felix von Oppen, and Klaus Ensslin. FranckCondon blockade in suspended carbon nanotube quantum dots. *Nature Physics*, 5(5):327–331, May 2009.

[38] J. Chaste, A. Eichler, J. Moser, G. Ceballos, R. Rurali, and A. Bachtold. A nanomechanical mass sensor with yoctogram resolution. *Nat Nano*, 7(5):301–304, April 2012.

[39] Marc Ganzhorn, Svetlana Klyatskaya, Mario Ruben, and Wolfgang Wernsdorfer. Carbon Nanotube Nanoelectromechanical Systems as Magnetometers for Single-Molecule Magnets. *ACS Nano*, 7(7):6225–6236, July 2013.

[40] P. M. Kosaka, V. Pini, J. J. Ruz, R. A. da Silva, M. U. Gonzlez, D. Ramos, M. Calleja, and J. Tamayo. Detection of cancer biomarkers in serum using a hybrid mechanical and optoplasmonic nanosensor. *Nat Nano*, 9(12):1047–1053, December 2014.

[41] Sumio Iijima. Helical microtubules of graphitic carbon. *Nature*, 354(6348):56–58, November 1991.

[42] J. W. Mintmire, B. I. Dunlap, and C. T. White. Are fullerene tubules metallic? *Physical Review Letters*, 68(5):631–634, February 1992.

[43] Noriaki Hamada, Shin-ichi Sawada, and Atsushi Oshiyama. New one-dimensional conductors: Graphitic microtubules. *Physical Review Letters*, 68(10):1579–1581, March 1992.

[44] Riichiro Saito, Mitsutaka Fujita, G. Dresselhaus, and M. S. Dresselhaus. Electronic structure of graphene tubules based on c_{60}. *Physical Review B*, 46(3):1804–1811, July 1992.

[45] D. S. Bethune, C. H. Klang, M. S. de Vries, G. Gorman, R. Savoy, J. Vazquez, and R. Beyers. Cobalt-catalysed growth of carbon nanotubes with single-atomic-layer walls. *Nature*, 363(6430):605–607, June 1993.

[46] Sumio Iijima and Toshinari Ichihashi. Single-shell carbon nanotubes of 1-nm diameter. *Nature*, 363(6430):603–605, June 1993.

[47] Andreas Thess, Roland Lee, Pavel Nikolaev, Hongjie Dai, Pierre Petit, Jerome Robert, Chunhui Xu, Young Hee Lee, Seong Gon Kim, Andrew G. Rinzler, Daniel T. Colbert, Gustavo E. Scuseria, David Tomnek, John E. Fischer, and Richard E. Smalley. Crystalline ropes of metallic carbon nanotubes. *Science*, 273(5274):483–487, July 1996.

[48] Alan M. Cassell, Jeffrey A. Raymakers, Jing Kong, and Hongjie Dai. Large scale cvd synthesis of single-walled carbon nanotubes. *The Journal of Physical Chemistry B*, 103(31):6484–6492, August 1999.

[49] Edward A. Laird, Ferdinand Kuemmeth, Gary A. Steele, Kasper Grove-Rasmussen, Jesper Nygrd, Karsten Flensberg, and Leo P. Kouwenhoven. Quantum transport in carbon nanotubes. *Reviews of Modern Physics*, 87(3):703–764, July 2015.

[50] Rodney S. Ruoff, Dong Qian, and Wing Kam Liu. Mechanical properties of carbon nanotubes: theoretical predictions and experimental measurements. *Comptes Rendus Physique*, 4(9):993 – 1008, 2003.

[51] R. Saito, M. Fujita, G. Dresselhaus, and M. S Dresselhaus. Electronic structure of chiral graphene tubules. *Applied Physics Letters*, 60(18):2204–2206, 1992.

[52] Rufan Zhang, Yingying Zhang, Qiang Zhang, Huanhuan Xie, Weizhong Qian, and Fei Wei. Growth of half-meter long carbon nanotubes based on schulzflory distribution. *ACS Nano*, 7(7):6156–6161, 2013. PMID: 23806050.

[53] A. K. Httel, M. Poot, B. Witkamp, and H. S. J. van der Zant. Nanoelectromechanics of suspended carbon nanotubes. *New Journal of Physics*, 10(9):095003, 2008.

[54] B. Reulet, A. Yu. Kasumov, M. Kociak, R. Deblock, I. I. Khodos, Yu. B. Gorbatov, V. T. Volkov, C. Journet, and H. Bouchiat. Acoustoelectric Effects in Carbon Nanotubes. *Physical Review Letters*, 85(13):2829–2832, September 2000.

[55] Vincent Gouttenoire, Thomas Barois, Sorin Perisanu, Jean-Louis Leclercq, Stephen T. Purcell, Pascal Vincent, and Anthony Ayari. Digital and FM Demodulation of a Doubly Clamped Single-Walled Carbon-Nanotube Oscillator: Towards a Nanotube Cell Phone. *Small*, 6(9):1060–1065, May 2010.

[56] B. Gao, A. Komnik, R. Egger, D. C. Glattli, and A. Bachtold. Evidence for luttinger-liquid behavior in crossed metallic single-wall nanotubes. *Physical Review Letters*, 92(21):216804, May 2004.

[57] B. Gao, Y. F. Chen, M. S. Fuhrer, D. C. Glattli, and A. Bachtold. Four-Point Resistance of Individual Single-Wall Carbon Nanotubes. *Physical Review Letters*, 95(19):196802, October 2005.

[58] B. Gao, D. C. Glattli, B. Plaais, and A. Bachtold. Cotunneling and one-dimensional localization in individual disordered single-wall carbon nanotubes: Temperature dependence of the intrinsic resistance. *Physical Review B*, 74(8):085410, August 2006.

[59] B. J. LeRoy, S. G. Lemay, J. Kong, and C. Dekker. Electrical generation and absorption of phonons in carbon nanotubes. *Nature*, 432(7015):371–374, November 2004.

[60] S. Sapmaz, P. Jarillo-Herrero, Ya. M. Blanter, C. Dekker, and H. S. J. van der Zant. Tunneling in Suspended Carbon Nanotubes Assisted by Longitudinal Phonons. *Physical Review Letters*, 96(2):026801, January 2006.

[61] Benoit Witkamp, Menno Poot, and Herre S. J. van der Zant. Bending-Mode Vibration of a Suspended Nanotube Resonator. *Nano Letters*, 6(12):2904–2908, December 2006.

[62] D. Garcia-Sanchez, A. San Paulo, M. J. Esplandiu, F. Perez-Murano, L. Forr, A. Aguasca, and A. Bachtold. Mechanical Detection of Carbon Nanotube Resonator Vibrations. *Physical Review Letters*, 99(8):085501, August 2007.

[63] B. Lassagne, Y. Tarakanov, J. Kinaret, D. Garcia-Sanchez, and A. Bachtold. Coupling mechanics to charge transport in carbon nanotube mechanical resonators. *Science*, 325(5944):1107–1110, August 2009.

[64] G. A. Steele, A. K. Hüttel, B. Witkamp, M. Poot, H. B. Meerwaldt, L. P. Kouwenhoven, and H. S. J. van der Zant. Strong coupling between single-electron tunneling and nanomechanical motion. *Science*, 325(5944):1103–1107, 2009.

[65] Edward A. Laird, Fei Pei, Wei Tang, Gary A. Steele, and Leo P. Kouwenhoven. A High Quality Factor Carbon Nanotube Mechanical Resonator at 39 GHz. *Nano Letters*, 12(1):193–197, January 2012.

[66] J. Moser, A. Eichler, J. Güttinger, M. I. Dykman, and A. Bachtold. Nanotube mechanical resonators with quality factors of up to 5 million. *Nat Nano*, 9(12):1007–1011, December 2014.

[67] G. A. Steele, G. Gotz, and L. P. Kouwenhoven. Tunable few-electron double quantum dots and Klein tunnelling in ultraclean carbon nanotubes. *Nature Nanotechnology*, 4(6):363–367, June 2009.

[68] Andreas K. Hüttel, Gary A. Steele, Benoit Witkamp, Menno Poot, Leo P. Kouwenhoven, and Herre S. J. van der Zant. Carbon nanotubes as ultrahigh quality factor mechanical resonators. *Nano Letters*, 9(7):2547–2552, July 2009.

[69] Ben H. Schneider, Vibhor Singh, Warner J. Venstra, Harold B. Meerwaldt, and Gary A. Steele. Observation of decoherence in a carbon nanotube mechanical resonator. *Nat Comms*, 5:5819, dec 2014.

[70] Daniel F. Walls, Gerard J. Milburn, and Walls-Milburn. *Quantum optics.* Springer, Berlin, 2. ed edition, 2008.

[71] A. A. Clerk, M. H. Devoret, S. M. Girvin, Florian Marquardt, and R. J. Schoelkopf. Introduction to quantum noise, measurement, and amplification. *Reviews of Modern Physics*, 82(2):1155–1208, April 2010.

[72] Milton Abramowitz and Irene A. Stegun, editors. *Handbook of mathematical functions: with formulas, graphs, and mathematical tables.* Dover books on mathematics. Dover Publ, New York, NY, 9. dover print edition, 2013.

[73] Milton Abramowitz and Irene A Stegun. *Handbook of mathematical functions: with formulas, graphs, and mathematical tables.* Number 55 in Applied Mathematics. Courier Corporation, 1964.

[74] Ya. M. Blanter and M. Bttiker. Shot noise in mesoscopic conductors. *Physics Reports*, 336(12):1–166, September 2000.

[75] M. I. Dykman, S. M. Soskin, and M. A. Krivoglaz. Spectral distribution of a nonlinear oscillator performing Brownian motion in a double-well potential. *Physica A: Statistical Mechanics and its Applications*, 133(12):53–73, October 1985.

[76] M.I. Dykman and M.A. Krivoglaz. Time correlation functions and spectral distributions of the duffing oscillator in a random force field. *Physica A: Statistical Mechanics and its Applications*, 104(3):495–508, December 1980.

[77] N. J. Tao. Electron transport in molecular junctions. *Nature Nanotechnology*, 1(3):173–181, December 2006.

[78] Emanuel Lrtscher, JacobW. Ciszek, James Tour, and Heike Riel. Reversible and Controllable Switching of a Single-Molecule Junction. *Small*, 2(8-9):973–977, August 2006.

[79] Byoung-Young Choi, Se-Jong Kahng, Seungchul Kim, Hajin Kim, Hyo Won Kim, Young Jae Song, Jisoon Ihm, and Young Kuk. Conformational Molecular Switch of the Azobenzene Molecule: A Scanning Tunneling Microscopy Study. *Physical Review Letters*, 96(15):156106, April 2006.

[80] J. Gaudioso, L. J. Lauhon, and W. Ho. Vibrationally Mediated Negative Differential Resistance in a Single Molecule. *Physical Review Letters*, 85(9):1918–1921, August 2000.

[81] A. J. Leggett. Testing the limits of quantum mechanics: motivation, state of play, prospects. *Journal of Physics: Condensed Matter*, 14(15):R415, 2002.

[82] Menno Poot and Herre S. J. van der Zant. Mechanical systems in the quantum regime. *Physics Reports*, 511(5):273–335, February 2012.

[83] Juliane Klatt, Lothar Mhlbacher, and Andreas Komnik. Kondo effect and the fate of bistability in molecular quantum dots with strong electron-phonon coupling. *Physical Review B*, 91(15):155306, April 2015.